Fall 2019

On developing a graphitic white iron for metal-to-metal wear systems

Jie Wan

Department: Materials Science and Engineering

ON DEVELOPING A GRAPHITIC WHITE IRON FOR METAL-TO-METAL WEAR SYSTEMS

by

JIE WAN

A DISSERTATION

Presented to the Faculty of the Graduate School of the

MISSOURI UNIVERSITY OF SCIENCE AND TECHNOLOGY

In Partial Fulfillment of the Requirements for the Degree

DOCTOR OF PHILOSOPHY

in

MATERIALS SCIENCE & ENGINEERING

2019

Approved by:

Mingzhi Xu, Advisor
David C. Van Aken
Haiming Wen
Jingjing Qing
Julia E. Medvedeva

PUBLICATION DISSERTATION OPTION

This dissertation consists of the following four articles, formatted in the style used by the Missouri University of Science and Technology:

Paper I: Pages 18-48 are intended to be submitted to Wear.

Paper II: Pages 49-78 have been published on Metallurgical and Materials Transactions A.

Paper III: Pages 79-110 have been published on Wear.

Paper IV: Pages 111-132 are intended to be submitted to Wear.

ABSTRACT

This research addressed heat dissipation issues related to the adhesive wear observed in metal-to-metal wear systems, by developing a graphitic white iron to increase thermal diffusivity of the wear components. One of the premium materials commonly used in current metal-to-metal wear systems is Fe15Mo18Cr and field returned parts were characterized as part of this study. Failure analysis showed that white layers were formed on the wearing surface due to frictional heating and surface deformation. These white layers were extremely brittle and could be fractured easily during use, which in turn led to micro-galling defects that caused parts leakage. Increasing thermal diffusivity of the material was recommended to improve the performance of wear components.

A new alloy, graphitic white iron, was developed for metal-to-metal wear systems by introducing 3.2-9.6 vol.% graphite flakes into white irons, to increase thermal diffusivity and reduce friction and frictional heating. Graphite volume percent was quantitatively investigated. It turned out that, at 200 °C, thermal diffusivity increased by ~114% with increasing graphite to 7.6 vol.%. Abrasive and adhesive wear resistance was measured by dry sand/rubber wheel test and block on ring test, respectively. Empirical models were established to predict graphite volume percent for any given composition, and a Hashin-Shtrikman model was used to predict the thermal diffusivity of the multiphase alloy. Abrasive and adhesive wear resistance was found to depend upon composite hardness and graphite volume percent. It was found that 1 vol.% graphite was equivalent to an increase of 2.33 HRC and 2.66 HRC in composite hardness with respect to abrasive wear resistance and adhesive wear resistance, respectively.

ACKNOWLEDGMENTS

First and foremost, I would like to thank my wife Yanru Lu for being supportive and understanding throughout my four years' journey. I really appreciate all her sacrifices to make it possible for me to finish my degree. I would like to express my special appreciation to my advisor, Dr. Mingzhi Xu. He led me here as a PhD student and helped me so much not only on my research, but also in my daily life. I would like to thank Dr. David C. Van Aken, Dr. Jingjing Qing, Dr. Haiming Wen, and Dr. Julia E. Medvedeva for their technical discussion and guidance throughout my research.

This work has been financially supported by Caterpillar Inc. through the APEC-Caterpillar Fellowship. I am enormously grateful to my friend, Yuan Gao, lecturer at Xi'an Jiaotong University, who recognized and recommended me to this fellowship. Further gratitude is extended to friends and colleagues at Caterpillar in Mossville, IL Tech Center including: Linda R. Harrell, Thomas E. Clements, James O. Barlow, Thomas J. Yaniak, Rob Pickerill, Christopher A. Barnes, George B. Kokos, Tianju Liu, Zack Birky, Olga Rowan, Connor J. Hass, Hyung K. Yoon, Brandon L. Reneau, Isaiah Strong.

I would like to extend my appreciation to the staff of the Materials Research Center including Dr. Clarissa Wisner for her guidance in electron microscopy and Dr. Eric Bohannon for his support on X-ray diffraction and DSC analyses. I'm grateful to Dr. Jeremy Watts, and Austin Stanfield for their help on Laser Flash operation, and Dr. Andrew Hoffman for his help with indexing TEM images. I would also like to thank Dr. Daniel Field, Dr. Mario Buchely, Viraj Athavale, Breton Hrebec, and Yizhou Du for their assistance with foundry experiment. Perrin Habecker, Logan Bader, Wayne Pugh are acknowledged for their help with regard to sample preparation.

TABLE OF CONTENTS

Page

PUBLICATION DISSERTATION OPTION iii

ABSTRACT iv

ACKNOWLEDGMENTS v

LIST OF ILLUSTRATIONS xii

LIST OF TABLES xvii

SECTION

1. INTRODUCTION 1

2. LITERATURE REVIEW 4

2.1. WEAR RESISTANT MATERIALS 4

2.1.1. Alloyed White Iron. 4

2.1.2. Cobalt-Based Stellite. 6

2.1.3. Nickel-Based/Boride Alloy. 8

2.2. WEAR MECHANISMS 10

2.2.1. Adhesive Wear. 11

2.2.2. Abrasive Wear. 11

2.2.3. Fatigue Wear. 13

2.2.4. Corrosive Wear. 14

2.3. FRICTIONAL HEATING AND CONTACT TEMPERATURE 14

2.3.1. Frictional Heating. 14

2.3.2. Contact Temperature. 16

2.4. EMPHASIS FOR THIS WORK 17

PAPER

I. MICROSTRUCTURAL CHARACTERIZATION AND FAILURE ANALYSIS OF A WEAR RESISTANT, HIGH MOLYBDENUM AND CHROMIUM WHITE IRON 18

ABSTRACT 18

1. INTRODUCTION 19

2. MATERIAL AND METHOD 21

2.1. MATERIAL 21

2.2. SAMPLE PREPARATION AND CHARACTERIZATION 21

2.2.1. As-Cast Samples 21

2.2.2. Field Returned Wear Component. 22

3. RESULTS 24

3.1. METALLOGRAPHIC RESULTS 24

3.1.1. Optical Microstructure. 24

3.1.2. Electrolytic Deep Etching Microstructure. 25

3.1.3. TKD Phase Mapping. 26

3.2. FAILURE ANALYSIS 28

3.2.1. Cross Section. 28

3.2.2. White Layer. 30

3.2.3. Worn Surface. 33

4. DISCUSSION 34

4.1. SOLIDIFICATION SEQUENCE AND MICROSTRUCTURAL CORRELATION 34

4.2. WHITE LAYER 38

4.3. FAILURE MECHANISM 40

5. CONCLUSION 41

ACKNOWLEDGEMENTS 42

REFERENCES 42

II. DESIGNING A NOVEL GRAPHITIC WHITE IRON FOR METAL-TO-METAL WEAR SYSTEMS 49

ABSTRACT 49

1. INTRODUCTION 50

2. MATERIAL AND METHODS 52

2.1. RATIONAL FOR CHEMISTRY 52

2.2. SAMPLE PREPARATION AND CHARACTERIZATION 54

3. METALLOGRAPHY RESULTS 55

4. DISCUSSION 57

4.1. GRAPHITE PHASE FRACTION VS CARBON EQUIVALENT 57

4.2. CHARACTERIZATION OF CARBIDES 63

4.3. SOLIDIFICATION SEQUENCE 66

4.3.1. Alloy 3Cr. 66

4.3.2. Alloy 5Cr. 66

4.3.3. Alloy 7Cr. 66

4.3.4. Alloy 9Cr. 67

4.3.5. Alloy 11Cr. 67

4.4. M_7C_3 TO FE_3C TRANSFORMATION IN LEDEBURITE-SHAPED STRUCTURE IN ALLOY 11CR 71

4.5. VICKERS INDENTATION HARDNESS ANALYSIS 74

5. CONCLUSION 75

ACKNOWLEDGEMENTS 76

REFERENCES 76

III. DEVELOPING A GRAPHITIC WHITE IRON FOR ABRASIVE WEAR APPLICATION: THERMAL AND WEAR PROPERTIES 79

ABSTRACT 79

1. INTRODUCTION 80

2. MATERIALS AND METHODS 82

2.1. MATERIAL DEVELOPMENT 82

2.2. SAMPLE PREPARATION AND CHARACTERIZATION 85

2.2.1. Metallographic Sample Preparation and Characterization. 85

2.2.2. Thermal Diffusivity Sample Preparation and Characterization. 85

2.2.3. Wear Test Sample Preparation and Characterization. 86

3. RESULTS 87

3.1. METALLOGRAPHIC MICROSTRUCTURE 87

3.2. THERMAL DIFFUSIVITY ANALYSIS 91

3.3. WEAR PROPERTY ANALYSIS 92

3.4. WEAR SCARS EVALUATION 93

4. DISCUSSION 95

4.1. THERMAL DIFFUSIVITY INVESTIGATION 95

4.2. WEAR RESISTANCE INVESTIGATION 99

4.3. WEAR PROPERTY MODEL 102

4.4. RATIONAL FOR GRAPHITE CONTRIBUTION 104

4.5. ALLOY COST 104

5. CONCLUSION 105

ACKNOWLEDGEMENTS 106

REFERENCES 106

IV. ADHESIVE WEAR PROPERTY OF A GRAPHITIC WHITE IRON DESIGNED FOR METAL-TO-METAL WEAR SYSTEMS 111

ABSTRACT 111

1. INTRODUCTION 112

1.1. THERMAL DIFFUSIVITY 113

1.2. ABRASIVE WEAR 113

2. MATERIALS AND METHODS 115

2.1. MATERIALS 115

2.2. SAMPLE PREPARATION AND CHARACTERIZATION 116

2.2.1. Metallographic Samples. 116

2.2.2. Block On Ring Samples. 116

3. RESULTS 117

3.1. MICROSTRUCTURE 117

3.2. ADHESIVE WEAR PERFORMANCE 117

3.3. ADHESIVE WEAR SCAR EVALUATION 119

4. DISCUSSION 122

4.1. ADHESIVE WEAR RESISTANCE 122

4.2. ADHESIVE WEAR MODEL 124

4.3. ADHESIVE WEAR VS. ABRASIVE WEAR 126

4.4. RATIONAL FOR GRAPHITE CONTRIBUTION 127

5. CONCLUSION 127

ACKNOWLEDGEMENTS 128

REFERENCES 128

SECTION

3. CONCLUSIONS AND RECOMMENDATIONS 133

3.1. CONCLUSIONS 133

3.1.1. Alloy Fe15Mo18Cr. 133

3.1.2. Graphitic White Iron. 134

3.1.2.1. Metallographic analyses of microstructures. 134

3.1.2.2. Thermal diffusivity. 135

3.1.2.3. Wear performance 136

3.2. RECOMMENDATIONS 137

BIBLIOGRAPHY 140

VITA 151

LIST OF ILLUSTRATIONS

SECTION Page

Figure 2.1. Plot showing typical alloying elements effect on the carbide formation in alloyed white iron 4

Figure 2.2. Schematic images of four representative wear modes 10

Figure 2.3. Three different modes of abrasive wear observed by SEM: cutting mode (a), steel pin on brass plate; wedge-forming mode (b), steel pin on stainless steel plate; ploughing mode (c), steel pin on brass plate 12

Figure 2.4. Magnitude of shear stress at various depths directly below the point of contact of two hard surfaces in rolling, sliding and combined contact 13

Figure 2.5. Temperature effect on the wear rate of an Al0.25CoCrFeNi high-entropy alloy from a dry sliding wear test 15

Figure 2.6. Contact temperature profile in a flash temperature study during dry friction process at high sliding speed 16

PAPER I

Figure 1. FIB-SEM sample preparation: (a) SEM image before FIB; (b) Pt deposition on the selected area for site-specific sample preparation; (c) Removal of material adjacent; (d) Lift-out of the TEM sample using a micro-manipulator 23

Figure 2. Marble's reagent etched microstructure from: (a) Casting center; (b) Casting surface 24

Figure 3. SEM images showing the electrolytic deep etched microstructure taken from the subsurface of the casting. 25

Figure 4. TKD images from the casting subsurface showing: (a) TEM image; (b) Phase mapping on the white box in (a); and (c)-(h) EDS mappings for Fe, Cr, V, Mo, C, and Mn, respectively. 27

Figure 5. Optical micrographs on the cross section of the field returned component showing: (a) final wear point on the wearing surface; (b) affected depth next to the final wear point. 29

Figure 6. Optical micrograph on the cross section of the field return component showing white layer on the worn surface 30

Figure 7. BF TEM images of the white layer 31

Figure 8. TEM images showing (a) SAD pattern for the white layer; (b) Indexing of the SAD pattern..... 31

Figure 9. Pictures of (a) TEM DF image with the dashed line showing the line scan position, and arrows indicating the persistent carbides; (b) Line scan spectrum profile. 32

Figure 10. SEM images showing the worn surface of a field returned component..... 34

Figure 11. Diagrams showing phase evolution calculated using JMatPro during solidification from 1300 °C to 700 °C (a), and from1270 °C to 1150 °C (b). 35

Figure 12. Schematic showing the correlation between the microstructure and the solidification sequence 37

PAPER II

Figure 1. The primary phase formed during solidification at different contents of C and Cr; Colored dots represent the alloys studied in this research; numbers in each callout represent the chemistry of C and Cr individually. 53

Figure 2. Graphite morphology in as-polished microstructure: (a) 3Cr; (b) 5Cr; (c) 7Cr; (d) 9Cr; (e) 11Cr. 55

Figure 3. Carbide morphology in 2% nital etched microstructure at a lower magnification: (a) 3Cr; (b) 5Cr; (c) 7Cr; (d) 9Cr; (e) 11Cr..... 56

Figure 4. Pearlite structure revealed by 2% nital etched microstructure at a higher magnification: (a) 3Cr; (b) 5Cr; (c) 7Cr; (d) 9Cr; (e) 11Cr..... 57

Figure 5. Contrast threshold was adjusted in ImageJ to include (a) graphite and (b) primary and eutectic carbides; scale bars were removed to avoid interference with the threshold. 58

Figure 6. Phase percent comparison among five alloys for: (a) Graphite; (b) Carbide. ... 59

Figure 7. Relation between carbon equivalent and graphite percent. 61

Figure 8. Cooling rate study for: (a) Cooling curves obtained from ATAS quick cups; (b) Relation between graphite volume percent and cooling rate measured from temperature curves at 900°C. 62

Figure 9. Fe/Cr(wt.%) ratio of : (a) Plate carbide in 7Cr; (b) Plate carbide in 9Cr; (c) Cluster carbide in 7Cr; (d) Hexagonal shaped carbide in 9Cr; (e) Hexagonal shaped carbide in 11Cr. 64

Figure 10. Pearlite in the center of M_7C_3: (a) 7Cr; (b) 9Cr; (c) 11Cr. 65

Figure 11. Schematics of equilibrium step diagram calculated using Factsage for: (a) 3Cr; (b) 5Cr; (c) 7Cr; (d) 9Cr; (e) 11Cr 68

Figure 12. Fe/Cr(wt.%) ratio for carbide in ledeburite-shaped structure for alloy 11Cr. 69

Figure 13. Schematics of: (a) SEM image of alloy 11Cr taken by an EBSD forescatter detector; (b) EBSD phase mapping including spots where Kikuchi pattern was taken for each phases; (c) Indexed Kikuchi pattern for ferrite obtained at spot 1; (d) Indexed Kikuchi pattern for Fe_3C obtained at spot 2; (e) Indexed Kikuchi pattern for M_7C_3 at spot 3. 70

Figure 14. Schematics of solidification sequence: (a) 3Cr; (b) 5Cr; (c) 7Cr; (d) 9Cr; (e) 11Cr..... 70

Figure 15. Schematics of heat treated alloy 11Cr: (a) SEM image taken by an EBSD forescatter detector; (b) EBSD phase mapping on ledeburite-shaped structure; (c) Cr EDS mapping. 73

Figure 16. Change of Cr content in wt.% versus temperature in different phases calculated using FactSage equilibrium module..... 73

Figure 17. Schematics of Vickers indentation hardness with a parameter of 490.6mN press load, 10s press time and 40x objective magnification. 74

PAPER III

Figure 1. Primary phase formed during solidification for ferrous alloy containing 2wt.%Si-0.5wt.%Mn, and different levels of C and Cr. 83

Figure 2. An example of a keel block casting produced..... 84

Figure 3. As polished microstructures for alloys studied 87

Figure 4. As polished microstructures for alloys studied at a higher magnification 88

Figure 5. Carbides of different shapes observed on the etched micrographs of alloys studied 89

Figure 6. Pearlite in the matrix revealed using 2% nital etching in alloys studied..... 89

Figure 7. Measured graphite volume percent for the five alloys studied..... 90

Figure 8. Thermal diffusivity results for five graphitic white irons 91

Figure 9. Measurements showing that a higher graphite volume percent improves the thermal diffusivity of the alloy at every testing temperature. 92

Figure 10. Volume loss of the five graphitic white irons studied compared to Hardox 400 and alloy Fe15Mo19Cr..... 93

Figure 11. SEM back scattered electron images showing the topography information of wear scars for alloys (a) 3Cr; (b) 5Cr; (c) 7Cr; (d) 9Cr; (e) 11Cr; (f) Fe15Mo19Cr. 94

Figure 12. Thermal diffusivity of the alloy excluding graphite calculated using the lower bound of the Hashin-Shtrikman model 96

Figure 13. Plots of thermal diffusivity of the alloy excluding graphite against carbon equivalent of the alloy excluding graphite at temperatures of: (a) 200 °C; (b) 300 °C; (c) 400 °C; (d) 500 °C; (e) 600 °C; (f) 800 °C. 98

Figure 14. Plots showing the relationship between temperature and (a) slope of linear equations; (b) constant of linear equations shown in Figure 12..... 99

Figure 15. Vickers indentation hardness for M_7C_3 carbide in alloys 7Cr, 9Cr and 11Cr 100

Figure 16. EBSD phase mapping for alloys (a) Fe15Mo9Cr; (b) 9Cr. 101

Figure 17. Cr EDS mapping for alloys 7Cr (a), 9Cr (b) and 11Cr (c); Contrast threshold adjusted to include carbidic phases in alloys 7Cr (d), 9Cr (e) and 11Cr (f). 102

Figure 18. Plots showing: (a) volume loss versus hardness of alloys studied; (b) volume loss as a function of alloy hardness and graphite volume percent. 103

Figure 19. Plots showing: (a) alloy cost comparison in dollar per pound for alloys studied; (b) alloy cost versus volume loss. 105

PAPER IV

Figure 1. Measurements showing that a higher graphite volume percent improves the thermal diffusivity of the alloy at every testing temperature. 113

Figure 2. Plots showing: (a) volume loss versus hardness of alloys studied; (b) volume loss as a function of alloy hardness and graphite volume percent 114

Figure 3. As-polished microstructures for five alloys studied..... 118

Figure 4. Nital etched microstructures for five alloys studied..... 118

Figure 5. BOR volume loss of the graphitic white irons studied compared to alloy Fe15Mo19Cr 119

Figure 6. SEM secondary electron images showing the BOR wear scars for all five graphitic white irons studied as well as alloy Fe15Mo19Cr 120

Figure 7. SEM secondary electron image showing the BOR wear scar for: (a) alloy 9Cr; (b) alloy Fe15Mo19Cr 121

Figure 8. Pictures for alloy Fe15Mo19Cr showing: (a) SEM image taken from BOR wear scar; (b) DIC image of the as-polished microstructure 122

Figure 9. Plots showing: (a) volume loss versus hardness of alloys studied; (b) volume loss as a function of alloy hardness and graphite volume percent 125

Figure 10. Wear resistance comparison between abrasive wear test (DSRW) and adhesive wear test (BOR) for five graphitic white irons developed. 126

SECTION

Figure 3.1. Schematics of equilibrium step diagram calculated using JMatPro for future graphitic white iron alloy design. 139

LIST OF TABLES

SECTION Page

Table 2.1. Chemical compositions of alloyed white irons for abrasion-resistant application. 6

Table 2.2. Chemical compositions for selected Stellite alloys. 7

Table 2.3. Chemical compositions for common nickel-based/boride alloys. 9

PAPER I

Table 1. Composition (wt.%) analyzed using an optical emission spectrometer and a Leco C/S analyzer. 21

Table 2. Operation parameters for electrolytic deep etching and polishing. 22

PAPER II

Table 1. Composition analyzed using spark emission spectrometer and Leco C/S analyzer. 54

Table 2. Pertinent temperature information for all studied alloys. 54

Table 3. Comparison of Fe/Cr(wt.%) ratio between FactSage calculation and ASPEX-EDS measurement for Fe3C and M7C3. 65

PAPER III

Table 1. Composition of the five alloys analyzed using an optical emission spectrometer and Leco combustion C/S analyzers. 84

Table 2. Pertinent temperature information for the five alloys studied. 84

Table 3. Composition of the alloy excluding graphite for the five graphitic white irons. 97

Table 4. Exposed volume percent for carbides measured on the Cr EDS mapping acquired from the wear scars. 102

PAPER IV

Table 1. Chemical compositions of the five alloys analyzed using an optical emission spectrometer and a Leco combustion C/S analyzer. 115

SECTION

Table 3.1. Chemical compositions proposed for future graphitic white iron alloy design 138

1. INTRODUCTION

Lubrication of rotating machinery requires seals that can inhibit the ingress of abrasive particles. Metal-to-metal wear systems are extensively used in modern machinery parts [1], [2], [3], [4], [5], [6], [7], [8]. Wear of metal-to-metal wear systems, repair and replacing costs of these parts, and the associated downtime related to these activities result in significant costs [9]. It has been estimated that the cost of wear ranges from 1% to 4% of the gross national product for an industrialized nation [10]. In order to decrease the wear rate and extend the lifetime of these wear components, various hard facing materials have been invented for these applications, such as silicon carbide, tungsten carbide, Ni-Resist cast iron, Stellite, and aluminum oxide [3], [11], [12], [13]. However, these hardfacing materials are either too expensive or too brittle to be widely used [14]. For example, cobalt-based Stellite is used primarily in military applications where material cost can be justified on non-economic factors [15].

Most of the metal-to-metal wear systems are used in full or partial lubrication environments, because lubrication significantly reduces frictional forces and carries away heat and debris generated during service [16]. Addition of corrosion inhibitors to the lubricant has been proven to significantly improve corrosive wear resistance and this mechanism of failure is no longer performance limiting in metal-to-metal wear systems [17], [18]. Therefore, among the four basic wear types categorized by Kato (abrasive wear, adhesive wear, fatigue wear, and corrosive wear) [19], the most prevalent wear type associated with metal-to-metal wear system is adhesive wear [20], [21], [22], [23], [24]. Nevertheless, failure of the metal-to-metal wear systems can lead to abrasive wear

as a result of ingress of external particles or metallic debrises generated by adhesive wear. [25]. Both adhesive and abrasive wear can cause frictional heating on the contact surfaces of the wear components [26], [27], [28], [29], [30]. High surface temperatures can negatively impact tribological behavior and even cause failure by (1) changes in the structure and properties of the materials; (2) oxidation of the surface; (3) melting of the contacting parts; (4) softening of the materials; (5) changes in stability and viscosity of the lubricant [30], [31].

One of the major problems caused by excessive frictional heat is the formation of white layers on the contact surface [32], [33], [34]. A white layer is characterized as a non-etching layer formed on contact surfaces, which appears featureless when viewed using an optical microscope [35]. The white layer is an extremely hard and brittle structure, and can cause crack formation and product failure [36], [37], [38], [39]. Failure analyses on the field returned components showed that the white layer is a super-refined microstructure with a grain size in the order of approximately 15 nm produced by thermomechanical deformation of the surface [23]. Micro-galling and fracture of the white layer is often the root cause of part failure in a metal-to-metal wear system.

Increasing thermal diffusivity of metal-to-metal materials can potentially increase heat dissipation and mitigate the frictional heating, which could potentially increase the performance of these wear components. In this regard, a composite approach by incorporating graphite to improve thermal diffusivity was investigated in this research. Addition of graphite to plasma sprayed NiCrBSi coating has demonstrated improved abrasive wear resistance [40] and addition of graphite was also found to improve the wear resistance of white iron mill rolls [41], [42], [43]. However, in the latter studies the

graphite addition observed in the white iron mill rolls was a spheroidal morphology, which may not be the optimum with respect to improving thermal diffusion [44], [45], [46]. Matsushita et al. reported that the thermal diffusivity of a cast iron increases with decreasing the nodularity of its graphite [47]. Therefore, flake graphite as observed in gray iron has the best thermal diffusivity when compared with vermicular graphite (compacted iron) and spheroidal graphite (ductile iron).

The purpose of this research was to develop a new alloy system for metal-to-metal wear systems by introducing graphite flakes into white iron. This new alloy should have adequate abrasive wear resistance, and be cost friendly. The author named this alloy as graphitic white iron.

2. LITERATURE REVIEW

2.1. WEAR RESISTANT MATERIALS

2.1.1. Alloyed White Iron. White cast iron is one of the oldest wear resistant materials known and is named so because of its characteristically white fracture surface relative to the fracture of gray iron. White iron can be formed from the same composition as gray iron by increasing the cooling rate during solidification [48]. Instead of forming graphite (pure carbon), the carbon is present in the form of cementite or Fe3C carbide. An 1148°C cementite will form as part of a metastable eutectic solidification with austenite. Fe3C carbide is a relatively hard phase (800-1100 HV) and is good for wear resistance, which makes white cast iron extensively used in grinding media for mineral processing [49]. In heavy sections or relatively large castings it is difficult to obtain sufficiently high cooling rates to promote white cast iron; and thus, high alloy additions are added to promote carbide formation at these slower cooling rates [20].

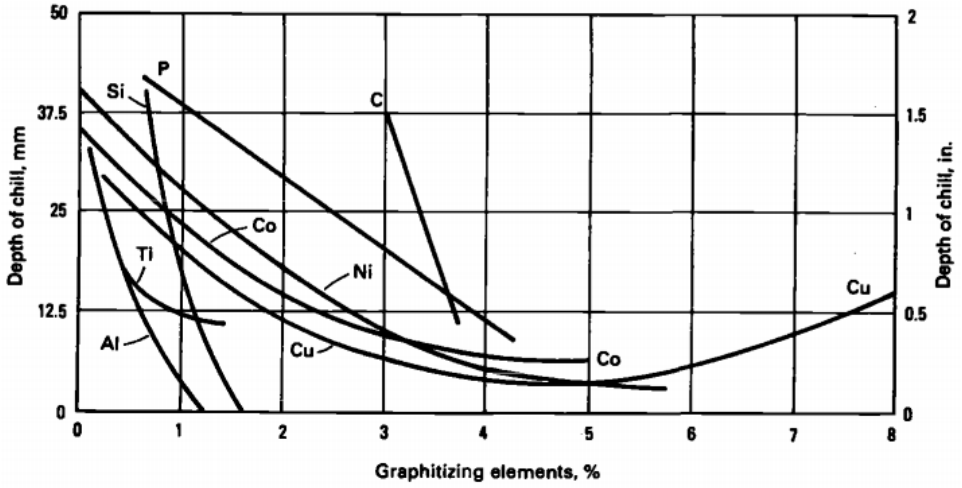

(a)

Figure 2.1. Plot showing typical alloying elements effect on the carbide formation in alloyed white iron. (a) Carbide destabilizers; (b) Carbide stabilizers [50].

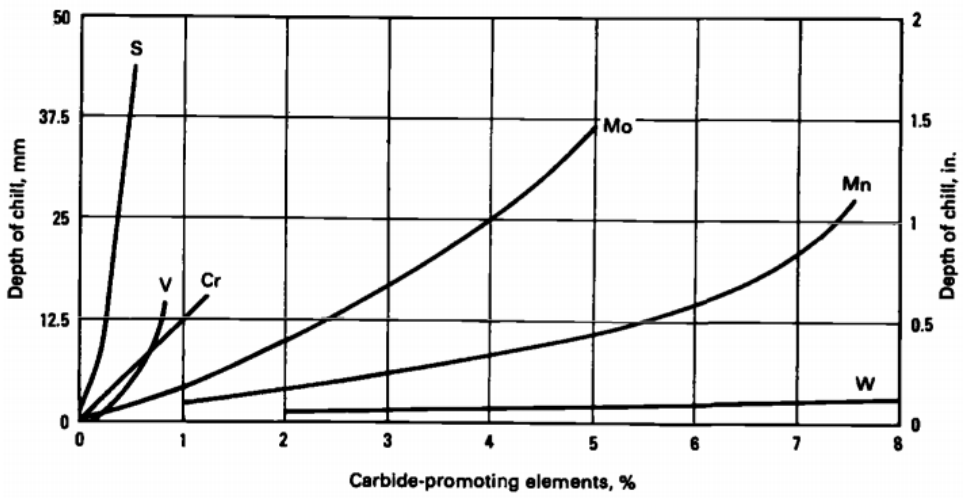

(b)

Figure 2.1. Plot showing typical alloying elements effect on the carbide formation in alloyed white iron. (a) Carbide destabilizers; (b) Carbide stabilizers [50] (cont.).

Figure 2.1 shows the effect of each alloy addition on the carbide formation for alloyed white iron, where "Depth of chill" represents the tendency of carbide formation [50].

Numerous alloyed white irons have been developed by researchers to satisfy various applications. There are two major groups of alloyed white iron for abrasion-resistant application: (1) Ni-Cr white iron; (2) Cr-Mo white iron [51]. Table 2.1 shows the chemical compositions for these alloyed white irons specified in ASTM Standard A532 [52]. Among all grades of alloyed white irons, high chromium white iron is most popular due to its high hardness resulting from the primary formation of M7C3 carbide (1100-1600 HV) during solidification [49]. Numerous of studies have been conducted on the effects of alloy additions on high chromium white iron. Addition of vanadium was found to be powerful with regard to grain refinement [53], [54]. Silicon addition was found to not only refine grains but also increase the volume fraction of the eutectic

carbides [55]. Titanium was reported to be useful in terms of refining primary M7C3 carbides [56], [57], [58], [59], [60]. And addition of niobium was found effective with respect to improving the fracture strength by changing the morphology of eutectic carbides from plate/rod-like shapes to more isotropic shapes [61].

Table 2.1. Chemical compositions of alloyed white irons for abrasion-resistant application.

Alloy Designation	Chemical Composition (wt.%)								
	C	Mn	Si	Ni	Cr	Mo	Cu	P	S
Ni-Cr-Hc	2.8-3.6	2.0	0.8	3.3-5.0	1.4-4.0	1.0	-	0.3	0.15
Ni-Cr-Lc	2.4-3.0	2.0	0.8	3.3-5.0	1.4-4.0	1.0	-	0.3	0.15
Ni-Cr-GB	2.5-3.7	2.0	0.8	4.0	1.0-2.5	1.0	-	0.3	0.15
Ni-HiCr	2.5-3.6	2.0	2.0	4.5-7.0	7.0-11.0	1.5	-	0.10	0.15
12 % Cr	2.0-3.3	2.0	1.5	2.5	11.0-14.0	3.0	1.2	0.10	0.06
15 % Cr-Mo	2.0-3.3	2.0	1.5	2.5	14.0-18.0	3.0	1.2	0.10	0.06
20 % Cr-Mo	2.0-3.3	2.0	1.0-2.2	2.5	18.0-23.0	3.0	1.2	0.10	0.06
25 % Cr	2.0-3.3	2.0	1.5	2.5	23.0-30.0	3.0	1.2	0.10	0.06

High chromium alloyed white iron is widely used in abrasion applications, mainly due to its higher hardness, lower cost relative to other alloy additions and better castability. However, addition of chromium to white iron decreases both thermal conductivity and thermal diffusivity [62], [24], [20], and makes the material more susceptible to adhesive wear [26], [27], [28], [29], [30].

2.1.2. Cobalt-Based Stellite. As a popular group of wear resistant materials, the initial development of Stellite alloys can been retrospected back to the early 1900s by one of the early American automotive pioneers, Elwood Haynes [63], [64]. The name “Stellite” is a trademark of Union Carbide, Stellite Division, and is now owned by Kennametal Inc. [65]. It was initially developed as cutting tools for automotive

manufacturers to replace high speed steel, and use of Stellite permits an increase in the rate of feed on lathe to approximately three times when compared with high speed steel tooling [63]. Stellite was used extensively in munitions production during the World War I [63]. Ever since then, Stellite draws enormous research attention and now exists as a large alloy family.

Chemical compositions for Stellite alloys are mostly cobalt based with additions of chromium, carbon, tungsten, and/or molybdenum. The chromium addition provides strength and corrosion resistance to the alloy, and molybdenum and tungsten additions provide the alloy with strengthening properties. Considerable amounts of other alloy additions such as nickel, vanadium, niobium, and boron, have been added during the development of new Stellite alloys [66], [67]. Up till now, there are dozens of Stellite alloys that have been invented for different applications [68]. Table 2.2 shows the nominal chemical compositions for a select few Stellite alloys that are used in metal-to-metal wear systems. The Stellite alloys with lower carbon content are generally used for cavitation, sliding wear, or moderate galling. Those with higher carbon content are usually selected for abrasion, severe galling, or low- angle erosion. Among all the selected Stellite alloys, Stellite 6 is the most popular, as it provides a good combination of abrasion resistance, galling resistance, cavitation resistance, and corrosion resistance.

Table 2.2. Chemical compositions for selected Stellite alloys.

Alloy Designation	Chemical Composition (wt.%)							
	Co	Cr	W	C	Mo	Ni	V	B
Stellite 1	Bal.	32	13	2.5	-	-	-	-
Stellite 6	Bal.	27	5	1.0	-	-	-	-
Stellite 12	Bal.	30	9	1.8	-	-	-	-
Stellite 20	Bal.	32	17	2.5	-	-	-	-

Table 2.2. Chemical compositions for selected Stellite alloys (cont.).

Alloy Designation	Chemical Composition (wt.%)							
	Co	Cr	W	C	Mo	Ni	V	B
Stellite 21	Bal.	27	-	0.2	5	-	-	-
Stellite 157	Bal.	22	4.5	-	-	-	-	2.4
Stellite 694	Bal.	28	19	1.0	-	5	1	-

A high temperature (750°C) sliding wear test using ball-on-disc apparatus showed that Stellite 6 is approximately five times more wear-resistant compared with Inconel 617 [69]. The exceptional wear performance of Stellite is mainly resulted from its inherent microstructure of hard, complex chemistry carbides dispersed in the CoCr alloy matrix [70], [71]. The price of Stellite is almost solely determined by the market price of cobalt, which makes it much more expensive than other traditional iron based alloys. As a result, Stellite alloys are primarily used for military applications where performance is critical. To utilize the superior wear performance of Stellite at a reasonable price, different deposition technologies have been utilized to deposit Stellite layer onto the surface of a base metal, e.g. plasma transferred arc, tungsten inert gas welding, thermal spraying, and laser cladding [72], [73], [74], [75], [76].

2.1.3. Nickel-Based/Boride Alloy. Due to the relatively high cost of cobalt, attempts have been made to design alternate materials, with nickel as the predominant cobalt substitute [77]. One of the biggest benefits of nickel is the versatility of nickel which can alloy with most metals. For example, complete solid solubility exists between nickel and copper and wide solubility ranges exist between iron, chromium, and nickel [78]. Thus, nickel can be alloyed with many combinations, to create solid solution strengthening, carbide strengthening, and precipitation hardening.

Nickel-based alloys are widely used in applications requiring corrosion resistance and/or heat resistance. However, when it comes to wear application, boron addition is often needed to improve the wear resistance for nickel-based alloys. Table 2.3 shows the chemical compositions for selected nickel-based/boride alloys. In nickel-based/boride alloys, boron promotes a primary, hard, boride phase and carbon acts as a secondary hardening contribution by forming carbides [77]. Because of the fine dispersion of boride and carbide, nickel-based/boride alloy has a typical hardness range of 51 to 57 HRC, which exhibits excellent wear resistance with acceptable corrosion resistance [79]. It was reported that low-stress abrasion resistance, e.g. dry sand rubber wheel test [80], generally increases with increasing boron and carbon contents, namely the hard phase volume fraction for these materials.

Table 2.3. Chemical compositions for common nickel-based/boride alloys.

Alloy Designation	Chemical Composition (wt.%)					
	Ni	Cr	B	Fe	C	Si
Alloy 40	Bal.	7.5	1.5	1.5	0.3	3.5
ERNiCr-A	Bal.	11	1.7	2.8	0.3	3
ERNiCr-A	Bal.	11	2.5	3	0.5	4
ERNiCr-A	Bal.	16	3.5	4	0.7	4

It should be noted that nickel-based/boride alloys are too expensive to be widely used in metal-to-metal wear systems, and are generally adopted as hardfacing for other base materials in surface engineering [81], [79], [82], [83], although small parts requiring a good combination of wear resistance, corrosion resistance, and thermal stability are sometimes made from these alloys.

2.2. WEAR MECHANISMS

Wear is defined by ASTM G40 as “alteration of a solid surface by progressive loss or progressive displacement of material due to relative motion between that surface and a contacting substance or substances” [84]. As one of the most complex subjects in engineering, Bayer remarked [85]: “Wear is not a material property. It is a system response.” There are many terms used to describe wear, however, they are not differentiated and classified very well, which sometimes makes understanding wear mechanisms confusing and difficult. Among all of the terms used to describe wear, the following four wear modes are generally recognized as fundamental and major ones: adhesive wear, abrasive wear, fatigue wear, and corrosive wear [19], [86]. Figure 2.2 shows the schematic images of these four wear modes.

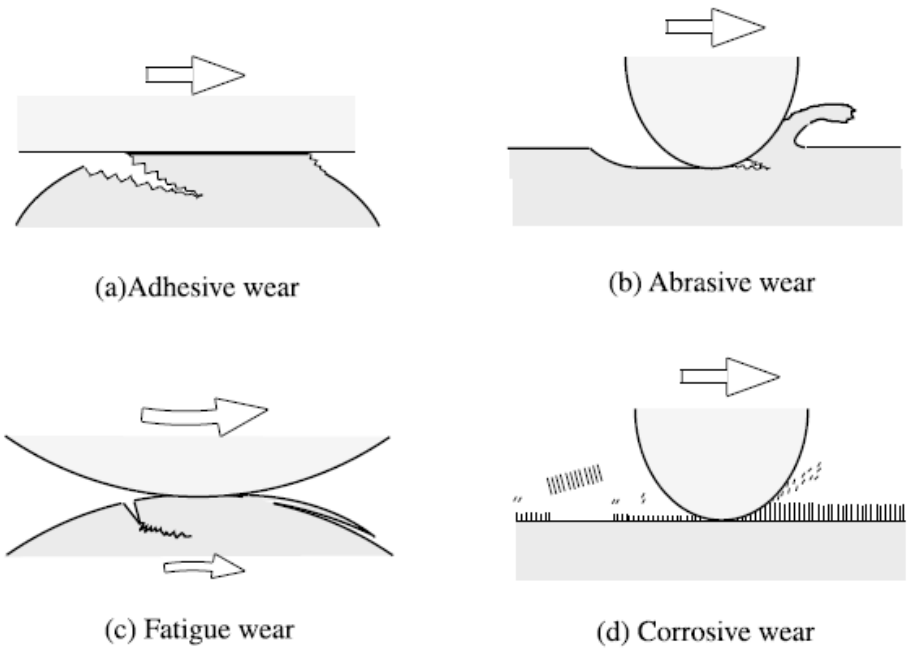

Figure 2.2. Schematic images of four representative wear modes [87].

2.2.1. Adhesive Wear. Adhesive wear is one of the most common forms of wear, which occurs due to localized bonding between contacting solid surfaces leading to material transfer between two surfaces or loss from either surface [88]. There is always a contact load between two surfaces in metal-to-metal wear systems. It should be noted that the entire contact load is often carried only by a very limited area of asperity contacts, due to materials' roughness, which can cause very high contact pressure over the asperity [89]. The high contact pressure can then lead to high localized adhesive bonding strength. If the adhesive bonding strength is high enough to resist relative local sliding, large plastic deformation caused by dislocation is introduced in the contact region [87]. As a result of relative sliding, subsurface plastic deformation may initiate a crack. When the crack propagates and reaches the contact interface, the adhesive wear complete, and a wear particle is generated. The wear particle may deposit on the other surface or come off as a loose particle and contribute to abrasive wear.

Adhesive wear occurs mostly between the same or similar materials, in which cases adhesive bonding strength is very strong. Using dissimilar materials can significantly reduce the adhesive wear rate. However, other factors like chemistry of the interacting materials, atmospheric environment, lubrication, normal load, area of contact, and sliding distance can also affect the adhesive wear rate [90], [91]. It was reported that application of lubricants can significantly reduce the adhesive wear and extend the lifetime of the wear components [89].

2.2.2. Abrasive Wear. Abrasive wear is considered as the most damaging wear mechanism [88]. It usually occurs when a hard, rough surface slides against a softer surface. If the contact interface has interlocking of an inclined or curved contact,

ploughing takes place between two wearing surfaces during sliding. As a result, a certain portion of material is removed and abrasive grooves present on the weaker surface [87]. Abrasive wear resistance is closely related to the material's hardness. Typically, it is believed that there is a linear correlation between the volume loss and the hardness for the similar type of material [92], [9], [93]. However, when the hardness of a material reaches a certain point, the wear resistance does not increase significantly any more [94]. Instead, the controlling factor of a material's wear resistance becomes the removal of the hard phase and the toughness of the matrix [24]. Other factors can also affect the abrasive wear resistance, such as penetration depth, friction force, temperature, and hardness ratio etc.

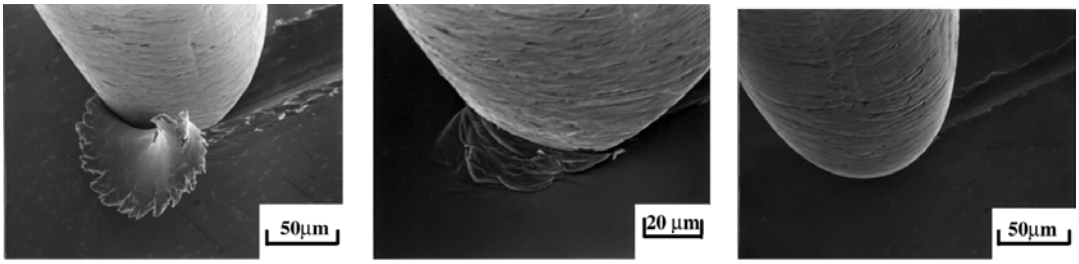

(a) (b) (c)

Figure 2.3. Three different modes of abrasive wear observed by SEM: cutting mode (a), steel pin on brass plate; wedge-forming mode (b), steel pin on stainless steel plate; ploughing mode (c), steel pin on brass plate [95].

To simplify the wear mechanism during the investigation, it is always assumed a single contact point model, where a hard, sharp abrasive is indented and slid against a flat and softer surface, and forming a groove on the abraded surface. Based on the morphology of the abrasive grooves formed, abrasive wear can be further categorized into three modes: cutting, wedge-forming, and ploughing, as shown in Figure 2.3 [95]. In

the cutting mode, a long and curled ribbon-like wear particle is formed, while a wedge-like wear particle is formed at the tip of abrasive groove in the wedge forming mode. Finally, no wear particle is generated and only a shallow groove is formed in the ploughing mode.

2.2.3. Fatigue Wear. Fatigue wear or surface fatigue is caused by a cycling loading during friction [96]. Repeated cycles are not necessary for the generation of wear particles in other major wear mechanisms [91]. Nevertheless, a certain number of repeated contacts are essential for the generation of wear particles in fatigue wear [97]. Based on the number of the contact cycles, fatigue can be further classified as high-cycle fatigue mechanism, and low-cycle fatigue mechanism. The high-cycle fatigue fracture predominantly occurs in the case of elastic contact, while the low-cycle fatigue fracture mostly occurs in the case of plastic contact [87].

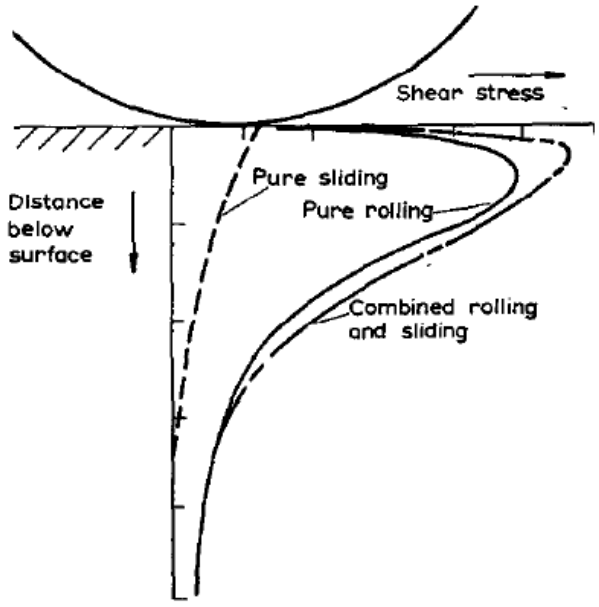

Figure 2.4. Magnitude of shear stress at various depths directly below the point of contact of two hard surfaces in rolling, sliding and combined contact [98].

The mechanism of fatigue fracture is best explained by Burwell [98]. As shown in Figure 2.4, the maximum shear stress occurs not at the contact surface, but at a small distance underneath the contact surface. Therefore, once the maximum shear stress exceeds the material's limit, a fatigue crack will be initiated slightly below the contact surface. The fatigue crack will propagate, then reaches the surface, and eventually flake off leaving the surface badly damaged.

2.2.4. Corrosive Wear. Different from other major wear mechanisms, corrosive wear is a tribochemical wear, which involves two actions [99], [100]. The first one is the alteration of the contact surface chemistry via chemical or electrochemical interaction. This action typically produces a reaction layer on the contact surface, which is always weaker and easier to be removed compared with the original material. The second action is the friction between the contact surfaces. This action typically removes the weakened reaction layer produced in the first action, and offers a fresh surface for the continuation of further corrosive wear [88].

The corrosive wear rate is determined by both chemical reaction rate and reaction layer removal rate. Although corrosive wear has a very minor contribution to the overall cost resulted from wear for industry, a lot of powerful corrosion inhibitors have been invented and added into the lubricant to decrease the chemical reaction rate [17], [18], [101].

2.3. FRICTIONAL HEATING AND CONTACT TEMPERATURE

2.3.1. Frictional Heating. Wear of moving machinery parts always involve frictional processes associated with differences in velocity between two surfaces. It is

believed that nearly all the frictional energy is dissipated as heat or frictional heat in metal-to-metal wear systems [30], [102], [103], [104]. Frictional heating is the process of temperature increase on the contact interface and the temperature will continuously increase until disapative heat removal mechanisms balance the frictional heating. Heat transport via lubrication and thermal transport through the metallic components are the two most important heat dissipation mechanisms. As the surface temperature increases, the tribological mechanisms of wear can change dramatically and these include: (1) changes in the structure and properties of the materials; (2) oxidation of the surface; (3) melting of the contacting parts; (4) softening of the materials; (5) changes in stability and viscosity of the lubricant [30], [31], [105].

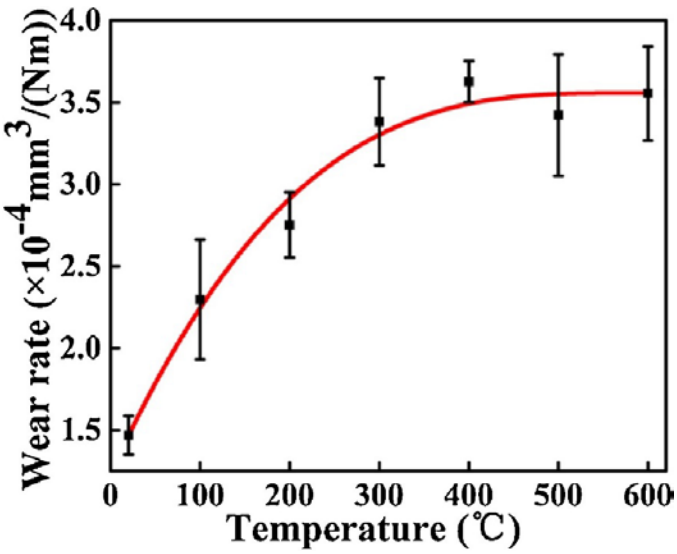

Figure 2.5. Temperature effect on the wear rate of an Al0.25CoCrFeNi high-entropy alloy from a dry sliding wear test [106].

Figure 2.5 shows the temperature effect on the wear rate of an Al0.25CoCrFeNi high-entropy alloy [106], which clearly indicates that the wear rate increases with

increasing testing temperature. It should be noted that the change of the wear rate decreases with increasing testing temperature, while others researchers found that the change of the wear rate increases with increasing the testing temperature [107]. The difference could be resulted from different test condition and material properties.

2.3.2. Contact Temperature. The contact temperature at the wear interface is defined by two quantitative parameters: bulk temperature and flash temperature [108]. In metal-to-metal wear systems, frictional heating occurs over a very limited area of asperity contacts. As a result, the highest temperatures occur close to the real contact areas where the energy is dissipated. Those highest temperatures are of short duration and generally termed as flash temperatures [109], [110]. In contrast, the temperature of the contact area, which does not depend on the instantaneous frictional heat generation, is called the bulk temperature [108]. It was reported that the flash temperature can be as high as 1000 °C [111]. Moreover, some red welding spots were observed by these researchers in high speed sliding experiment.

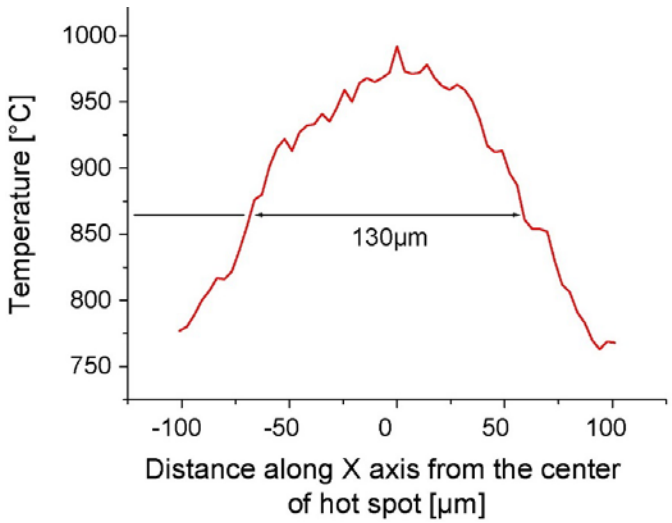

Figure 2.6. Contact temperature profile in a flash temperature study during dry friction process at high sliding speed [111].

Figure 2.6 shows the contact temperature profile near a real contact asperity. It is worth noting that relatively steep temperature gradients exist in the areas near the contact asperity, and these temperature gradients are on the order of few hundred degrees Celsius per micrometer, which indicate that the flash temperature can be significantly different from the bulk temperature.

2.4. EMPHASIS FOR THIS WORK

The purpose of this work is to improve the lifetime of metal-to-metal wear systems by means of introducing graphite falkes into white iron. The additional graphite in white iron can benefit the wear performance of metal-to-metal wear systems from following aspects:

(1) Graphite addition can increase the thermal diffusvity of the material, which in turn reduces the flash heating temperature at the contact interface;

(2) Graphite flakes can be partially pulled out from the original sites and leave some pockets on the wearing surface. Those pockets can work as resivors to hold lubricant and decrease the wear rate;

(3) Graphite flakes pulled out can be abraded into small particles and dispersed across the wearing surface. Those dispersed graphite can work as lubricant and reduce the friction coefficient between two wearing surfaces.

PAPER

I. MICROSTRUCTURAL CHARACTERIZATION AND FAILURE ANALYSIS OF A WEAR RESISTANT, HIGH MOLYBDENUM AND CHROMIUM WHITE IRON

Jie Wan[1], David C. Van Aken[1], Jingjing Qing[2], Mingzhi Xu[2]

[1]Missouri University of Science and Technology, Rolla, MO 65401, USA

[2]Georgia Southern University, Statesboro, GA 30460, USA

Tel: 573-578-3874

Email: jwvt7@mst.edu

Keywords: Wear-Resistant Material, High Molybdenum and Chromium White Iron, TKD, Failure Analysis, White Layer, Micro-Galling

ABSTRACT

An Fe-18Cr-3.3C-15Mo-1.65V white iron used for metal-to-metal contact wear resistance was field tested to failure. Microstructural analyses were performed using optical microscopy and scanning electron microscopy with phase identification performed using a transmission Kikuchi diffraction (TKD) technique. A solidification sequence was proposed by correlating thermodynamic equilibrium calculations with the distribution and size of the phase constituents. Field returned components were analyzed after approximately 10,000 service hours. Micro-galling defects exhibited regions of material flow and white layer formation. The white layer was determined to be nanocrystalline with average grain size less than 15 nm. Phase constitution of the white

layer was similar to the basemetal and contained M2C, M7C3, austenite and ferrite. Cracking of the white layer produced both surface pits and abrasive particles that lead to wear scars and eventual leakage of the lubricant protecting the wear components.

1. INTRODUCTION

Metal-to-metal wear systems are widely used in various industrial machineries that incorporate rolling element bearings [1], gears [2], and dynamic rotary seals [3]. In the case of dynamic rotary seals, failure of worn surfaces can lead to damage of more costly components and significant machine downtime [4]. White cast irons, Stellite, Ni-Resist cast irons, tungsten carbide hard faced steel, and various ceramic systems (aluminum oxide or silicon carbide) have been used in dynamic rotary seals [3], [5], [6], [7]. High chromium white irons are the least expensive and exhibit good abrasive wear resistance as a result of large M7C3 carbides with Vickers hardness 1100 to 1600 HV [8], [9], [10], [11], [12], [13].

Frictional heating is a major concern with dynamic rotary seals, and heat dissipation is often regulated by lubrication. Catastrophic failure of the dynamic rotary seal often follows loss of lubrication and overheating of the contact surfaces. Initially, frictional heating occurs over very small area of asperity contacts resulting in high local temperatures for short time durations. The maximum local temperature has been called a flash temperature [14], [15], [16]. In dry friction, flash temperatures as high as 1000 °C have been reported [17]. High surface temperatures can negatively impact tribological behavior and even cause failures by (1) changes in the microstructure and properties of

the contacting materials; (2) oxidation of the surfaces; (3) local melting of the contacting parts; (4) softening of the materials; and (5) changes in stability and viscosity of the lubricant [18], [19]. It is generally observed that the wear rate increases exponentially with temperature [20], [21], [22], [23], [24].

One of the major problems caused by excessive frictional heating for metal-to-metal wear systems is the formation of white layers on the contacting surfaces [25], [26], [27]. The term “white layer” or “white etching layer” refers to an etching resistant layer that appears white and featureless when viewed using an optical microscope [28]. In some studies the white layer has been identified as untempered martensite [29], [30], [31]. The white layer is an extremely hard and brittle structure, and can cause crack formation and product failure [32], [33], [34], [35]. It was reported that the hardness increase resulted from the formation of the white layer can be as high as 180% compared with the original substrate [36]. The high hardness difference between the white layer and substrate leads to high stress concentrations that accelerate contact fatigue crack initiation and propagation in these areas [37], [38]. While most studies indicate that the white layer has a detrimental influence on wear components, Cho et al. [36] found that the white layer can increase wear resistance in a low loading condition. This advantage diminishes, as the white layer begins to delaminate at higher loads. While most of the past works related to white layer were carried on steels [39], [40], [41], [42], [43], [44], [45], the authors are unaware of any study on white layer in cast iron. Thus, phase constitution, chemical composition, and failure mechanism remain unknown for white layer formation in cast irons.

In this paper, a wear resistant, high molybdenum and chromium white iron used for metal-to-metal wear systems has been investigated. This material is based upon a hard-facing alloy that was chemically modified to produce a castable white iron. A comprehensive phase characterization was carried out, and failure analysis was conducted from a field returned component made from this material.

2. MATERIAL AND METHOD

2.1. MATERIAL

High-purity charge materials were melted in an induction furnace and poured into shell molds to produce commercial sliding wear parts. Chemical composition for the white iron is shown in Table 1.

Table 1. Composition (wt.%) analyzed using an optical emission spectrometer and a Leco C/S analyzer.

Fe	C	S (ppm)	Si	Mn	Ni	Cr	Mo	V
Bal.	3.30	405	0.26	0.50	0.49	18.00	15.00	1.65

2.2. SAMPLE PREPARATION AND CHARACTERIZATION

2.2.1. As-Cast Samples. Metallographic samples were prepared for both wearing surface (in-plane) and cross section from the wear component casting. Standard metallogrphic methods were used to prepare the specimens with a final polish using 0.1μm diamond paste. Marble's reagent [46] was used to etch the specimens to reveal

different phases in the material. A Nikon FX-35DX camera was utilized to capture the optical micrographs.

Samples were also prepared by means of electrolytic deep etching or polishing using a solution of 60 vol.% methanol, 34 vol.% butoxyethanol, and 6 vol.% perchloric acid [47]. Deep etched structures were used to observe the 3-dimensitional microstructure using an FEI Helios NanoLab 600 scanning electron microscope (SEM). A separate sample was prepared by dual-Jet electropolishing to study the phase constituent via transmission Kikuchi diffraction (TKD) technique. SEM operation parameters are shown with each of the SEM images. The electrolytic deep etching and polishing parameters are reported in Table 2.

Table 2. Operation parameters for electrolytic deep etching and polishing.

Sample	Temperature (°C)	Voltage (V)	Current (mA)
Electrolytic Deep Etching	-25	20	20
Dual-Jet Electropolishing	-40	60	30

2.2.2. Field Returned Wear Component. Cast parts were also assembled into a metal-to-metal wear system for field testing. The components failed after 10,000 service hours with failure defined by excessive oil leakage. Failure analysis was then performed on the worn components using an optical microscope and an SEM. Samples for optical microscope were prepared using the same procedure aforementioned in Section 2.2.1 to study the cross section of the failed component. Samples for SEM were sectioned to preserve the wearing surface of the failed component and investigate cause of the failure. As shown in Figure 1, A TEM sample was extracted from a region containing white layer

formation (indicated by arrows in Figure 1(a)) using a focused ion beam (FIB) technique. Bright-field (BF), dark-field (DF), and selected area diffraction (SAD) techniques were used to investigate the microstructure of the white layer. Operating parameters for SEM and FIB are provided in the figure caption of each SEM image.

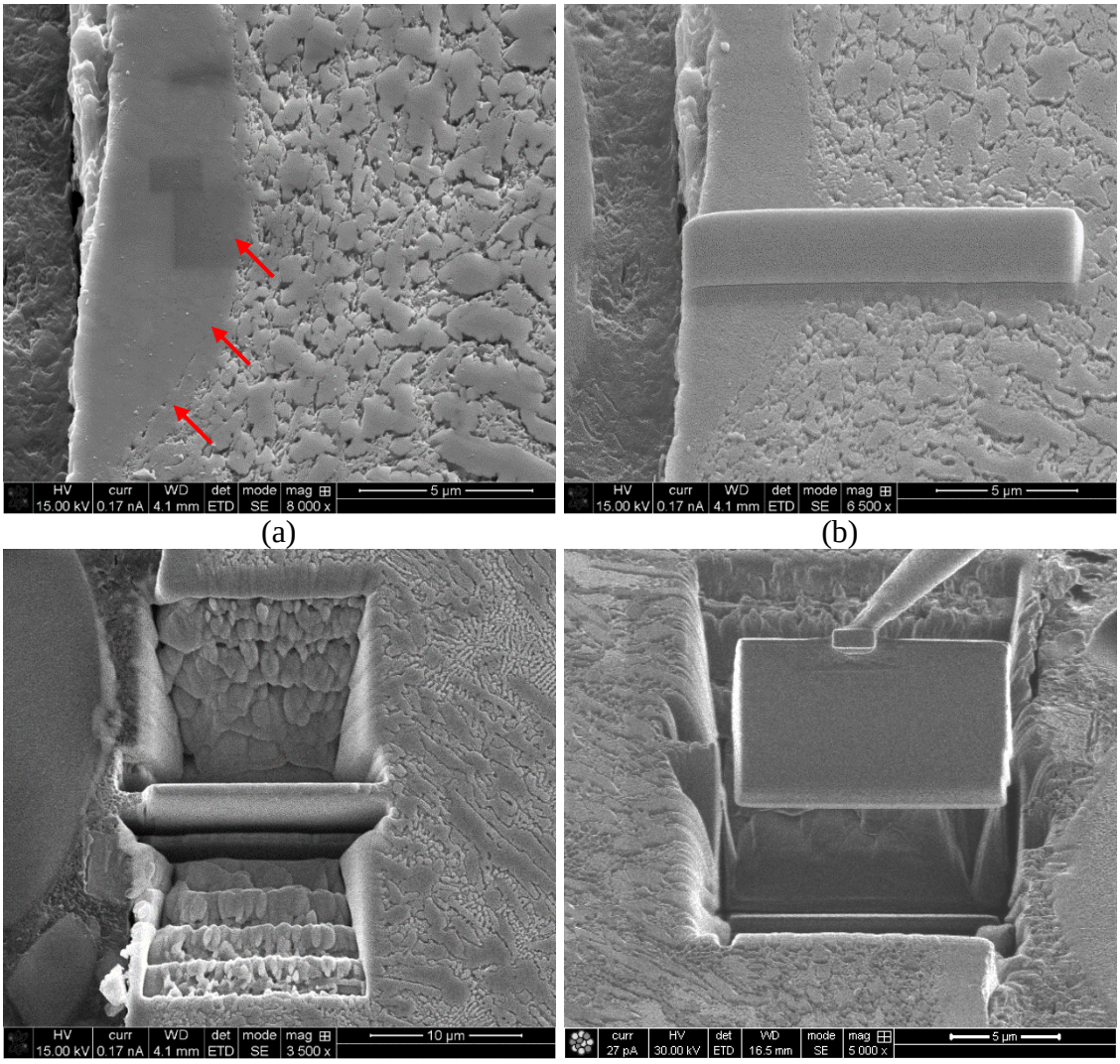

Figure 1. FIB-SEM sample preparation: (a) SEM image before FIB; (b) Pt deposition on the selected area for site-specific sample preparation; (c) Removal of material adjacent; (d) Lift-out of the TEM sample using a micro-manipulator. Arrows indicate the white layer formed on the wearing surface.

3. RESULTS

3.1. METALLOGRAPHIC RESULTS

3.1.1. Optical Microstructure. Figure 2(a) is an optical image showing the microstructure of the casting center, which was about 8 mm away from the casting surface. At least three different features were distinguished in Figure 2(a): hexagon (arrow with straight end), white segment with brownish tint boundary (arrow with round end), and network structure (arrow with rhomb end). Figure 2(b) shows the microstructure from the casting surface, also the wearing surface. As the cooling rate at the casting surface was faster, all three foresaid features were finer (<1 μm) than those in the casting center. The corresponding features in the casting surface are also marked by the same type of arrows, as shown in Figure 2(b).

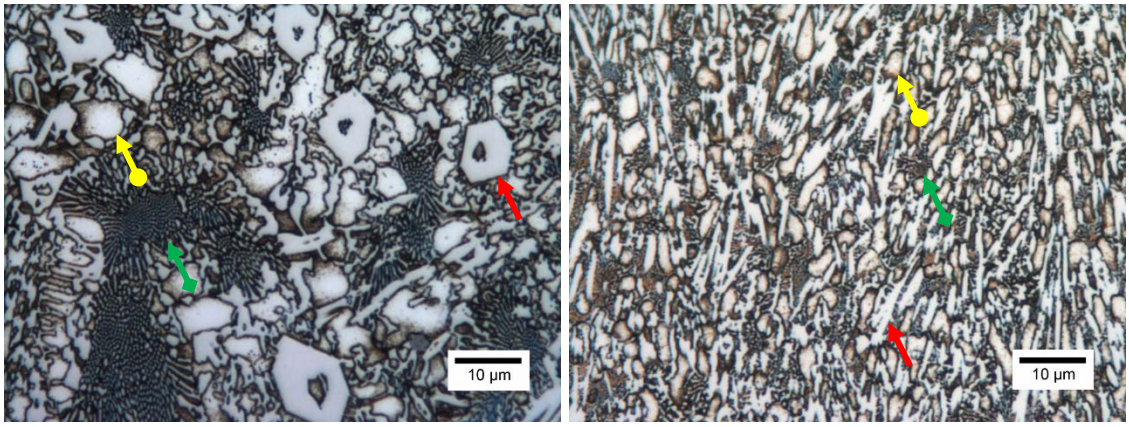

(a) (b)

Figure 2. Marble's reagent etched microstructure from: (a) Casting center; (b) Casting surface. Three features can be observed including: hexagon indicated by arrows with straight end, white segment with brownish boundary indicated by arrows with round end, and network structure indicated by arrows with rhomb end.

3.1.2. Electrolytic Deep Etching Microstructure. Deep etching produced a surface where carbides stood in relief and these surfaces were imaged using an SEM. Figure 3 shows the electrolytic deep etched microstructures taken from the casting subsurface, which was about 3 mm away from the casting surface. As shown in Figure 3(a), many finger-like rods were observed, which were named as columnar carbides. Figure 3(b) is a magnified image of Figure 3(a). In addition to the rod-like columnar carbide, a second rod solidification product was identified, which was termed as 2ry columnar carbide. Figure 3(c) and (d) revealed that there were also very few but relatively large carbides (~15um) in this alloy, which were named as Crocodile Jaw Shaped (CJS) carbide. According to Liu's work [48], the CJS carbides are primary M7C3 carbides, which were formed into crocodile jaw shape due to its unique coalescence process during growth.

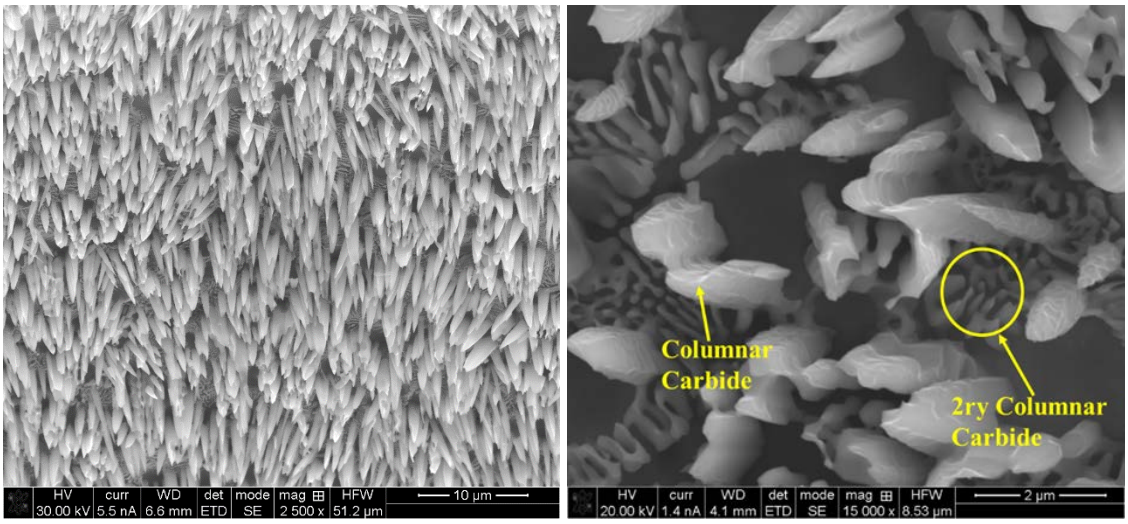

(a) (b)

Figure 3. SEM images showing the electrolytic deep etched microstructure taken from the subsurface of the casting.

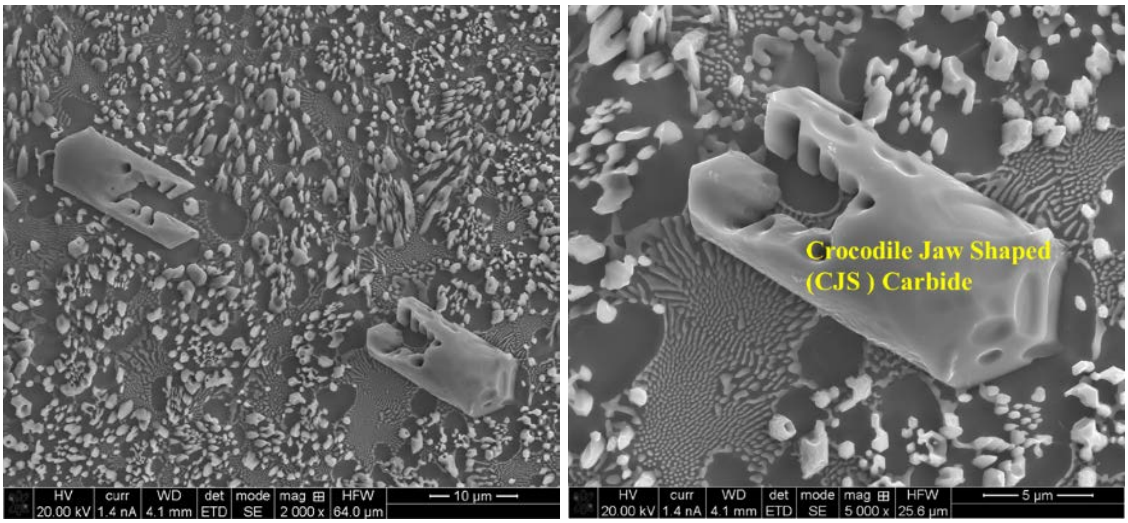

(c) (d)

Figure 3. SEM images showing the electrolytic deep etched microstructure taken from the subsurface of the casting (cont.).

The columnar carbides in Figure 3(a) appeared denser than in Figures 3(b)-(d). This is possibly due to the imaging angle difference, as Figure 3(a) was taken at 20° tilt, while Figures 3(b)-(d) were taken at no tilt. Overall, there are four different phases revealed by electrolytic deep etching: CJS carbide, columnar carbide, 2ry columnar carbide, and matrix.

3.1.3. TKD Phase Mapping. A TKD technique using transmitted electrons was used to identify the microconstituents that were smaller than 100 nm. TKD analyses using high operation voltage (30 kV), provides better spatial resolution than either secondary or backscattered electrons, which can be less than 10 nm [49], [50]. Results are shown in Figure 4 from the casting subsurface, which was about 3 mm away from the casting surface. The white rectangle in Figure 4(a) indicated the area where phase mapping and EDS mapping were performed. Phase constituents are identified in Figure 4(b) and EDS mappings are shown in Figure 4(c)-(h). As shown in Figure 4(b), there

were four phases in this material including: BCC (ferrite), FCC (austenite), M7C3, and M2C. Combining the phase mapping with the EDS mapping, the following conclusion can be drawn: (1) the matrix was rich in Fe, and it consisted of ferrite and retained austenite; (2) the columnar carbides were M7C3 carbides, and they were rich in Cr, V and Mn; (3) the 2ry columnar carbides were M2C carbides, which were rich in Mo and V. It should be noted that most of the signal for ferrite matrix between 2ry columnar carbides was blocked, since M2C carbides were much taller than ferrite.

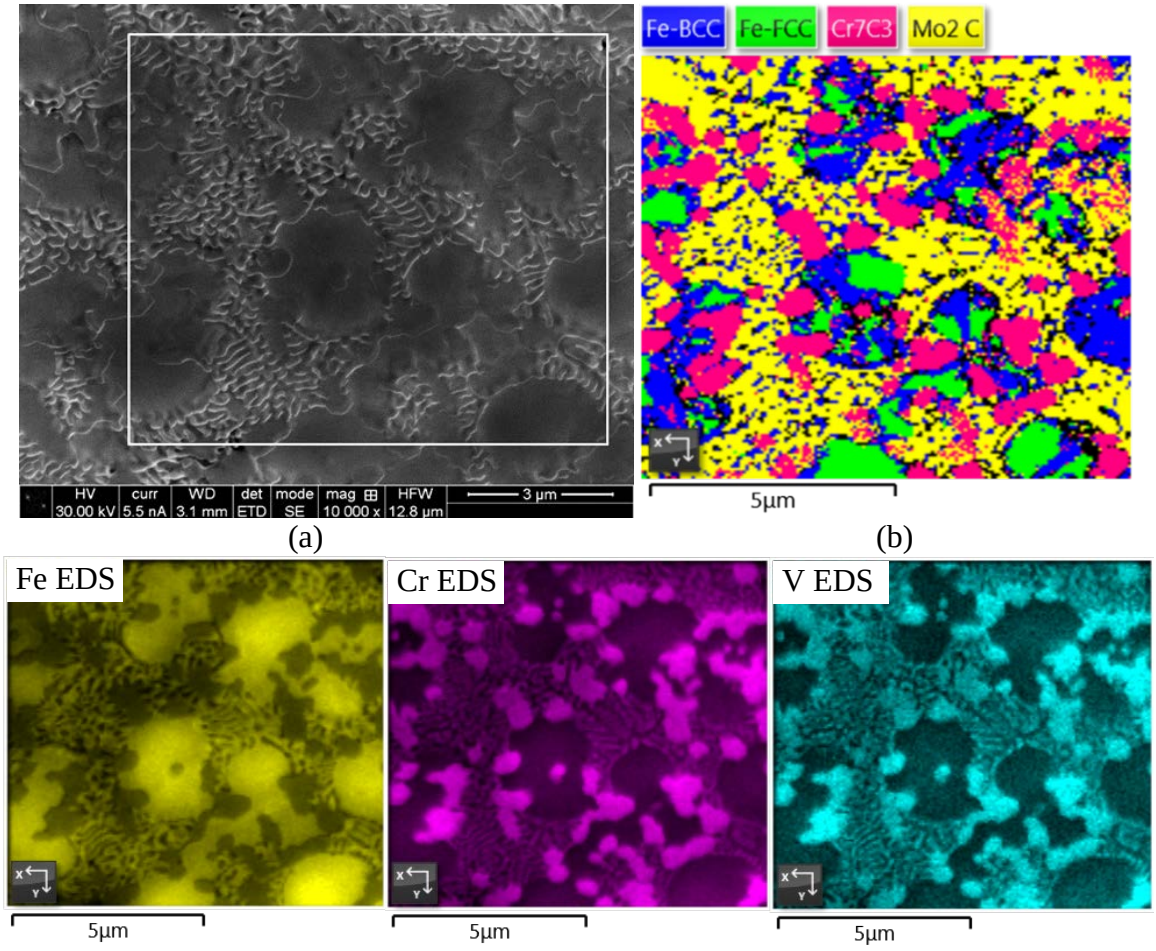

Figure 4. TKD images from the casting subsurface showing: (a) TEM image; (b) Phase mapping on the white box in (a); and (c)-(h) EDS mappings for Fe, Cr, V, Mo, C, and Mn, respectively.

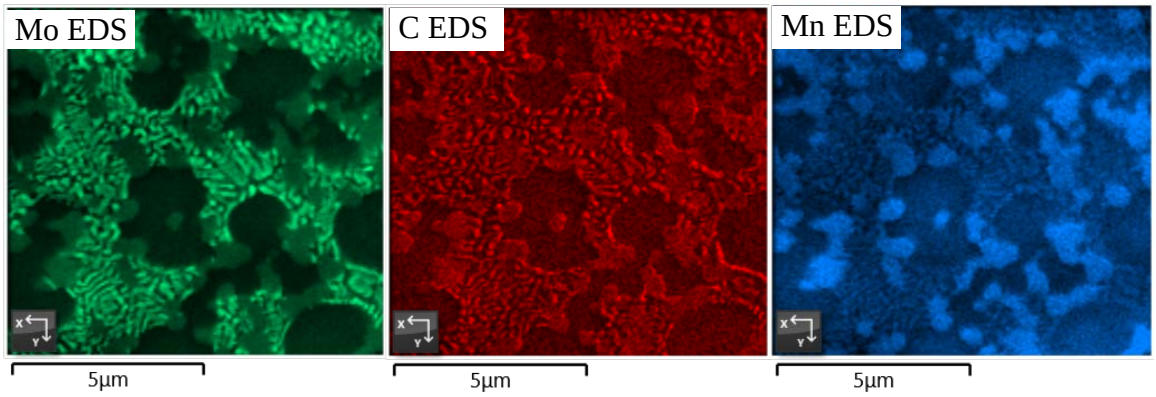

(f) (g) (h)

Figure 4. TKD images from the casting subsurface showing: (a) TEM image; (b) Phase mapping on the white box in (a); and (c)-(h) EDS mappings for Fe, Cr, V, Mo, C, and Mn, respectively (cont.).

3.2. FAILURE ANALYSIS

Failure analysis was performed on a field returned metal-to-metal wear component after failure and leakage of the lubricant. The observation results of the cross section and the wearing surface are reported.

3.2.1. Cross Section. It should be noted that the wear contact position changes with time during operation with the border of the actual contact area propagating from one side to the other during service. Figure 5 shows optical images of the cross section with the wear surface at the top of the image. The final wear point appears as a peak on the surface in Figure 5(a) with unworn surface to the left and the worn surface to the right. The unworn surface is protected by clean lubricant when in operation, whereas the worn surface can be contaminated by debris from the working environment. The image shown in Figure 5(b) was observed approximately 10 µm to the right of Figure 5(a). A comparison of the unworn surface with the worn surface yields two observations. The columnar M7C3 eutectic structure is nearly normal to the unworn surface due to

directional solidification, whereas this same structure appears tilted towards the final point of contact. In addition, many of these carbides seem to be fractured below the surface. The depth of deformation continuously decreases towards the point of final contact. A maximum depth of 32μm was observed on the worn surface. Secondly, a non-etching white layer appears on the worn surface, but not at the point of final contact.

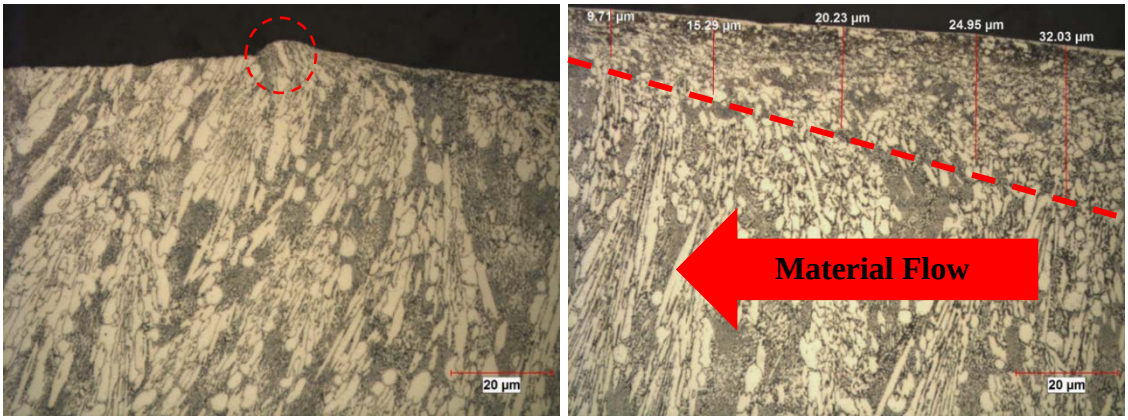

(a) (b)

Figure 5. Optical micrographs on the cross section of the field returned component showing: (a) final wear point on the wearing surface; (b) affected depth next to the final wear point.

Figure 6 is also an optical micrograph of the cross section showing some white layer formation on the worn surface. White layer refers to an etching resistant layer formed on the contact surface, which appears white and featureless [28]. It is believed that white layer is a result of excessive frictional heat and repeated mechanical load [39], [51]. Figure 6 was taken from an area that was worn for a much longer time compared with the worn surfaces shown in Figure 5. As a comparison, there was no white layer observable in Figure 5(a), thin white layers in Figure 5(b), but thick white layers (~4 μm)

in Figure 6. Cracks can also be observed within the white layer, which are indicated by arrows.

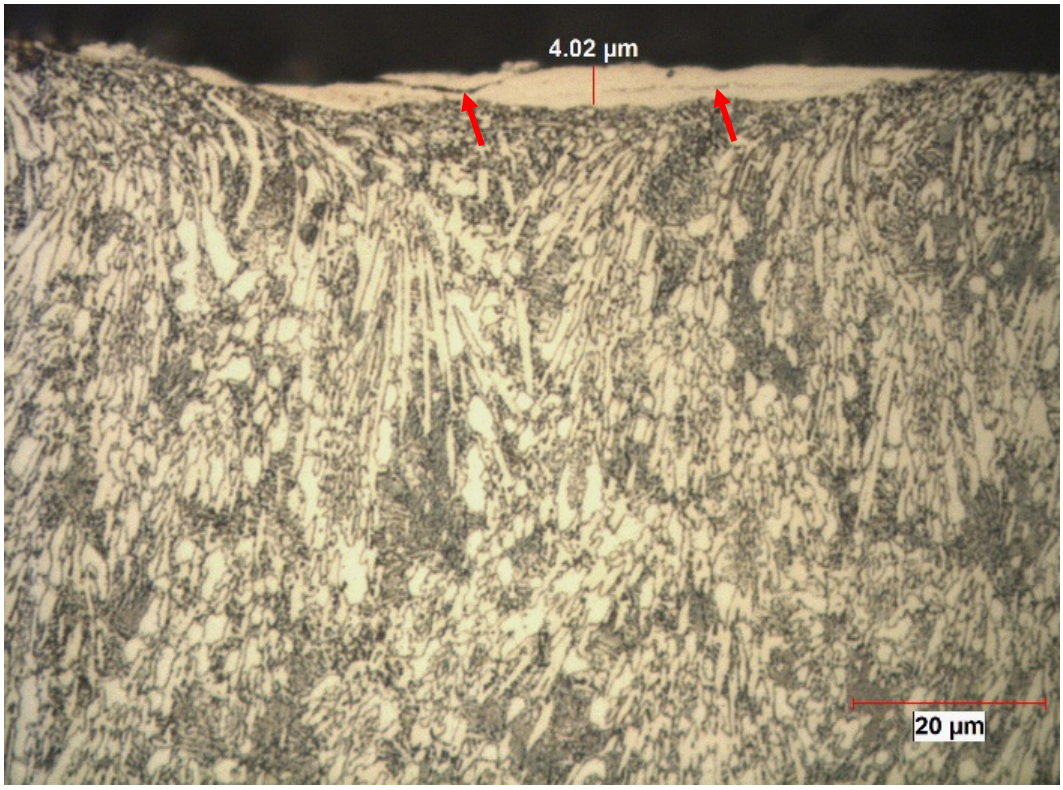

Figure 6. Optical micrograph on the cross section of the field return component showing white layer on the worn surface. Arrows indicate cracks within the white layer.

3.2.2. White Layer. Figure 7 shows the bright-field (BF) TEM images for the white layer. In Figure 7(a), the dashed line shows the interface between the white layer and the deformed substrate, and the dashed circle shows where the selected area diffraction (SAD) shown in Figure 8 was conducted. The grain sizes in the deformed substrate were much bigger than those in the white layer. Figure 7(b) is a high magnification BF TEM image taken from the white layer, and the grain sizes were estimated to be approximately 15 nm.

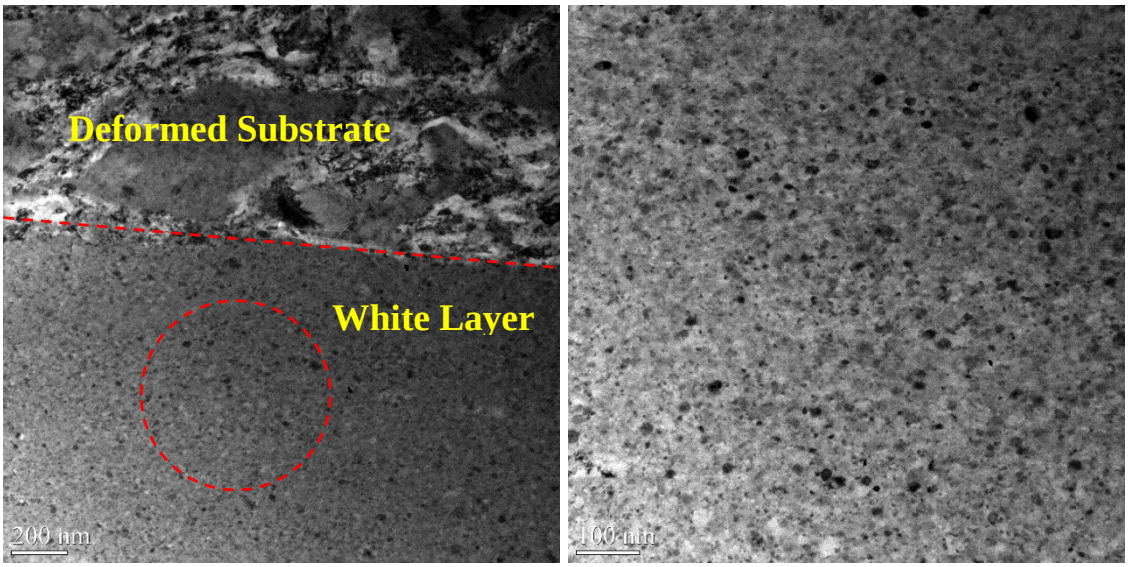

(a) (b)

Figure 7. BF TEM images of the white layer. (a) The area under the dashed line shows the white layer, and the dashed circle shows where the SAD was conducted; (b) High magnification image on the white layer.

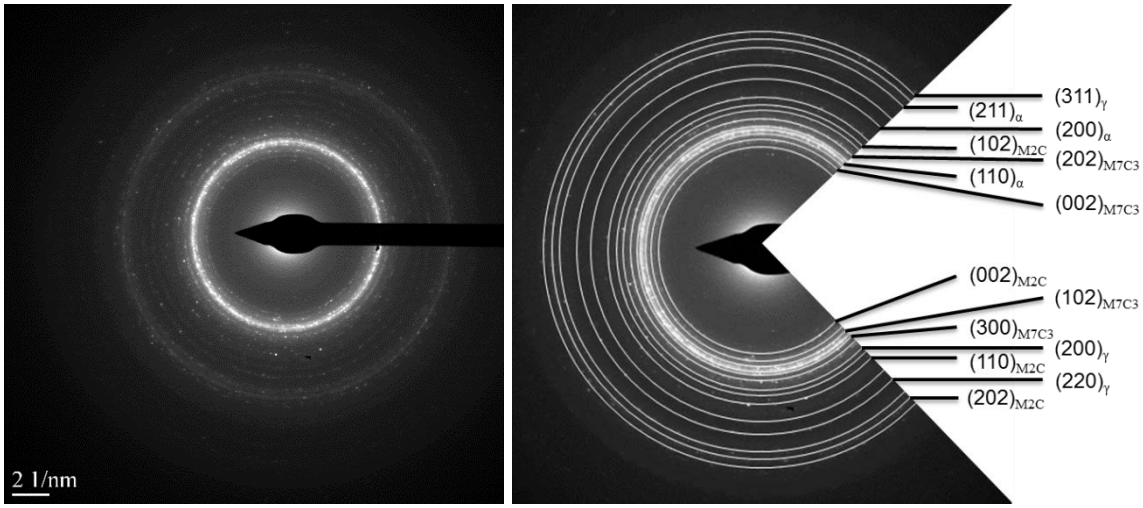

(a) (b)

Figure 8. TEM images showing (a) SAD pattern for the white layer; (b) Indexing of the SAD pattern.

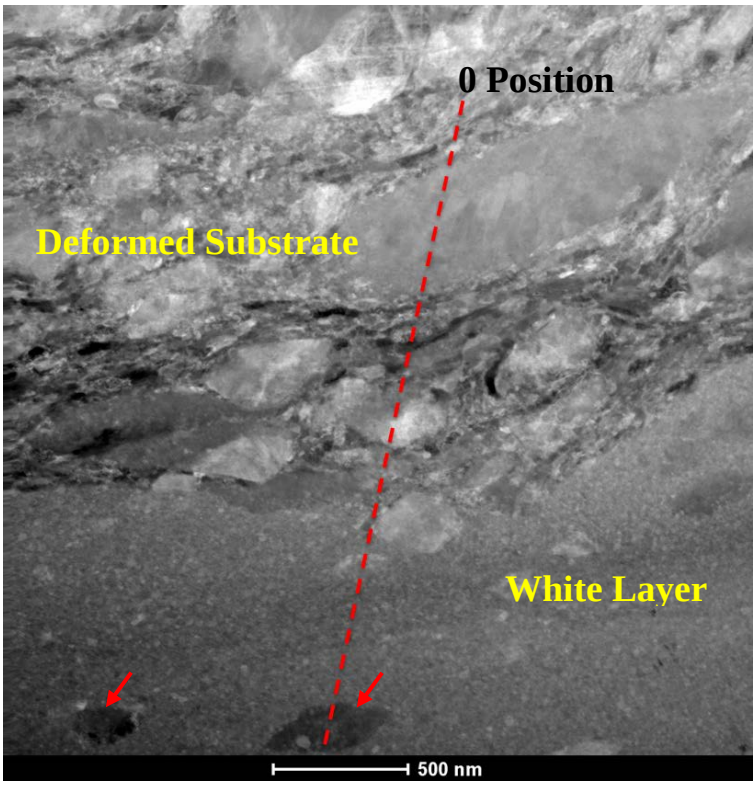

(a)

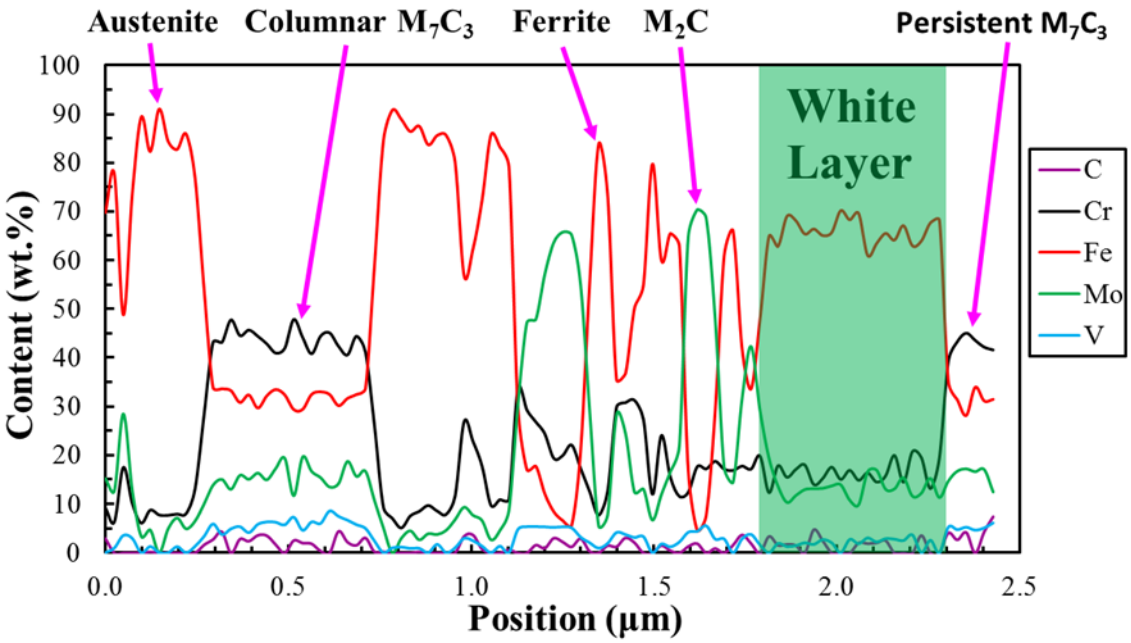

(b)

Figure 9. Pictures of (a) TEM DF image with the dashed line showing the line scan position, and arrows indicating the persistent carbides; (b) Line scan spectrum profile.

Figure 8(a) shows the SAD pattern for the white layer, and Figure 8(b) shows the indexing of the SAD pattern, where phases and planes are labeled for each reflection. As shown in Figure 8(b), the reflections for the white layer have been indexed as ferrite, austenite, M7C3 carbide, and M2C carbide. In general, the white layer exhibited the same phase constituents as the original microstructure analyzed via TKD technique shown in Figure 4.

Figure 9(a) shows a dark-field (DF) TEM image containing a white layer and a portion of the deformed substrate. Figure 9(b) shows an EDS line scan conducted along the dashed line in Figure 9(a) to compare the chemical composition of the white layer and the deformed microstructure. The line scan terminated at a dark-contrast feature approximately 200nm in size contained in the white layer. The composition of this feature is similar to an M7C3 carbide. The proximity and size of this feature would suggest that it is a persistent constituent of the original cast microstructure. This type feature was not observed near the contact surface of the white layer. Moreover, the phase constituents in deformed substrate can be speculated from the line scan spectrum profile, as labeled in Figure 9(b). However, the white layer showed a more uniform chemical composition compared with that in the deformed substrate, excepted for the persistent carbide, as shown in Figure 9(b). This could be resulted from the finer microstructures within the white layer.

3.2.3. Worn Surface. An SEM was used to observe the worn surface of the field returned component. As shown in Figure 10, three characteristics can be observed on the worn surface and are labeled in the SEM images including: Attachment, Cutting, and Micro-Galling. Generally, attachment is a characteristic for adhesive wear and result

from material transfer during asperity contact, whereas cutting is a characteristic for abrasive wear. Micro-galling is initiated by adhesive wear, but involves subsurface fatigue cracking that culminates with spallation of the surface.

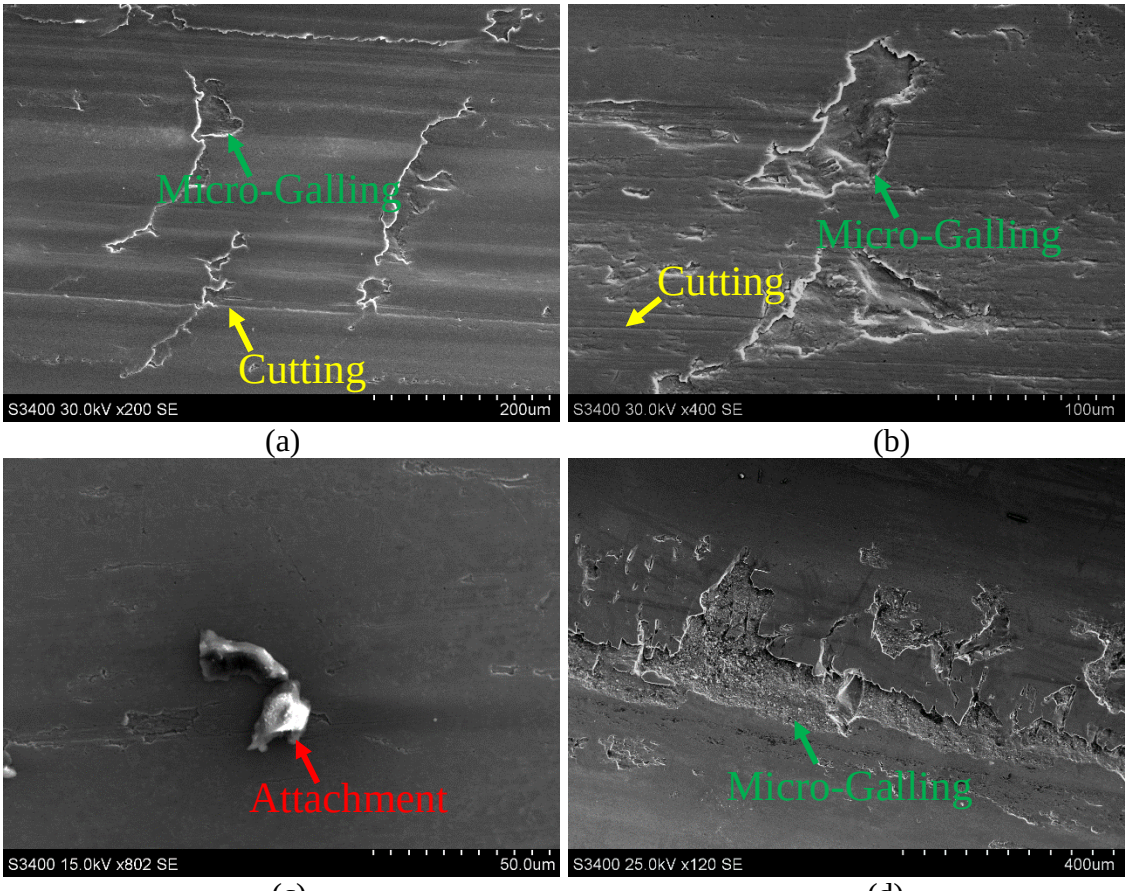

Figure 10. SEM images showing the worn surface of a field returned component.

4. DISCUSSION

4.1. SOLIDIFICATION SEQUENCE AND MICROSTRUCTURAL CORRELATION

As shown in Figure 11, the phase evolution for this alloy during equilibrium solidification was calculated using Temperature Step Calculation module provided in

JMatPro software (version 9.1). Figure 11(a) shows the overall phase evolution from 1300 °C to 700 °C, while Figure 11(b) shows the solidification evolution in more detail from 1270 °C to 1150 °C. A liquidus temperature of 1243 °C and a solidus temperature of 1179 °C are predicted. Primary solidification of M7C3 carbide is predicted with two subsequent eutectic reactions. At 1194 °C, M7C3 forms with austenite during the first eutectic reaction (binary). A second eutectic reaction (ternary) occurs at 1187 °C to form M2C in combination with austenite and M7C3. Austenite transforms to ferrite starting at 803°C.

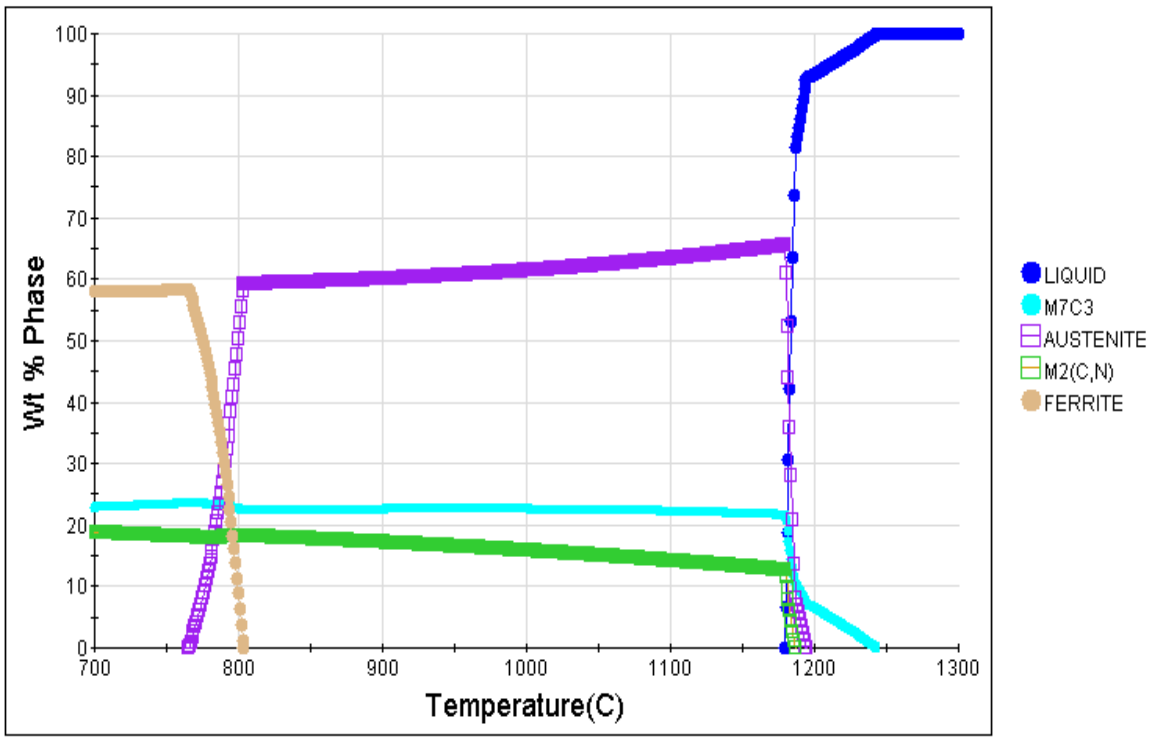

(a)

Figure 11. Diagrams showing phase evolution calculated using JMatPro during solidification from 1300 °C to 700 °C (a), and from1270 °C to 1150 °C (b). It should be noted that M6C was excluded for these calculations.

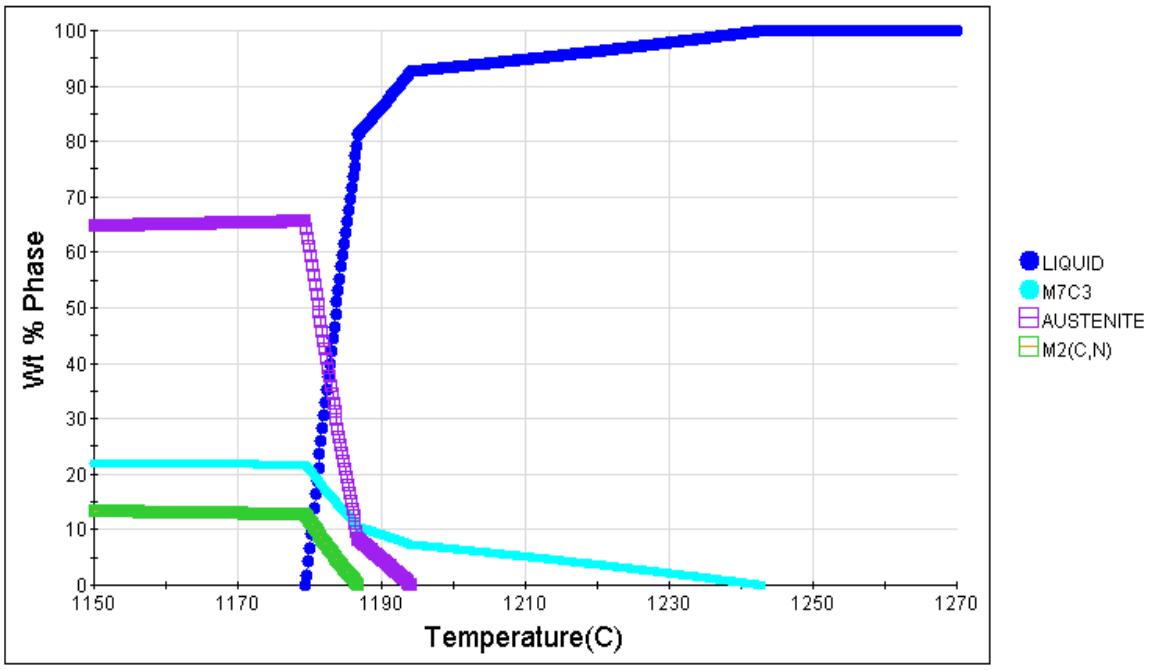

(b)

Figure 11. Diagrams showing phase evolution calculated using JMatPro during solidification from 1300 °C to 700 °C (a), and from1270 °C to 1150 °C (b). It should be noted that M6C was excluded for these calculations (cont.).

A complete explanation of the cast microstructure can now be given based upon a correlation of the thermodynamic calculations and the observed scale and phase distributions. Figure 12 depicts all of the major transformations during solidification. The CJS carbide is now identified as the primary M7C3 phase that initially forms at the liquidus temperature of 1243°C. The faceted character of M7C3 is easily identified in the coarse rod eutectic microstructure and this can be identified as the first eutectic reaction beginning at 1194°C, i.e. L->M7C3+austenite. The ternary reaction, L-> austenite+M2C+M7C3, appears to be mostly austenite and M2C; however, close examination of Figures 3(d), 4(b) and 12 shows regions where M7C3 is present within this eutectic microstructure. The scale differences between the two eutectic

microstructures also agree with this proposed sequence, since phases formed at higher temperatures have a kinetic growth advantage and will be larger in size. It should be noted that at the casting surface, as shown in Figure 2(b), the primary M7C3 may not be distinct from the M7C3 formed during the first eutectic reaction as a result of the chill induced by the mold producing both undercooling and rapid solidification. Retained austenite observed at room temperature in the first eutectic reaction may also be an effect of scale and the ability to resolve the phase constituents or composition differences in the formed austenite. It should be noted that in a similar alloy containing higher silicon content (1.34 vs. 0.26 wt.%), a M6C eutectic ("fishbone" morphology) forms instead of the M2C eutectic as observed in this study [52]. It is known that silicon can be incorporated into the M6C carbide as observed in 2.25Cr-1Mo type steels [53] and silicon destabilizes M2C in favor of M6C in nickel based alloys as reported by Xu et al. [54], [55].

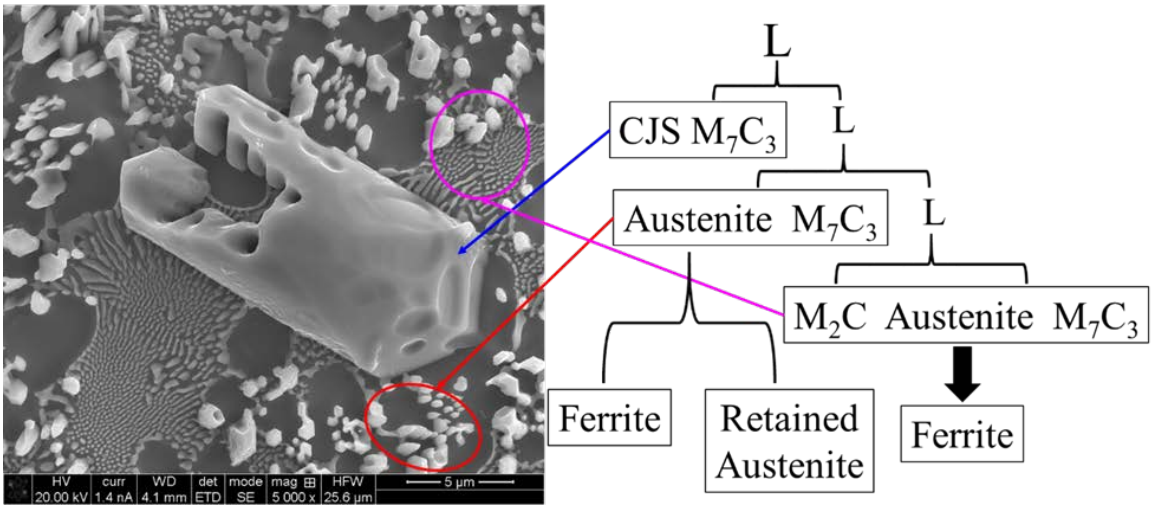

Figure 12. Schematic showing the correlation between the microstructure and the solidification sequence. SEM image was taken from the casting subsurface (3mm down).

4.2. WHITE LAYER

While most of the past works related to white layer were carried on steels [39], [40], [41], [42], [43], [44], [45], the authors are unaware of any study on white layer formation in white cast iron. According to Hosseini's work [56], the grain size in white layer formed by hard turning of AISI 52100 steel was in the range of 30 nm to 80 nm. The finer grain size in this study may be attributed to the multiphase structure and mechanical mixing over a longer time of contact. Grain size in multiphase microstructures are prone to pinning, which prevents grain growth. It was reported by Hosseini [56], that the contact time in hard turning was in the range of 45 to 400 milliseconds.

In the current study, white layer grain structure produced complex ring diffraction patterns (see Figure 8) and is similar to Hosseini's works [43], [56]. In their studies, white layers were induced by hard turning. Meanwhile, the as-cast steel microstructure in their study was fully martensitic and bainitic, and white layers were divided into two groups due to different formation mechanisms proposed: thermally induced, and mechanically induced. The mechanically induced white layer contained ferrite and cementite, whereas the thermally induced white layer consisted of austenite, martensite and cementite [56]. Current study was unable to differentiate between BCT martensite, tempered martensite, or ferrite and the authors labeled the phase as ferrite.

Severe plastic deformation has been found to be effective in refining the grains of metals and alloys [57], [58]. The fine grain size and nanocrystalline structure of the white layer are remarkably similar to those produced under severe plastic deformation [59]. It was reported that high pressure torsion can produce a nanocrystalline structure

with a grain size as small as a few nanometers [60]. Neglecting the possible differences in thermal history and material type, the high strain and dynamic loading accompanied with adiabatic shear associated with the wear components in metal-to-metal wear systems are very similar to the high pressure torsion experiments. Therefore, it is likely that the white layer in this study was mechanically induced via severe plastic deformation mechanism. Frictional heating enhanced the adhesive bonding strength on the contact interface, which in turn assisted the formation of the white layer. Similar white layer formation mechanism has been describe on the investigation of white layer formed on high-speed railway brake discs [61].

Refinement of grains in metals is generally controlled by dislocation activities, which subdivide the original coarse grains. Therefore, the white layer has a refined grain size, while its phase constituent is the same as the original microstructure, as is characterized by SAD diffraction shown in Figure 8. However, refinement of carbide is more difficult due to its high hardness [8], [13], and lack of sufficient slip systems [56], [62], [63]. The presence of persistent M7C3 carbide in the white layer can be speculated as a result of the combination effect from high hardness, fewer slip systems, and bigger original size (primary M7C3). It should be noted that primary M7C3 growth was suppressed by fast cooling rate near casting/wearing surface. The distance from primary M7C3 to casting surface affects cooling rate, which can in turn affect the original size of primary M7C3. The distance from persistent M7C3 observed in Figure 9(a) to the worn surface was estimated to be approximately 1.3 μm.

It was reported that the hardness of the white layer can be as high as 180% of the original substrate [36]. The high hardness difference leads to a higher stress

concentration within the white layer and the interface between the white layer and the substrate. Therefore, the white layer can not only initiate cracks but also accelerate their propagation [37], [38]. Based on the crack propagation direction, Yang et al. [64] further proposed two failure models: (1) along a path parallel to the wearing surface; (2) along a path at an acute angle (31-45°) to the wearing surface. Based on the cracks shown in Figure 6, the failure of the white layer in this study is model 1, which is stress state related and delamination along the cracking path is the main failure mechanism.

4.3. FAILURE MECHANISM

The service component examined was a matched pair of ground Fe-18Cr-3.3C-15Mo-1.65V white iron wear parts. The component was examined and there was no evidence of white layer formation as a result of surface grinding, as shown on the unworn surface in Figure 5(a). Worn surfaces exhibited various stages of adhesive wear beginning with material transfer between components with a characteristic of attachment, as shown in Figure 10(c). It is known that a certain amount of plastic deformation is required to close the interfacial gap between two contact surfaces during the service [65]. Point loading with high contact pressure occurred, as the number and severity of the attachments increase. Surface temperature is also expected to increase. The combination of high contact pressure and increased surface temperature induced plastic flow along the sliding direction as shown in Figure 5. Carbides phases such as M7C3 and M2C are expected to have limited plasticity and fractures were observed along the length of the rod-shaped carbides. This process refined the grains, and at some certain point, nanocrystalline white layer was produced. Similar nanocrystalline white layers have

been reported in AISI 1065 steel, where the authors produced white layer by adhesive sliding wear friction [66].

While most studies state that the white layer has a detrimental influence on wear components, Cho et al. found that the white layer can increase wear resistance in a low contact stress condition. This advantage diminishes, as the white layer delaminated at a higher load [36]. The high contact pressure introduced higher load on the white layer, and eventually delamination of white layer occurred along the cracks within the white layer, as shown in Figure 6. Discontinuity of the white layer on the worn surface may be a result of variation in contact pressure on the worn surfaces, since the engineered point of contact continuously shifts during service.

Delamination of white layers can be expected to produce large loose particles between the two contact surfaces creating a three-body abrasive wear condition. The abrasive cutting scars in the radial direction of sliding are shown in Figure 10(a) and Figure 10(b). Growth of surface delamination produced the micro-galling defects as shown in Figure 10(d). In this case, the plastic deformation generated by contact pressure was not high enough to close the gaps and subsequent oil leakage resulted in failure.

5. CONCLUSION

A wear-resistant, high molybdenum and chromium white iron used for metal-to-metal wear systems was investigated. Microstructural characterization showed that there were four phases in this wear-resistant material including: ferrite, retained austenite,

M7C3 and M2C carbides. Solidification sequence was determined based on the size of the phase constituents and equilibrium calculation results.

Micro-galling defects were found on the wearing surface of the field returned component which lead to loss of lubrication. Examination of the micro-galling defects and microstructure suggests the following sequence. Excessive frictional heat induced severe adhesive wear, which in turn introduced material attachment and white layer formation on the worn surface. The delamination of white layer led to loose particle debris on the contact interface, followed by three-body abrasive wear. Eventually, the complex wear activity produced large areas of defects (micro-galling), and caused oil leakage in the wear systems.

ACKNOWLEDGEMENTS

This work was financially supported by Caterpillar Inc. The authors are grateful for the technical discussion with Christopher A. Barnes, and James O. Barlow. Andrew Hoffman is acknowledged for his assistance with regard to TEM image analysis. Yizhi Du is acknowledged for his help on FIB sample preparation.

REFERENCES

[1] X. Ai, and C. A. Moyer, "Rolling Element Bearings," in *Modern Tribology Handbook*, CRC, 2001, pp. 1041-1093.

[2] H. S. Cheng, "Gears," in *Modern Tribology Handbook*, CRC, 2001, pp. 1095-1129.

[3] R. F. Salant, "Rotary Dynamic Seals," in *Modern Tribology Handbook*, CRC, 2001, pp. 1131-1157.

[4] J. A. Hawk, R. D. Wilson, J. H. Tylczak and O. N. Dogan, "Laboratory Abrasive Wear Tests: Investigation of Test Methods and Alloy Correlation," *Wear,* vol. 225, pp. 1031-1042, 1999.

[5] M. Riddihough, "Stellite as a wear-resistant material," *Tribology,* vol. 3, no. 4, pp. 211-215, 1970.

[6] K. C. Antony, "Wear-Resistant Cobalt-Based Alloys," *Journal of Metals*, vol. 35, no. 2, pp. 52-60, 1983.

[7] J. Shin, J. Doh, J. Yoon, D. Lee, and J. Kim, "Effect of molybdenum on the microstructure and wear resistance of cobalt-base Stellite hardfacing alloys," *Surface and Coatings Technology,* vol. 166, no. 2-3, pp. 117-126, 2003.

[8] H. Berns and W. Theisen, "Tribological Properties," in *Ferrous Materials*, Bochum, Springer, 2008, p. 103.

[9] J. Wan, J. Qing and M. Xu, "Developing a Graphitic White Cast Iron," in *Materials Science and Technology 2018*, Columbus, 2018.

[10] J. Wan, P. W. Habecker, J. Qing and M. Xu, "Evolution of Phases in a Graphitic White Iron," in *AFS*, Atlanta, 2019.

[11] J. Wan, J. Qing, and M. Xu, "Designing a Graphitic White Iron: Microstructures and Properties," in *AISTech*, Pittsburgh, Pa., USA, 2019.

[12] J. Wan, D. C. Van Aken, J. Qing, T. J. Yaniak, T. C. Clements, and M. Xu, "Developing a graphitic white iron for abrasive wear application: Thermal and wear properties," *Wear,* Vols. 436-437, p. 202967, 2019.

[13] J. Wan, J. Qing and M. Xu, "Designing a Novel Graphitic White Iron for Metal-to-metal Wear Systems," *Metallurgical and Materials Transactions A*, vol. 50, no. 3, pp. 1162-1174, 2019.

[14] B. Basu, and M. Kalin, Tribology of Ceramics and Composites: A Materials Science Perspective, John Wiley & Sons, 2011.

[15] J. F. Archard, "THE TEMPERATURE OF RUBBING SURFACES," *Wear,* vol. 2, pp. 438-455, 1958.

[16] A. H. Abdel-Aal, "Flash Temperature Theory," in *Encyclopedia of Tribology*, Boston, Springer, 2013.

[17] G. Sutter, and N. Ranc, "Flash temperature measurement during dry friction process at high sliding speed," *Wear,* vol. 268, no. 11-12, pp. 1237-1242, 2010.

[18] F. E. Kennedy, "Frictional Heating and Contact Temperatures," in *Modern Tribology Book*, CRC, 2001, pp. 235-272.

[19] L. J. Gschwender, D. C. Kramer, B. K. Lok, S. K. Sharma, C. E. Snyder, and M. L. Sztenderowicz, "Liquid Lubricants and Lubrication," in *Modern Tribology handbook*, CRC, 2001, pp. 361-373.

[20] P. C. Okonkwo, G. Kelly, B. F. Rolfe and M. P. Pereira, "The Effect of Temperature on Sliding Wear of Steel-tool Steel Paris," *Wear*, vol. 282, no. 5, pp. 22-30, 2012.

[21] V. L. Ratia, D. Zhang, M. J. Carrington, J. L., Daure, D. G. McCartney, P. H. Shipway and D. A. Stewart, "The Effect of Temperature on Sliding Wear of Self-mated HIPed Stellite 6 in a Simulated PWR Water Invironment," *Wear,* 2018.

[22] W. Molnar, A. Nevosad, H. Rojacz, K. Adam, H. J. Henze, M. R. Ripoll, and E. Badisch, "Two and three-body abrasion resistance of rubbers at elevated temperatures," *Wear,* Vols. 414-415, pp. 174-181, 2018.

[23] H. Rojacz, H. Pahr, S. Baumgartner, and M. Varga, "High temperature abrasion resistance of differently welded structural steels," *Tribology International*, vol. 113, pp. 487-499, 2017.

[24] A. Gaard, N. Hallback, P. Krakhmalev and J. Bergstrom, "Temperature Effects on Adhesive Wear in Dry Sliding Contacts," *Wear,* vol. 268, no. 7, pp. 968-975, 2010.

[25] C. Barnes, *Failure Analysis,* Peoria, IL, 2015.

[26] G. Guerrini, F. Lerra, and A. Fortunato, "The effect of radial infeed on surface integrity in dry generating gear grinding for industrial production of automotive transmission gears," *Journal of Manufacturing Processes*, vol. 45, pp. 234-241, 2019.

[27] A. Alok, and M. Das, "White layer analysis of hard turned AISI 52100 steel with the fresh tip of newly developed HSN2 coated insert," *Journal of Manufacturing Processes,* vol. 46, pp. 16-25, 2019.

[28] R. D. Gruiter, "WHITE LAYER IN HARD TURNING," 2015.

[29] D. Kurten, I. Khader, R. Raga, P. Casajus, N. Winzer, A. Kailer, R. Spallek, and M. Scherge, "Hydrogen assisted rolling contact fatigue due to lubricant degradation and formation of white etching areas," *Engineering Failure Analysis,* vol. 99, pp. 330-342, 2019.

[30] L. Xin, M. Ma, Y. Lu, and T. Shoi, "Comparative study on fretting wear behaviors of Alloy 600MA in dry air and deionized water conditions," *Wear,* Vols. 418-419, pp. 167-179, 2019.

[31] P. Palit, S. Das, and J. Mathur, "Metallurgical investigation of wire breakage of tyre bead grade," *Case Studies in Engineering Failure Analysis,* vol. 4, pp. 83-87, 2015.

[32] S. S. Bosheh, and P. T. Mativenga, "White layer formation in hard turning of H13 tool steel at high cutting speeds using CBN tooling," *International Journal of Machine Tools & Manufacture,* vol. 46, pp. 225-233, 2006.

[33] F. Klocke, E. Brinksmeier, and K. Weinert, "Capability profile of hard cutting and grinding processes," *Annals of CIRP,* vol. 54, no. 2, pp. 22-45, 2005.

[34] S. Smith, S.N. Melkote, L. Curzio, E.T. Watkins, R. Allard, and L. Riester, "Effect of surface integrity of hard turned AISI 52100 steel on fatigue performance," *Materials Science & Engineering A,* vol. 459, pp. 337-346, 2007.

[35] Y.B. Guo, and G.M. Janowski, "Microstructural characterization of white layers by hard turning and grinding," *Transactions of NAMRI/SME,* vol. 32, pp. 367-374, 2004.

[36] D. Cho, S. Lee, and Y. Lee, "Mechanical Properties and Wear Behavior of the White Layer," *Tribology Letter,* vol. 45, pp. 123-129, 2012.

[37] E. Abbasi, Q. Luo, and D. Owens, "Case study: Wear mechanisms of NiCrVMo-steel and CrB-steel scrap shear blades," *Wear,* Vols. 398-399, pp. 29-40, 2018.

[38] K. D. Vo, A. K. Tieu, H. T. Zhu, and P. B. Kosasih, "The influence ofhightemperatureduetohighadhesioncondition on rail damage," *Wear,* Vols. 330-331, pp. 571-580, 2015.

[39] S. S. Bosheh, and P. T. Mativenga, "White layer formation in hard turning of H13 tool steel at high cutting speeds using CBN tooling," *International Journal of Machine Tools & Manufacture,* vol. 46, pp. 225-233, 2006.

[40] S. Han, S. N. Melkote, M. S. Haluska, and T. R. Watkins, "White layer formation due to phase transformation in orthogonal machining of AISI 1045 annealed steel," *Materials Science and Engineering A,* vol. 488, pp. 195-204, 2008.

[41] A. Attanasio, D. Umbrello, C. Cappellini, G. Rotella, and R. M'Saoubo, "Tool wear effects on white and dark layer formation in hard turning of AISI 52100 steel," *Wear,* Vols. 286-287, pp. 98-107, 2012.

[42] S. B. Hosseini, T. Beno, U. Klement, J. Kaminski, and K. Ryttberg, "Cutting temperatures during hard turning—Measurements and effectson white layer formation in AISI 52100," *Journal of Materials Processing Technology,* vol. 214, pp. 1293-1300, 2014.

[43] S. B. Hosseini, M. Thuvander, U. Klement, G. Sundell, and K. Ryttberg, "Atomic-scale investigation of carbon atom migration in surface induced white layers in high-carbon medium chromium (AISI 52100) bearing steel," *Acta Materialia,* vol. 130, pp. 155-163, 2017.

[44] R. Hossain, F. Pahlevani, E. Witteveen, A. Banerjee, B. Joe, B. G. Pursty, R. Deppenaar, and V. Sahajwalla, "Hybrid structure of white layer in high carbon steel – Formation mechanism and its properties," *Scientific Report,* vol. 7, no. 13288, pp. 1-12, 2017.

[45] F. Zhang, C. Duan, M. Wang, and W. Sun, "White and dark layer formation mechanism in hard cutting of AISI52100 steel," *Journal of Manufacturing Processes* , vol. 32, pp. 878-887, 2018.

[46] Annual Book of ASTM Standards, "ASTM Designation E407-07," *ASTM*, 2007.

[47] C. A. Johnson, Metallography Principles and Procedures, St. Joseph: LECO Corporation, 1996.

[48] S. Liu, Y. Zhou, X. Xing, J. Wang, X. Ren, and Q. Yang, "Growth characteristics of primary M7C3 carbide in hypereutectic Fe-Cr-C alloy," *Scientific Report,* vol. 6, pp. 32941-32946, 2016.

[49] R. van Bremen,D.Ribas Gomes,L.T.H.de Jeer,V.Ocelík, and J.Th.M.DeHosson, "On theoptimumresolutionoftransmission-electronbackscattered diffraction (t-EBSD)," *Ultramicroscopy,* vol. 160, pp. 256-264, 2016.

[50] P. W. Trimby, "Orientation mapping of nanostructured materials using transmission Kikuchi diffraction in the scanning electron microscope," *Ultramicroscopy,* vol. 120, pp. 16-24, 2012.

[51] J. W. Stead, "Micro-metallography and its practical applications," *Journal of Western Scottish Iron and Steel Institute,* vol. 19, pp. 169-204, 1912.

[52] J. Wan, D. C. Van Aken, J. Qing, and M. Xu, "Adhesive Wear Property of a Graphitic White Iron Designed for Metal-to-Metal Wear Systems," 2019.

[53] H. Wada, "Thermodynamic Properties of Carbides in 2.25Cr-1Mo Steel at 985 K," *Metallurgical Transaction A,* vol. 17A, pp. 1585-1592, 1986.

[54] Z. Xu, L. Jiang, J. Dong, Z. Li, and X. Zhou, "The effect of silicon on precipitation and decomposition behaviors of M6C carbide in a Ni–Mo–Cr superalloy," *Journal of Alloys and Compounds,* vol. 620, pp. 197-203, 2015.

[55] L. Jiang, W. Zhang, Z. Xu, H. Huang, X. Ye, B. Leng, L. Yan, Z. Li, and X. Zhou, "M2C andM6C carbide precipitation in Ni-Mo-Cr based superalloys containing silicon," *Materials and Design,* vol. 112, pp. 300-308, 2016.

[56] S. B. Hosseini, U. Klement, Y. Yao, and K. Ryttberg, "Formation mechanisms of white layers induced by hard turning of AISI 52100 steel," *Acta Materialia,* vol. 89, pp. 258-267, 2015.

[57] X. Wu, P. Jiang, L. Chen, F. Yuan, and Y. T. Zhu, "Extraordinary strain hardening by gradient structure," *PNAS,* vol. 111, no. 20, pp. 7197-7201, 2014.

[58] X. L. Wu, P. Jiang, L. Chen, J. F. Zhang, F. P. Yuan & Y. T. Zhu, "Synergetic Strengthening by Gradient Structure," *Materials Research Letters,* vol. 2, no. 4, pp. 185-191, 2014.

[59] A.M. WUSATOWSKA-SARNEK, B. DUBIEL, A. CZYRSKA-FILEMONOWICZ, P.R. BHOWAL, N. BEN SALAH, and J.E. KLEMBERG-SAPIEHA, "Microstructural Characterization of the White Etching Layer in Nickel-Based Superalloy," *METALLURGICAL AND MATERIALS TRANSACTIONS A*, vol. 42A, pp. 3813-3825, 2011.

[60] Z. Fan, B. Joni, G. Ribarik, E. Odor, Z. Fogarassy, and T. Ungar, "The Microstructure and strength of a V–5Cr–5Ti alloy processed by high pressure torsion," *Materials Science and Engineering: A*, vol. 758, pp. 139-146, 2019.

[61] Z. Wang, J. Han, J. P. Domblesky, Z. Li, and X. Fan, "Crack propagation and microstructural transformation on the friction surface of a high-speed railway brake disc," *Wear*, Vols. 428-429, pp. 45-54, 2019.

[62] A. Kagawa, T. Okamoto, K. Saito, and M. Ohta, "Hot hardness of (Fe,Cr)3C and (Fe,Cr)7C3 carbides," *JOURNAL OF MATERIALS SCIENCE*, vol. 19, pp. 2546-2554, 1984.

[63] J. Wang, W. Guo, H. Sun, H. Li, H. Gou, and J. Zhang, "Plastic deformation behaviors and hardening mechanism of M7C3 carbide," *Materials Science and Engineering: A*, vol. 662, pp. 88-94, 2016.

[64] Y. Yang, H. Fang, Y. Zheng, Z. Yang, and Z. Jiang, "The failure models induced by white layers during impact wear," *Wear*, vol. 185, no. 1-2, pp. 17-22, 1995.

[65] B. N. J. Persson, "Leakage of Metallic Seals: Role of Plastic Deformations," *Tribology Letter*, vol. 63, pp. 1-6, 2016.

[66] K. Sipos, M. Lopez, and M. Trucco, "Surface Martensite White Layer Produced by Adhesive Sliding Wear-Friction in AISI 1065 Steel," *Revista Latinoamericana de Metalurgia Materiales*, vol. 28, no. 1, pp. 46-50, 2008.

II. DESIGNING A NOVEL GRAPHITIC WHITE IRON FOR METAL-TO-METAL WEAR SYSTEMS

Jie Wan[1], Jingjing Qing[2], Mingzhi Xu[2]

[1]Missouri University of Science and Technology, Rolla, MO 65401, USA

[2]Georgia Southern University, Statesboro, GA 30460, USA

Tel: 573-578-3874

Email: jwvt7@mst.edu

Keywords: Graphitic White Iron, Alloy Design, Wear Resistant, Carbon Equivalent, Characterization

ABSTRACT

Metal-to-metal wear systems are widely used in various industries, but heat induced adhesive wear has been limiting the lifetime of the components for many years. An idea of introducing interconnected flake graphite networks into white iron was developed by the authors, which can potentially solve this problem by increasing the overall thermal conductivity. To optimize the thermal conductivity and wear resistance, five alloys with different chromium and carbon contents were designed, produced and investigated to develop the first generation of graphitic white iron. Mathematical models were developed to correlate the graphite phase concentration and cooling rate with carbon equivalent. It was shown that graphite volume percent needs to be higher than 7% to have a consistent thermal conductivity increase. Hardness model developed in this article suggested that M7C3 has a higher hardness than the plate cementite, and hardness

increases with increasing chromium content in the carbides. The as-solidified microstructure was characterized using a SEM, and solidification sequence was established for this novel alloy system. Unexpectedly, for the first time, study of alloy with 11 wt.% Cr shows that M7C3 was formed during eutectic reaction and then transformed into cementite at a lower temperature.

1. INTRODUCTION

White cast iron exhibits a white, crystalline fracture surface because the fracture occurs along the iron carbide plate [1], which is a result of no graphitization and fast cooling rate. Due to the relatively high hardness of cementite carbide (800-1100HV) [2], white cast iron is extensively used in wear resistance applications. However, it is difficult to obtain sufficient cooling rate to produce white cast iron in heavy sections or relatively large castings, thus high alloy additions are added to promote carbide formation at a slower solidification cooling rate. Typically, high-alloyed white cast irons fall into two major groups [3]: Ni-Cr white iron and Cr-Mo white iron. Among all grades of white cast irons, high Cr white iron is the most popular type due to its higher hardness resulted from M7C3 carbides (1100-1600HV) [2]. Numerous studies have been conducted on the effects of alloy additions on high Cr white cast iron. Additional vanadium is added for grain refinement purpose [4-5]. Silicon is also added for grain refinement and it also increases the volume fraction of the eutectic carbides [6]. Titanium is used to refine primary M7C3 carbides [7-11]. In addition, niobium was found to be effective to improve

the fracture strength by changing the morphology of eutectic carbides from plate/rod-like shape to isotropic shape [12].

Gray cast iron exhibits a gray fracture surface because the fracture occurs along graphite flakes [1], which can be formed as primary graphite or eutectic graphite. Generally, flake graphite in gray iron is divided into five type based on their distributions, morphologies and patterns [13-14]. In specific, type A graphite flakes have a random orientation and are intended in gray iron, type B graphite has a rosette pattern, type C graphite is kish graphite which is formed in hypereutectic cast irons, type D graphite is randomly orientated very fine interdendritic flakes, and type E graphite is very fine interdendritic flakes with a preferred orientation [14]. Due to interconnected structure of graphite, gray iron always presents higher thermal conductivity as compared to the with other graphitic irons [15-16], which also can be concluded from the cooling curves for different cast irons [17-19].

High Cr white cast iron is commonly used in metal-to-metal wear applications, where significant heat induced by friction causes severe adhesive wear [20-21]. To take the advantage of both high wear resistance from carbide and high thermal conductivity from interconnected graphite, the authors proposed to design a mottled graphitic white iron. Typically, mottled cast iron refers to mottled nodular cast iron [22-27] and are generally used for mill rolls [22-24]. But limited work has been done on designing mottled cast iron containing flake graphite.

In the present work, the authors introduced interconnected graphite networks into the as-solidified matrix to increase the thermal conductivity of white iron. Specifically, five mottled cast iron alloys were designed and produced in an induction furnace. The

five alloys were studied metallographically to determine the graphite and carbide phase fraction. Solidification sequences were studied by rationalizing the thermodynamic equilibrium calculation results with optical microstructures. Meanwhile, Energy Dispersive Spectroscopy (EDS) and Electron Backscatter Diffraction (EBSD) were used to further verify the solidification sequences. Hardness of different carbides in all five alloys were measured. Numerical models were constructed for guiding future alloy design.

2. MATERIAL AND METHODS

2.1. RATIONAL FOR CHEMISTRY

In the present investigation, a series of 2wt.%Si-0.5wt.%Mn-C-Cr-Fe alloys were designed and studied. Based on thermodynamic calculation using software FactSage Equilibrium Modulus (version 7.1, database FSstel), the primary phase formed during solidification over 0-30wt.% Cr and 0-8wt.% C was plotted in Figure 1. It is shown that carbon promotes the formation of graphite, while chromium promotes the formation of M7C3 and ferrite. It is well known that an interconnected graphite network in metal can provide high thermal conductivity, for example, the type A flake graphite in grey cast iron. Carbides are known for a relatively high hardness, which increases a casting's wear resistance. To take the advantage of both graphite and carbides, three hypereutectic and two hypoeutectic chemistries were proposed. The alloys were named with their individual Cr content and marked as different colored dots in Figure 1. Here Cr is

working as a regulator to control the competition of carbon between graphite and carbides.

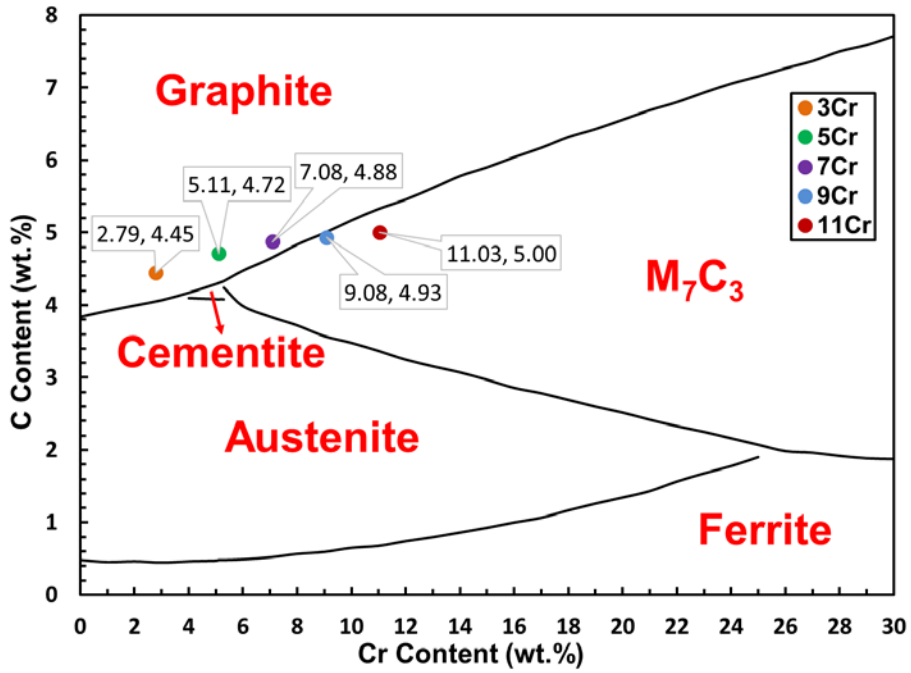

Figure 1. The primary phase formed during solidification at different contents of C and Cr; Colored dots represent the alloys studied in this research; numbers in each callout represent the chemistry of C and Cr individually.

To accurately control the chemistry, high purity charge materials including induction iron, Desulco graphite, low carbon ferrochrome, ferrosilicon and ferromanganese were melt in an induction furnace to produce five alloys with various Cr and C contents. Metal was cast into no-bake sand molds with 200ºC superheat for each alloy. The chemical composition of the five produced alloys is given in Table 1. Additionally, 0.15wt.% graphite inoculant was added into the sprue well prior to each pour to promote graphite formation. The pertinent temperature information is shown in Table 2.

Table 1. Composition analyzed using spark emission spectrometer and Leco C/S analyzer.

Alloys	Chemical composition (wt.%)					Inoculant (wt.%)
	Leco C	Leco S (ppm)	Si	Mn	Cr	
3Cr	4.45	154	2.06	0.44	2.79	0.15
5Cr	4.72	157	2.00	0.47	5.11	0.15
7Cr	4.88	184	2.07	0.49	7.08	0.15
9Cr	4.93	198	2.05	0.50	9.08	0.15
11Cr	5.00	170	2.03	0.50	11.03	0.15

Table 2. Pertinent temperature information for all studied alloys.

Alloys	Temperature (ºC)			
	A_1	Solidus	Liquidus	Pouring Temperature
3Cr	798	1142	1305	1505
5Cr	818	1139	1304	1504
7Cr	834	1134	1292	1492
9Cr	834	1138	1256	1456
11Cr	834	1138	1282	1482

2.2. SAMPLE PREPARATION AND CHARACTERIZATION

All specimens were sectioned from the bottom part of the casting to minimize the amount of shrinkage porosity. Metallography samples were machined from the same location to minimize the variation due to different cooling rates. Two sets of samples were ground on silicon carbide papers to 1200 grits and then polished using 3 µm followed by 0.1 µm diamond paste. The first set of as-polished samples were used to study the graphite fraction, and the second set of samples were etched with 2% nital to measure carbide fraction as well as micro-hardness. Microstructure was analyzed using a Nikon FX-35DX camera. Microhardness was conducted with Duramin-5 microhardness tester. ASPEX-EDS was used to determine the composition of each carbide phase. EBSD was performed on alloy 11Cr to discriminate different types of carbides in it. FactSage

7.1 (FSstel database) was used to calculate the phase diagrams and phase equilibrium step diagrams to study the solidification sequences.

3. METALLOGRAPHY RESULTS

As polished microstructure is shown in Figure 2 to reveal different graphite morphology and fraction among five alloys. Type A (green arrows in Figure 2) and type C (red arrows in Figure 2) graphite are observed in alloy 3Cr, 5Cr and 7Cr. Type D graphite (purple arrows in Figure 2) is found within the dendritic structures for all five alloys.

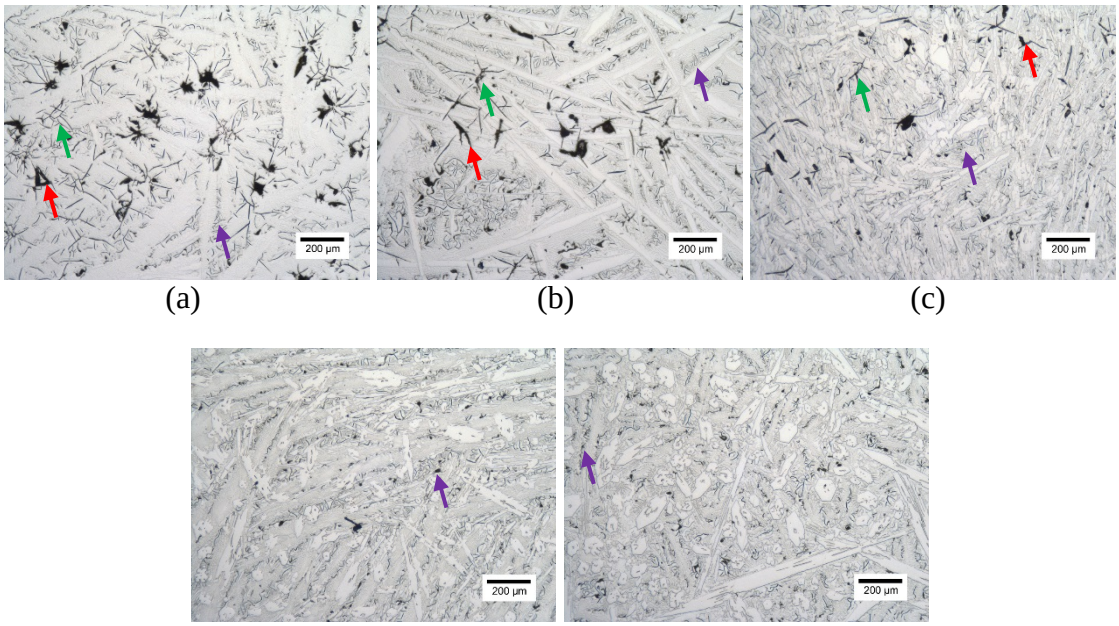

Figure 2. Graphite morphology in as-polished microstructure: (a) 3Cr; (b) 5Cr; (c) 7Cr; (d) 9Cr; (e) 11Cr.

Another set of specimens were etched with 2% nital to reveal various phases. Figure 3 shows the microstructures under a lower magnification. Few skinny plate carbides are observed in alloys 3Cr. Longer and thicker plate carbides are found in alloy 5Cr. In alloy 7Cr, besides plate carbide, cluster carbides are noticed. As the Cr content increases, in alloys 9Cr, more hexagonal shaped carbides and fewer plate carbides are observed. However, in alloy 11Cr, a lot of hexagonal shaped carbides but minimum plate carbide was observed. In Figure 3, the plate carbides are indicated by red arrows, cluster carbides are indicated by purple arrows, and hexagonal shaped carbides are indicated by green arrows, respectively. Furthermore, pearlite was differentiated in all five alloys under a higher magnification shown in Figure 4 and there was no obvious difference in pearlite morphology among all five alloys.

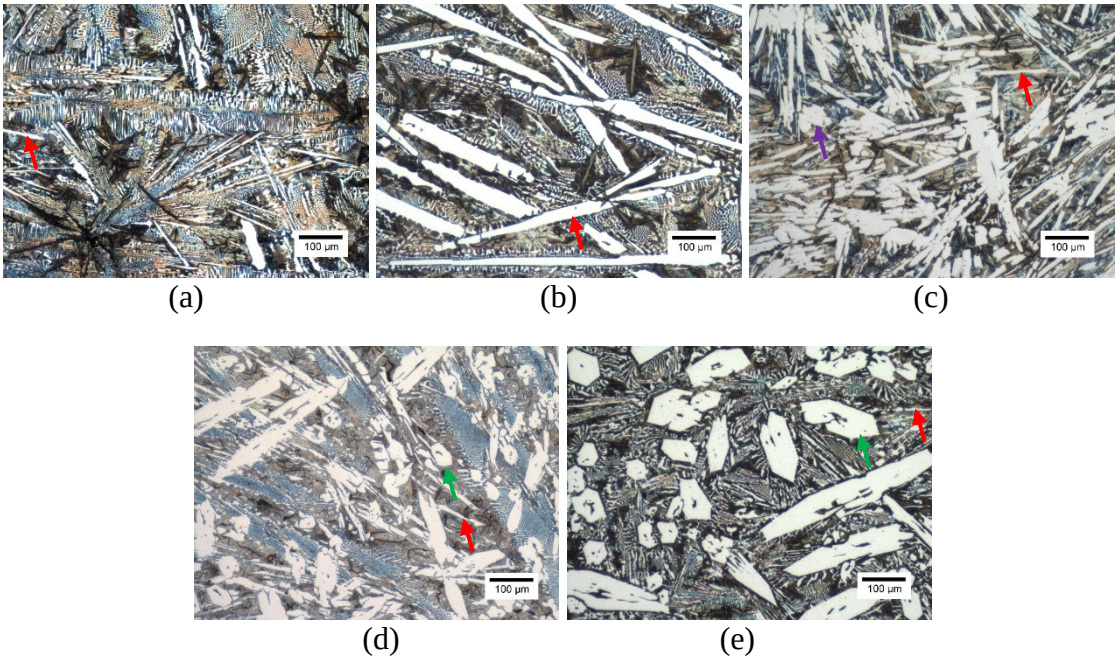

(a) (b) (c)

(d) (e)

Figure 3. Carbide morphology in 2% nital etched microstructure at a lower magnification: (a) 3Cr; (b) 5Cr; (c) 7Cr; (d) 9Cr; (e) 11Cr.

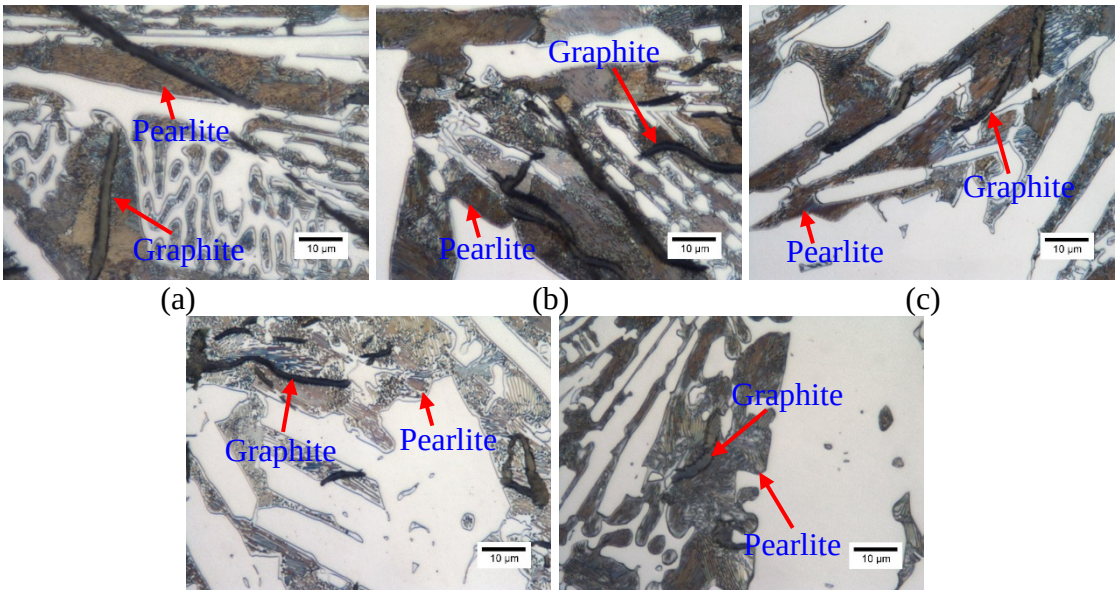

Figure 4. Pearlite structure revealed by 2% nital etched microstructure at a higher magnification: (a) 3Cr; (b) 5Cr; (c) 7Cr; (d) 9Cr; (e) 11Cr.

4. DISCUSSION

4.1. GRAPHITE PHASE FRACTION VS CARBON EQUIVALENT

FactSage 7.1 (database FSstel) was used to calculate the amount of graphite and carbide during solidification in all studied alloys. The weight percent of both graphite and carbides were calculated at a temperature right above the critical temperature A1 during the equilibrium solidification. No eutectoid reaction takes place at such temperature, consequently no eutectoid product was considered in the calculation. In another word, only primary carbide and those carbides formed during metastable eutectic reaction in ledeburite were included. Then weight percent for each phases were transformed into volume percent using following densities: ρ(graphite)=2266 kg/m3, ρ(Fe3C)=7730 kg/m3, ρ(M7C3)=7230 kg/m3 and ρ(austenite)=7915 kg/m3.

ImageJ software was used to measure the amount of graphite and carbide on optical micrographs for all five alloys. Graphite was measured from the as polished microstructures shown in Figure 2. The contrast threshold was adjusted to include both primary graphite and eutectic graphite. Carbides were measured using the 2% nital etched microstructures shown in Figure 3. Similarly, the contrast threshold was carefully adjusted such that only primary carbides and eutectic carbides were highlighted. Carbides in pearlite formed during the eutectoid reaction were not included in the ImageJ measurements. As a consequence, neither FactSage calculation nor ImageJ measurements considered the eutectoid reaction products. Figure 5 shows an example of an adjusted threshold for both graphite and carbides.

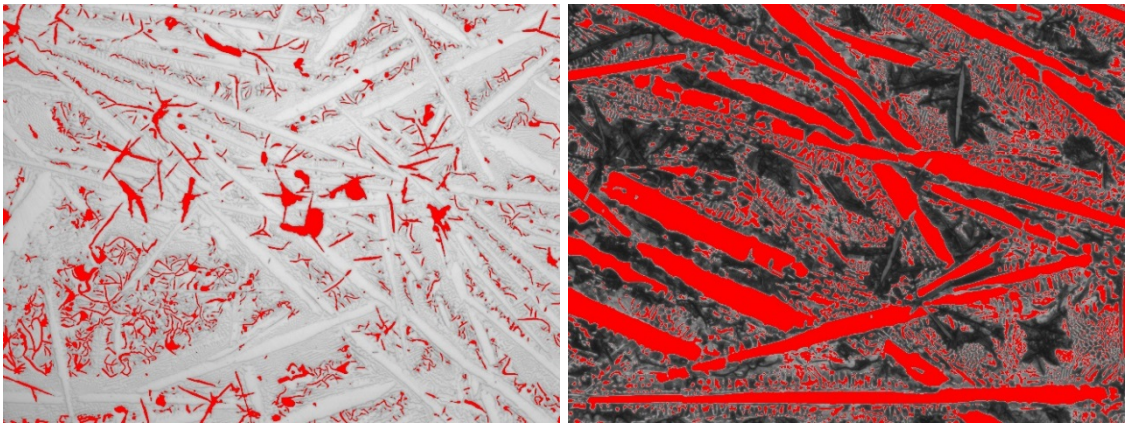

(a) (b)

Figure 5. Contrast threshold was adjusted in ImageJ to include (a) graphite and (b) primary and eutectic carbides; scale bars were removed to avoid interference with the threshold.

As shown in Figure 6, the volume percent of graphite and carbides calculated using FactSage was compared with that measured with ImageJ. Red bars represent FactSage equilibrium calculation results at a temperature above critical temperature A1.

Blue bars represent ImageJ measurements averaged from ten micrographs. The error bars represent 95% CL uncertainty range [28].

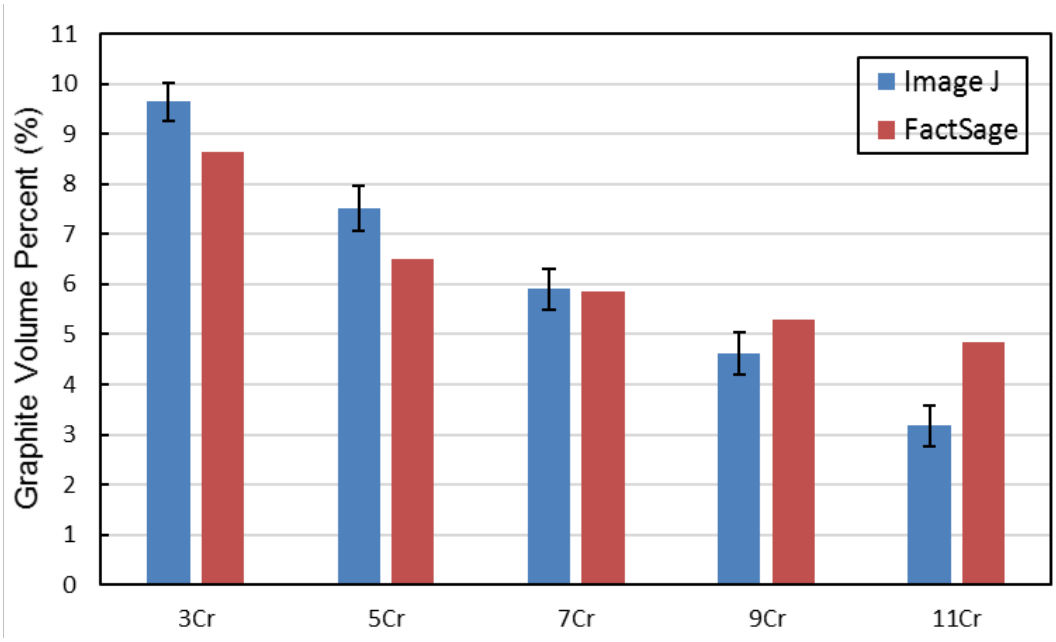

(a)

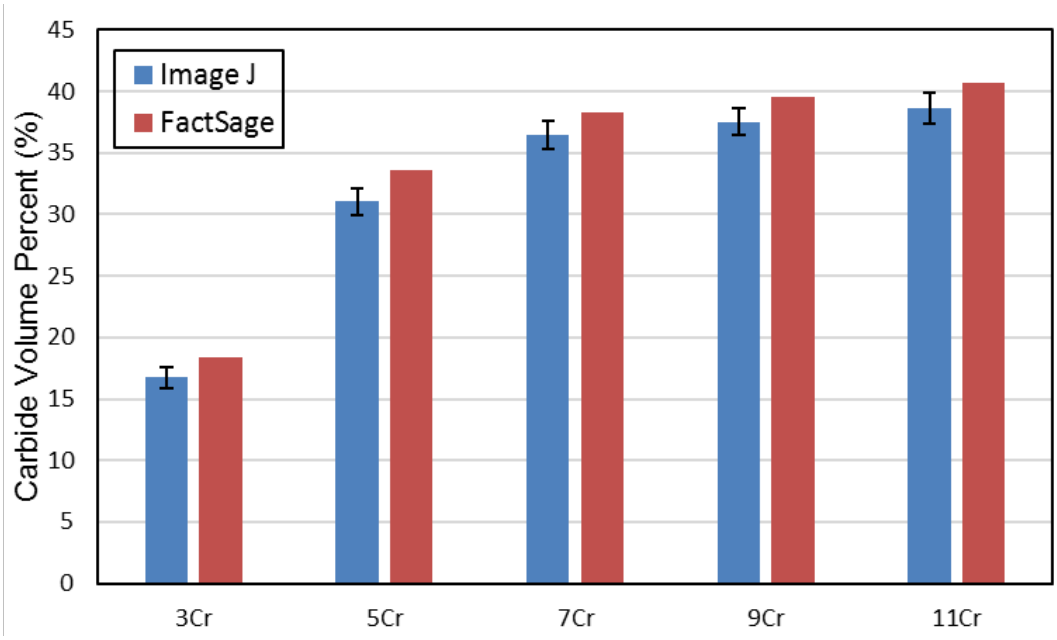

(b)

Figure 6. Phase percent comparison among five alloys for: (a) Graphite; (b) Carbide.

Overall, volume fractions measured by ImageJ is similar to those calculated by FactSage. Following conclusion can be drawn: graphite percent decreases and carbide percent increases with increasing Cr content. Nevertheless, as the Cr content increases, graphite concentration predicted by FactSage at A1 temperature decreases at a slower speed compared to ImageJ measurements. One possible explanation is that at higher Cr levels, FactSage equilibrium module doesn't have a graphite growth model via diffusion built in. It is worth noting that the measured carbide volume percent for all five studied alloys is smaller than the calculated values, which is consistent with Hecht's work [29].

According to previous published works [30-31], following multiplying factors were reported for carbon equivalent calculation: G_C^S = 0.4, G_C^{Si} = 0.33, G_C^{Mn} = -0.027, G_C^{Cr} = -0.25, so Eq. (1) is established to calculate carbon equivalent in these studied alloys.

$$C_{Eq} = C_C + 0.4C_S + 0.33C_{Si} - 0.027C_{Mn} - 0.25C_{Cr} \quad (1)$$

To fully understand how the graphite volume percent is affected by the carbon equivalent, Eq. (1) was used to calculate the carbon equivalents for all five alloys. Then the relation between carbon equivalent and graphite volume percent for those alloys was plotted in Figure 7. It turned out that graphite volume percent increases with increasing carbon equivalent by a linear relation following Eq. (2). And the coefficient of determination is 0.9696, which indicates that Eq. (2) is fitting very well and can be used for future works.

$$V_p(Gr) = 4.1046C_{Eq} - 9.0513 \quad (2)$$

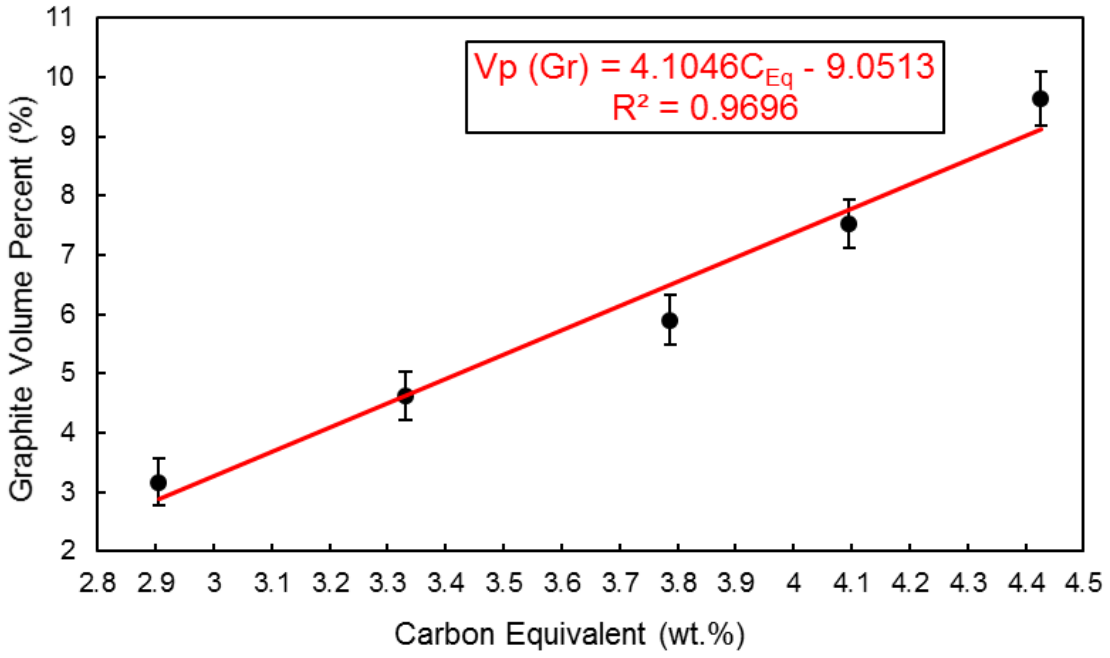

Figure 7. Relation between carbon equivalent and graphite percent.

Cooling curves can be used to predict the graphite morphology and cast structure by studying the cooling characteristics and critical points [19]. One way to qualitatively study the effect of graphite on thermal conductivity is to compare the cooling rate among different alloys during solidification. Figure 8 correlated the cooling rate at 900°C with graphite volume percent for all five alloys. Figure 8(a) shows the cooling curves obtained from thermal analysis cups and Figure 8(b) shows the relation between graphite volume percent and cooling rate at 900°C measured from cooling curves in Figure 8(a). A linear relation between cooling rate at 900°C and graphite volume percent is established and shown in Eq. (3) for all five studied alloys. As is shown in Figure 8(b), as the graphite volume percent increases, cooling rate at 900ºC also increases, which proved that introducing graphite into white iron increases its thermal conductivity. However, cooling rates at 900ºC for alloy 3Cr and alloy 5Cr are much higher than the rest three studied

alloys and once the graphite volume percent is lower than 7%, which is the minimum measured graphite volume percent for alloy 5Cr, the corresponding cooling rate at 900ºC is scattered around 1.1ºC/s. One can conclude that graphite volume percent needs to be higher than 7% in order to increase the thermal conductivity consistently in a graphitic white iron alloy.

$$V_p(Gr) = 2.8358R + 1.6419 \quad (3)$$

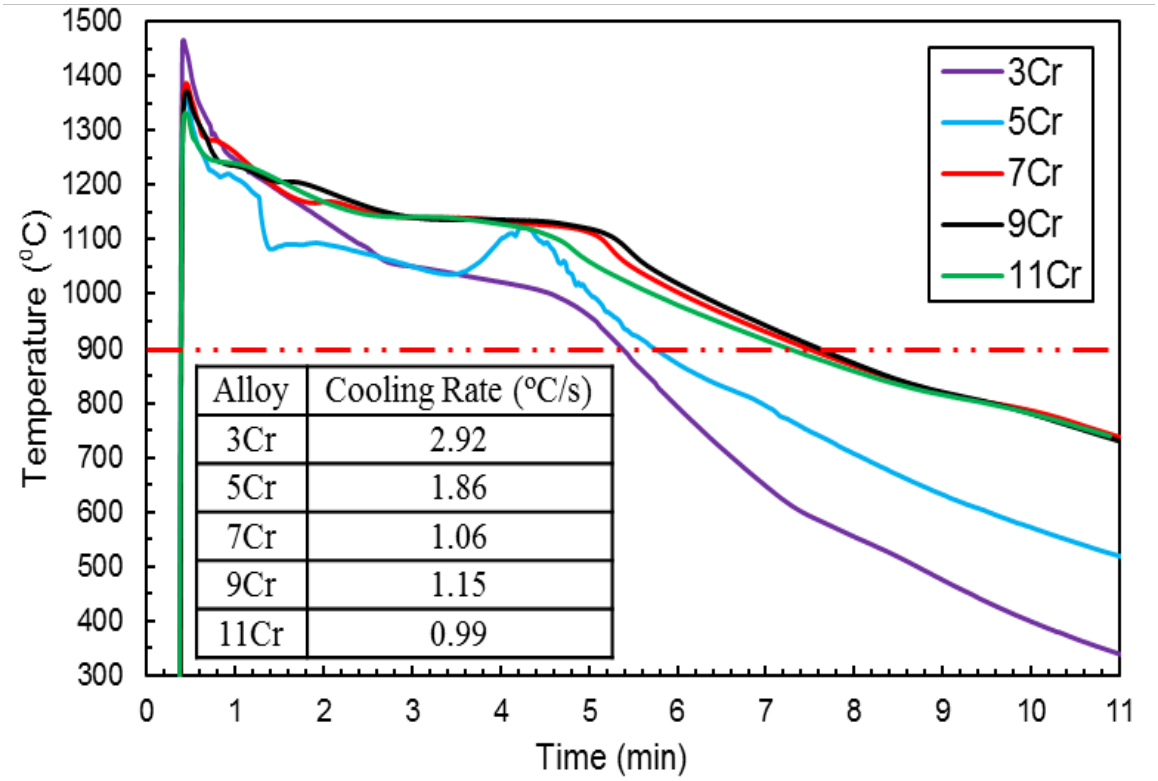

(a)

Figure 8. Cooling rate study for: (a) Cooling curves obtained from ATAS quick cups; (b) Relation between graphite volume percent and cooling rate measured from temperature curves at 900°C.

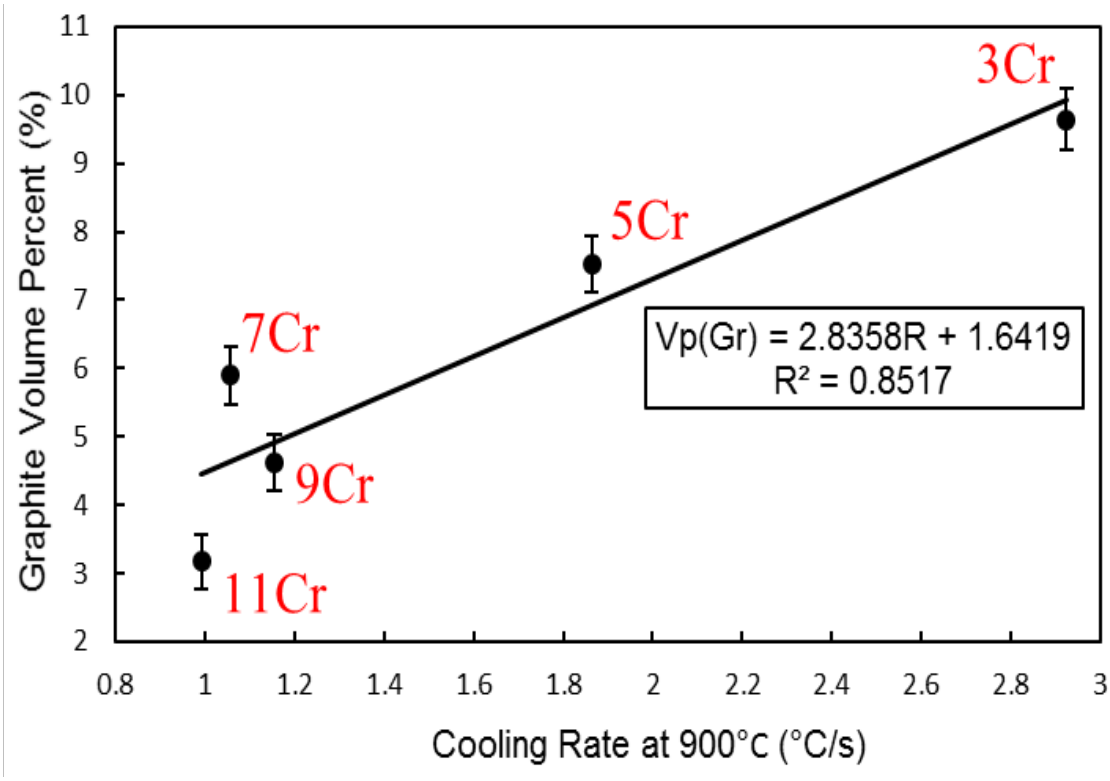

(b)

Figure 8. Cooling rate study for: (a) Cooling curves obtained from ATAS quick cups; (b) Relation between graphite volume percent and cooling rate measured from temperature curves at 900°C (cont.).

4.2. CHARACTERIZATION OF CARBIDES

Plate carbides found in alloy 3Cr and 5Cr were cementite, which is proved by FactSage thermodynamic calculation in Sections 4.3.1 and 4.3.2. However, different morphologies of carbides were observed in alloys with higher Cr contents. Initial FactSage calculation indicated those carbides are cementite and M_7C_3 carbides. Solidification equilibrium was calculated for alloy 7Cr, 9Cr and 11 Cr, and the different ratios of Fe/Cr(wt.%) between cementite and M_7C_3 can be used to differentiate the types of carbide under an electron microscope with an EDS detector. Figure 9 shows some of the examples of EDS measured carbide morphologies. Table 3 summarizes the

calculated and measured Fe/Cr(wt.%) ratios within cementite and M_7C_3 carbides across all samples. It is noticed that the Cr concentration in both cementite and M_7C_3 carbides increases with increasing Cr content in the alloy. By comparing the EDS measured results with the equilibrium calculation, it can be concluded that the plate carbides are primary cementite and hexagonal shaped carbides are M_7C_3 carbides. It is worth noting that the difference on the exact chemistry between EDS and thermodynamic calculation is a result of electron reaction volume in the SEM.

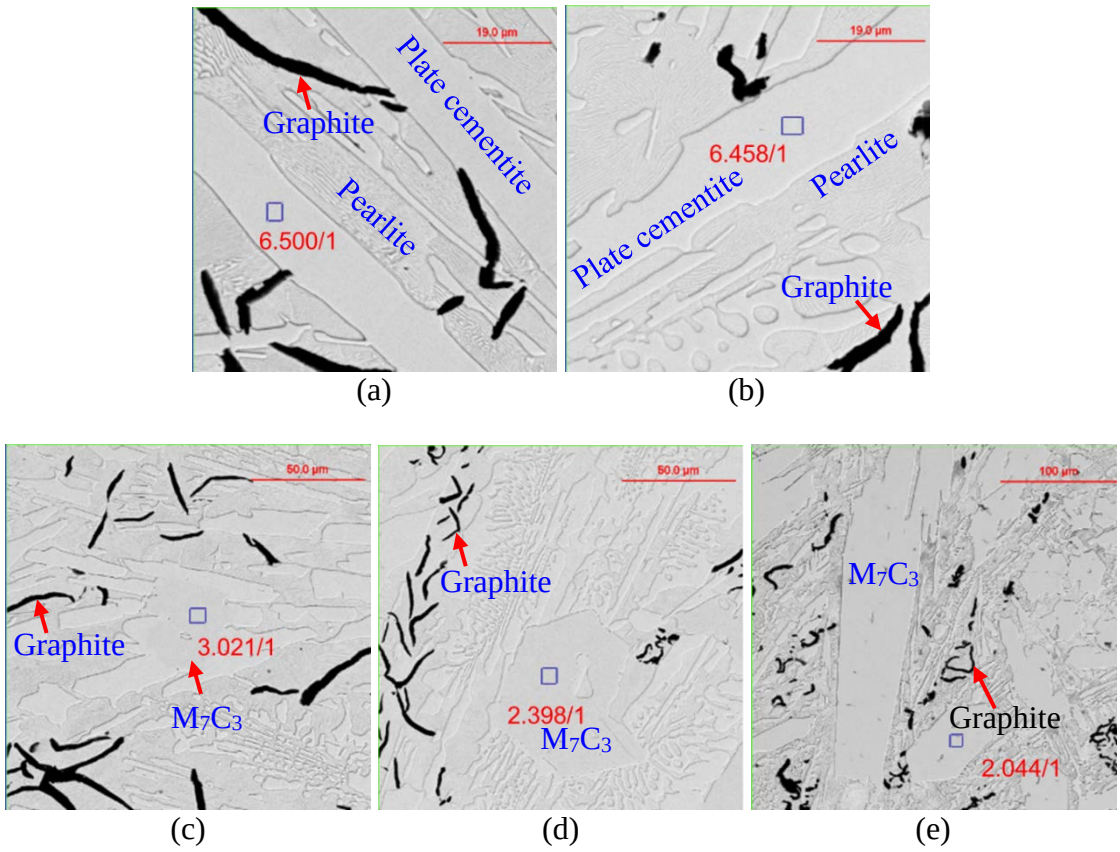

Figure 9. Fe/Cr(wt.%) ratio of : (a) Plate carbide in 7Cr; (b) Plate carbide in 9Cr; (c) Cluster carbide in 7Cr; (d) Hexagonal shaped carbide in 9Cr; (e) Hexagonal shaped carbide in 11Cr.

Table 3. Comparison of Fe/Cr(wt.%) ratio between FactSage calculation and ASPEX-EDS measurement for Fe3C and M7C3.

Fe/Cr (wt.%)		3Cr	5Cr	7Cr	9Cr	11Cr
Fe_3C	FactSage	7.418/1	6.186/1	5.521/1	5.521/1	5.571/1
	EDS	12.690/1	6.722/1	6.500/1	6.458/1	-
M_7C_3	FactSage	-	-	1.528/1	1.528/1	1.528/1
	EDS	-	-	3.021/1	2.398/1	2.044/1

Previous work by Xing et al. suggested that M_7C_3 has a hollow hexagonal structure at high chrome ratio [32]. As shown in Figure 10, higher magnification images show that the cores of the hexagonal M_7C_3 carbide were pearlite, which was austenite before eutectoid reaction. Similar to M_7C_3 carbides in 7Cr and 9Cr. Sha Liu's work claimed that primary M_7C_3 is irregular polygonal shape with several hollows in the center and gaps on the edge [33]. However, Figure 9(e) and Figure 10(c) show that with increasing Cr content in the alloy, the primary M_7C_3 carbide becomes more regular and close to hexagonal in the shape and there is no gaps around the edge of M_7C_3 carbide in alloy 11Cr.

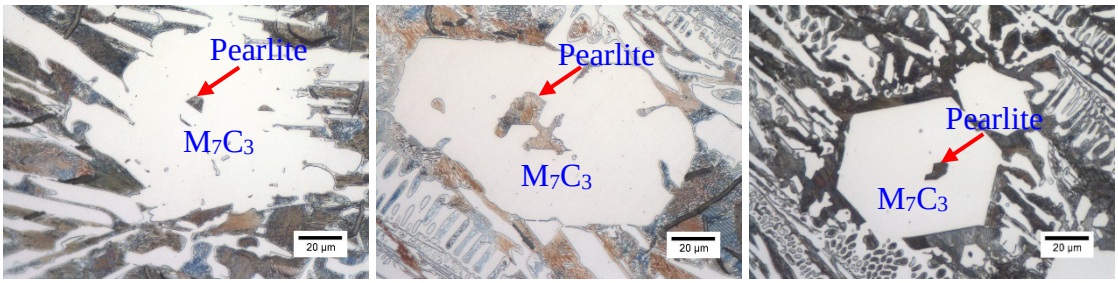

(a) (b) (c)

Figure 10. Pearlite in the center of M_7C_3: (a) 7Cr; (b) 9Cr; (c) 11Cr.

4.3. SOLIDIFICATION SEQUENCE

4.3.1. Alloy 3Cr. By relating the FactSage Equilibrium step diagram, as shown in Figure 11(a), to the microstructure, one can construct the solidification sequence. Specifically, during the solidification, graphite was the primary phase thus type A and type C graphite were observed. As the temperature decreases, the solidification reached the stable eutectic reaction, where austenite and type D graphite were formed. As the solidification continues, cementite (Fe_3C) was precipitated as the primary phase for the metastable reaction, followed by the metastable eutectic reaction. In the metastable eutectic reaction, ledeburite was formed which contains cementite and austenite. When the temperature reached A_1, the austenite transformed to pearlite, as shown in Figure 4(a).

4.3.2. Alloy 5Cr. Similarly to alloys 3Cr, during the solidification of alloy 5Cr, graphite precipitates firstly, as shown in Figure 11(b). As a result, type A and type C graphite were observed. As the solidification continues, primary cementite was formed as the primary phase for the metastable reaction. With decreasing temperatures, the solidification reached stable eutectic reaction where liquid transformed to austenite, type D graphite. Then ledeburite was formed which contains cementite and austenite during the metastable eutectic reaction. Finally when the temperature reached A_1, pearlite structure was formed from the austenite, as shown in Figure 4(b).

4.3.3. Alloy 7Cr. As shown in Figure 11(c), during the solidification of alloy 7Cr, graphite was still the primary phase. Type A and type C graphite were expected. Then M_7C_3 precipitated into cluster carbide instead of cementite as a result of high Cr content compared with alloy 5Cr. After that, primary cementite solidified as the primary phase for the metastable reaction. Austenite and type D graphite were formed as

metastable eutectic products after the solidification of primary cementite. Subsequently, ledeburite was formed during the metastable eutectic reaction. At last, as shown in Figure 4(c), eutectoid reaction occurred and austenite transformed into pearlite at temperature below A_1.

4.3.4. Alloy 9Cr. With regarding to alloy 9Cr, M_7C_3 precipitated first from the liquid metal. As the temperature decreases, primary austenite solidified as the primary phase for the hypo-eutectic reaction. At a lower temperature, primary cementite formed as the primary phase for the metastable hyper-eutectic reaction. Then, the stable eutectic reaction occurred, where austenite and type D graphite were formed, followed by the metastable eutectic reaction, where ledeburite was formed which contains cementite and austenite. And pearlite shown in Figure 4(d) was formed as a eutectoid product at last.

4.3.5. Alloy 11Cr. During the solidification of alloy 11Cr, as shown in Figure 11(e), the hexagonal shaped M_7C_3 formed first as the primary phase. As the temperature decreases, eutectic reaction occurred and formed M_7C_3 and austenite into a ledeburite-shaped structure. As the temperature reduced, very few primary graphite was formed as the primary phase for stable eutectic reaction followed by the stable eutectic reaction, where austenite and type D graphite were formed. Meanwhile, part of the M_7C_3 carbide was transformed into cementite (Fe_3C), as seen in Figure 11(e) at temperatures below 1126°C. Further ASPEX-EDS analysis in Figure 9 and Figure 12 confirmed that the carbide in ledeburite-shaped structure for alloy 11Cr has a similar Fe/Cr ratio with the cementite in alloys 7Cr and 9Cr. Electron Backscatter Diffraction (EBSD) was used to confirm the phase constituent in alloy 11Cr. As is shown in Figure 13, EBSD analysis was conducted on an area including both carbide in the ledeburite-shaped structure and

primary hexagonal shaped carbide. And Figure 13(b) shows most of the carbides in ledeburite-shaped structure are cementite, while the primary hexagonal shaped carbide is still M_7C_3 except few cementite around it. More details are discussed in later section. Finally starting at the critical temperature A_1, austenite transformed into pearlitic structure shown in Figure 4(e).

Overall, the schematics of solidification sequence for each alloy are shown in Figure 14.

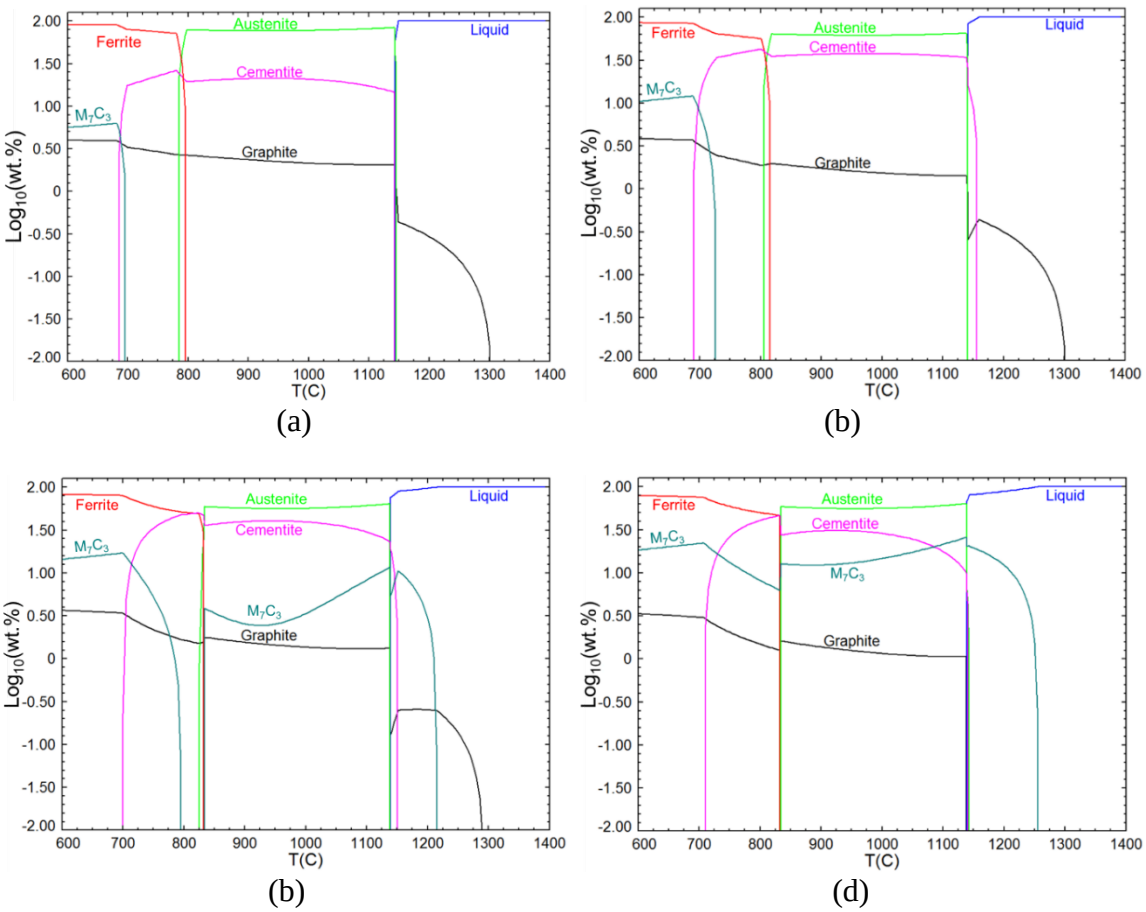

Figure 11. Schematics of equilibrium step diagram calculated using Factsage for: (a) 3Cr; (b) 5Cr; (c) 7Cr; (d) 9Cr; (e) 11Cr.

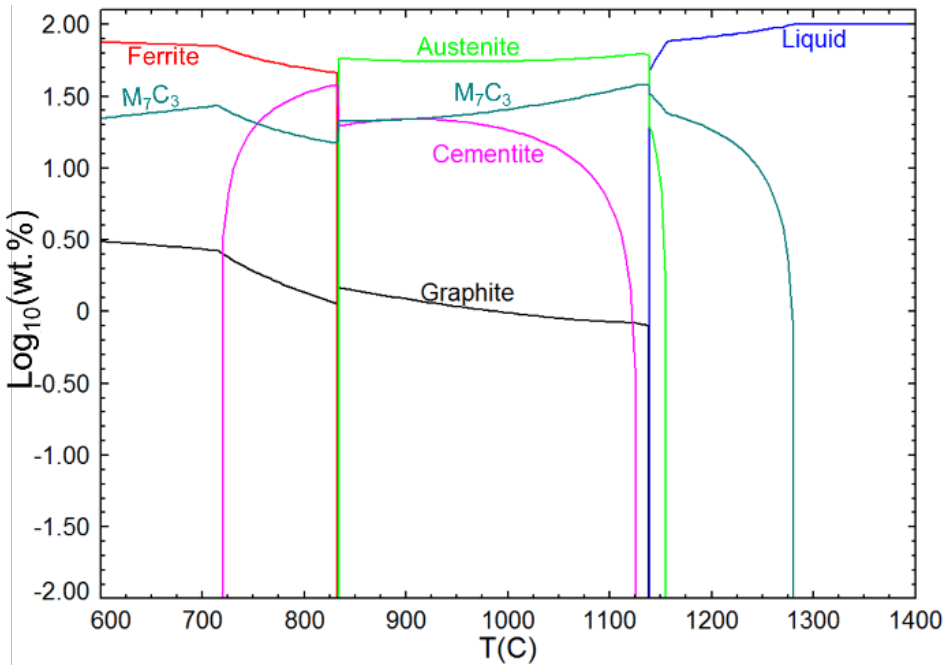

(e)

Figure 11. Schematics of equilibrium step diagram calculated using Factsage for: (a) 3Cr; (b) 5Cr; (c) 7Cr; (d) 9Cr; (e) 11Cr (cont.).

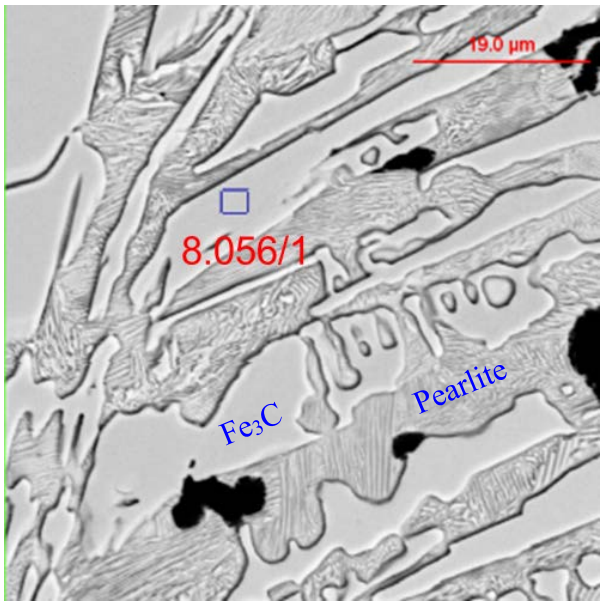

Figure 12. Fe/Cr(wt.%) ratio for carbide in ledeburite-shaped structure for alloy 11Cr.

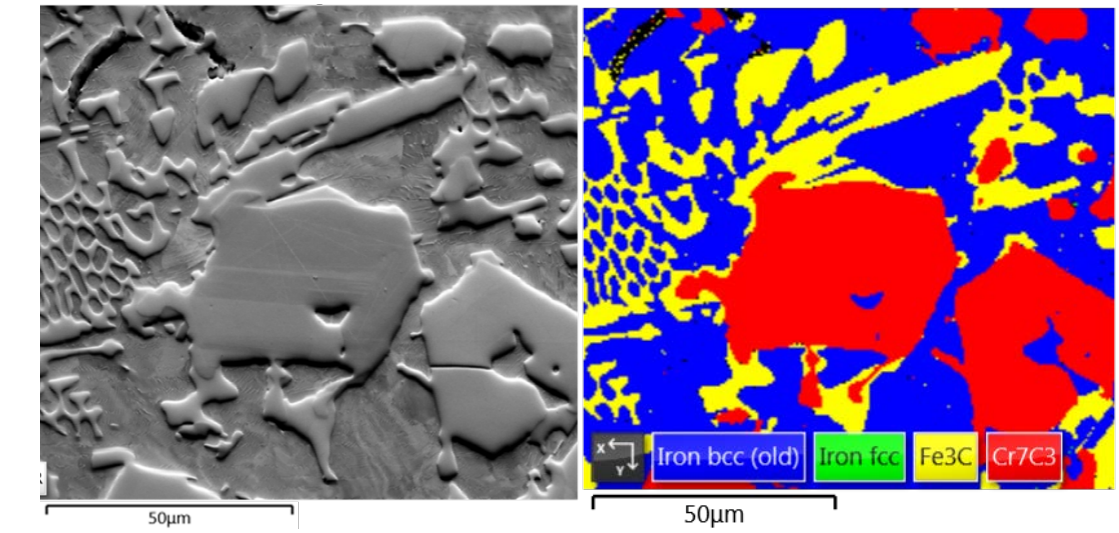

Figure 13. Schematics of: (a) SEM image of alloy 11Cr taken by an EBSD forescatter detector; (b) EBSD phase mapping including spots where Kikuchi pattern was taken for each phases; (c) Indexed Kikuchi pattern for ferrite obtained at spot 1; (d) Indexed Kikuchi pattern for Fe_3C obtained at spot 2; (e) Indexed Kikuchi pattern for M_7C_3 at spot 3.

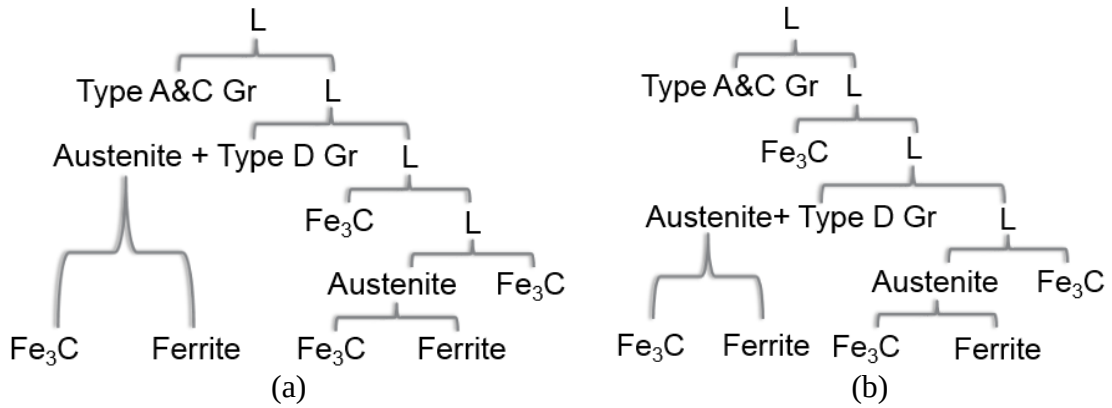

Figure 14. Schematics of solidification sequence: (a) 3Cr; (b) 5Cr; (c) 7Cr; (d) 9Cr; (e) 11Cr.

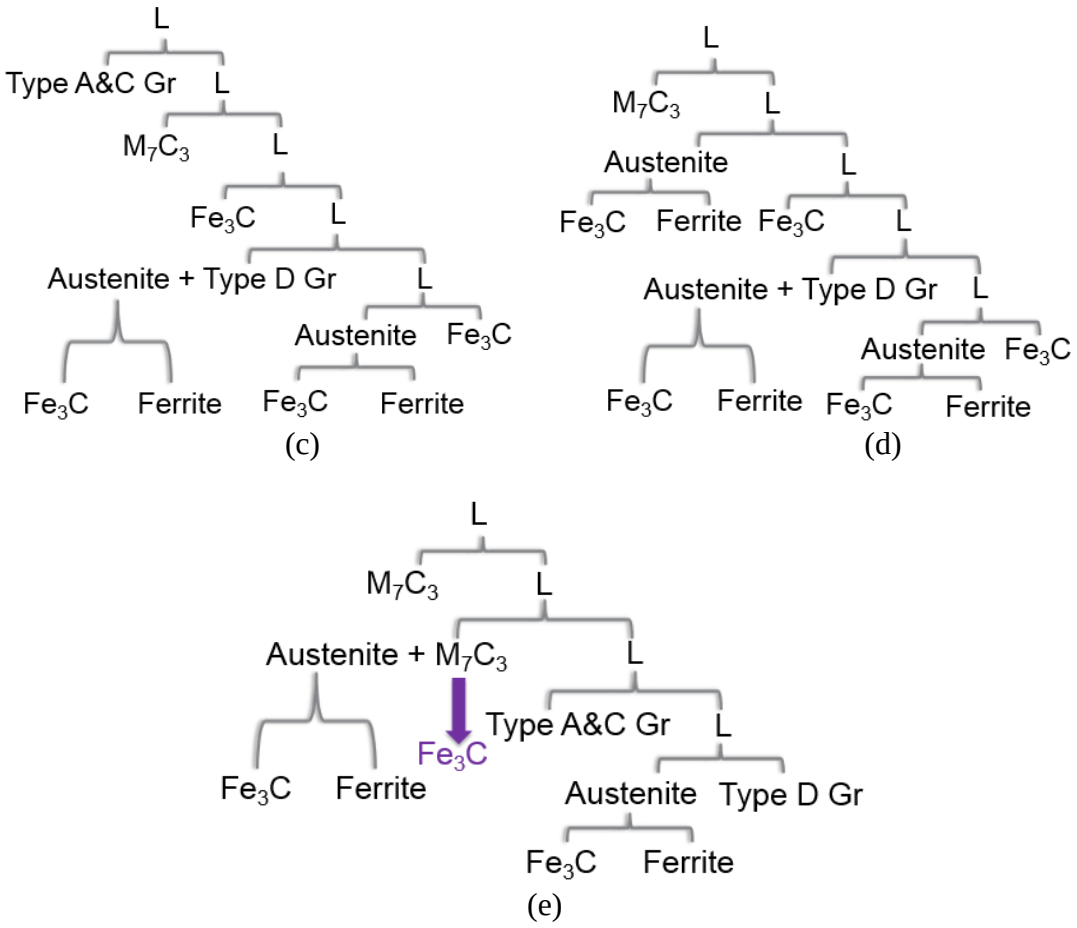

Figure 14. Schematics of solidification sequence: (a) 3Cr; (b) 5Cr; (c) 7Cr; (d) 9Cr; (e) 11Cr (cont.).

4.4. M_7C_3 TO Fe_3C TRANSFORMATION IN LEDEBURITE-SHAPED STRUCTURE IN ALLOY 11CR

Since both Skobir [34] and Inoue [35] claimed that M3C can transform into M_7C_3 during a tempering process in high Cr white iron, to further verify that the Fe_3C in ledeburite-shaped structure was originally transformed from M_7C_3, a heat treatment was done on alloy 11Cr. A small piece of metal sectioned from alloy 11Cr was sealed with inert argon gas in a quartz tube to avoid decarburization during the heat treatment. The sample was heat treated for four hours at a temperature 1122°C, which is right below

solidus temperature in a SiC box furnace and then quenched in agitating water. EBSD technique again was used to confirm the phase constituent in alloy 11Cr after heat treatment. As is shown in Figure 15(a), EBSD analysis was performed on the ledeburite-shaped structure to verify the phase constituent in the ledeburite-shaped structure in this heat treated alloy 11Cr. The Figure 15(b) is an EBSD phase mapping and shows both M_7C_3 and Fe_3C are existing in the ledeburite-shaped structure after the heat treatment, which means this specimen was quenched in a state where M_7C_3 and Fe_3C are co-existing. The Cr EDS mapping in Figure 15(c) shows that the M_7C_3 in the ledeburite-shaped structure has a higher Cr content compared with Fe_3C. The Cr content in both M_7C_3 and Fe_3C in the ledeburite-shaped structure was measured using SEM-EDS, and compared with the Cr content calculated from FactSage equilibrium modulus in Figure 16. It is shown that the Cr content in M_7C_3 is about twice of that in Fe_3C, although the measured Cr contents are slightly lower than the calculated Cr contents, which is due to the reaction volume effect in the SEM-EDS. Consequently, M_7C_3 is proved to be the initial carbide in the ledeburite-shaped structure during the solidification and was transformed into Fe_3C at a lower temperature. It is worth noting that the temperature range between solidus temperature and M_7C_3 in ledeburite-shaped structure transformation temperature is too narrow to capture a stage where only M_7C_3 but no Fe_3C exists in the ledeburite-shaped structure. The red dashed line in Figure 16 represents the temperature used for this heat treatment. The difference to Inoue's [35] work could be resulted from different Cr content. In this work, at lower Cr content (11wt.% vs 18wt.%), Fe_3C is more stable at temperature below 1100°C.

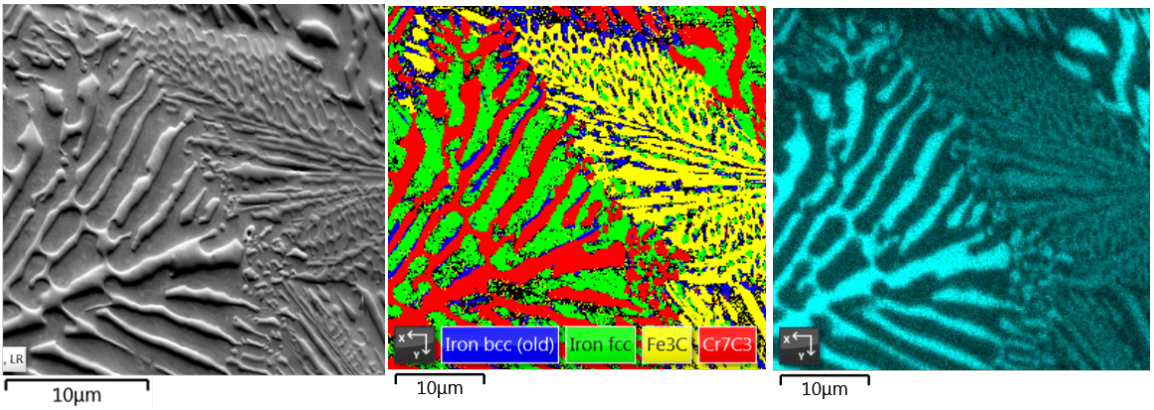

(a) (b) (c)

Figure 15. Schematics of heat treated alloy 11Cr: (a) SEM image taken by an EBSD forescatter detector; (b) EBSD phase mapping on ledeburite-shaped structure; (c) Cr EDS mapping.

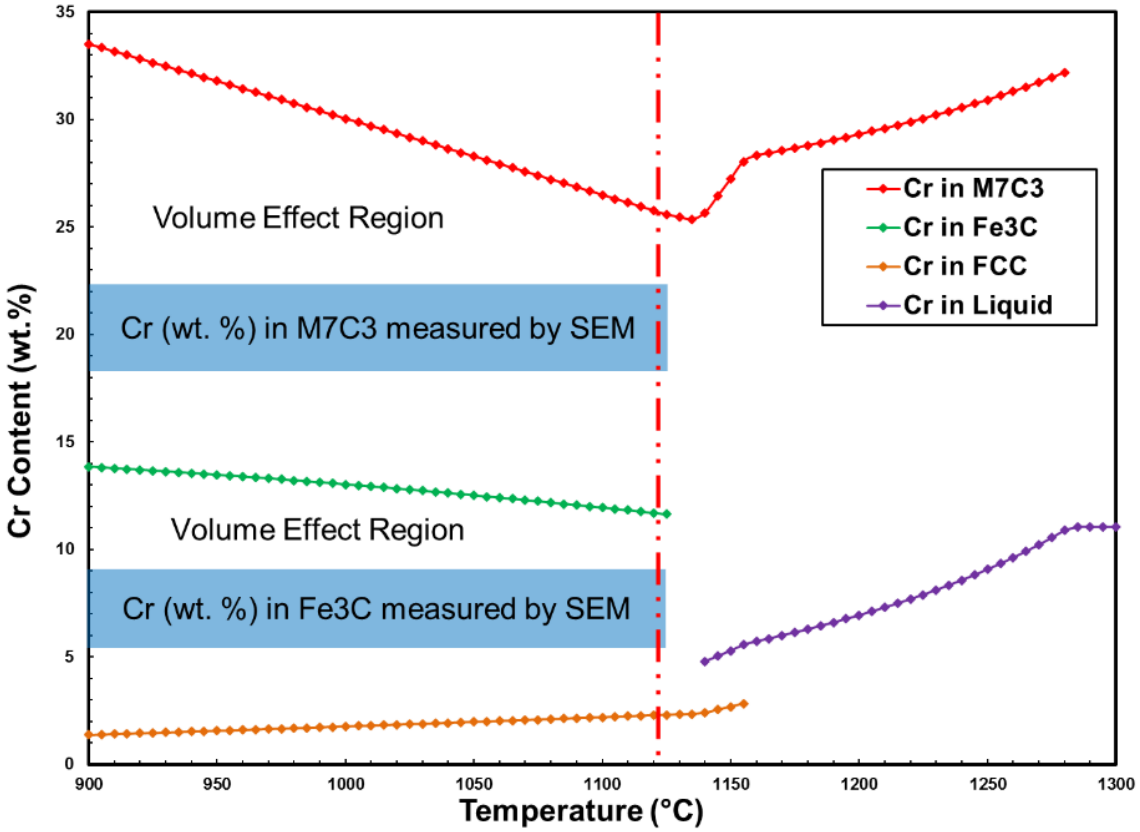

Figure 16. Change of Cr content in wt.% versus temperature in different phases calculated using FactSage equilibrium module. The blue regions represent the Cr wt.% measured by SEM-EDS for M_7C_3 and Fe_3C both in ledeburite-shaped structure. The Red dashed line represents the temperature used for heat treatment.

4.5. VICKERS INDENTATION HARDNESS ANALYSIS

Hardness is related to wear resistance of the metal. To understand the hardness change at various chemistry level, Vickers indentation hardness was taken for primary plate cementite, hexagonal shaped M_7C_3 cross face and side face in accordance with ASTM standard E92 [36]. A Vickers scale of HV 0.05 (50gf test force) was used along with 10 seconds press time and 40x objective magnification to ease the measurements and ensure the testing condition was coherent. Figure 17 shows an average of ten measurements with an error bar showing 95% CL uncertainty range [28]. By comparing the Vickers hardness of each phase and their Fe/Cr(wt.%) ratio listed in Table 3, one can conclude that: (1) Hexagonal shaped M_7C_3 is harder than plate cementite; (2) Hardness of hexagonal shaped M_7C_3 and plate cementite increases with increasing Cr content; (3) Cross face is harder than Side face in the hexagonal shaped M_7C_3 which indicates the close packed plane is the hardest plane in HCP structure for M_7C_3, and this is consistent with both Wang's and Coronado's investigations, respectively [37-38].

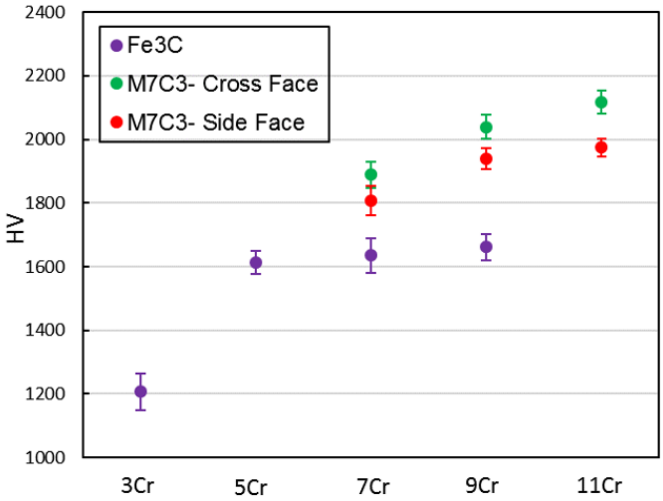

Figure 17. Schematics of Vickers indentation hardness with a parameter of 490.6mN press load, 10s press time and 40x objective magnification.

5. CONCLUSION

Five graphitic white iron alloys have been designed, cast and investigated. Graphite and carbides (excluding carbides in pearlite) percent measured using ImageJ matches thermodynamic calculation results using FactSage equilibrium module. Two numerical models were constructed to guide future design efforts: 1) graphite volume percent increases linearly with increasing carbon equivalent; 2) graphite volume percent needs to be at least 7% to be effective on increasing the thermal conductivity of the alloys.

Solidification sequences for each alloy have be determined based on microstructures and FactSage equilibrium step diagrams. Over the investigated five alloy compositions, as Cr content in bulk materials increases, 1) the Cr content in M_7C_3 carbide increases, 2) M_7C_3 carbides start to be the primary phase, and the morphology of M_7C_3 carbide becomes more regular and closer to hexagonal, 3) carbon competition is more favorable towards carbides formation. At higher Cr content, alloy 11Cr, M_7C_3 and austenite were formed during the metastable eutectic reaction at early stage, then as the temperature decreases, M_7C_3 in the ledeburite-shaped structure was transformed into cementite. Moreover, the presence of M_7C_3 in ledeburite-shaped structure at high temperature during the early stage metastable eutectic reaction was verified by EBSD analysis on the heat-treated specimen.

It was also observed that M_7C_3 carbide has a transformed austenite core structure along its [0001] direction. Vickers hardness measurements show that, in these austenite-cored M_7C_3 carbides, cross face is harder than side face. When comparing the hardness

between different phases and chemistries, M_7C_3 carbide is harder than plate cementite, and hardness of M_7C_3 and plate cementite increases with increasing Cr content.

ACKNOWLEDGEMENTS

This work was financially supported by Caterpillar Inc. The authors are grateful for the technical discussion with Dr. David C. Van Aken. Perrin W. Habecker is acknowledged for his assistance with the experiments and sample preparations. The FEI Helios NanoLab EBSD was obtained with a Major Research Instrumentation grant from the National Science Foundation under contract DMR-0723128.

REFERENCES

[1] D. M. Stefanescu: *ASM Handbook,* 10th ed., ASM International, 1990, vol. 1, pp. 3-11.

[2] H. Berns and W. Theisen: *Ferrous Materials,* 1st ed., Springer- Verlag Berlin Heidelberg, 2008, pp. 103.

[3] R. B. Gundlach: *ASM Handbook,* ASM International, 2008, vol. 15 pp. 896-903.

[4] M. Mohammadnezhad, V. Javaheri, M. Shamanian, M. Naseri and M. Bahrami: *Materials & Design,* 2013, vol. 49, pp. 888-893.

[5] M. Filipovic, Z. Kamberovic and M. Korac: *Materials Transactions,* 2011, vol. 52, pp. 386-390.

[6] A. Bedolla-Jacuinde, M. W. Rainforth and I. Mejia: *Metall. Trans. A*, 2013, vol 44, pp. 856-872.

[7] Z. F. Huang, J. D. Xing, X. H. Zhi and Y. M. Gao: *Materials Science and Technology,* 2014, vol. 27, pp. 426-430.

[8] W. T. Yu, J. Li, C. B. Shi and Q. T. Zhu: *Metals*, 2016, vol. 6, pp. 193.

[9] X. H. Zhi, J. D. Xing, H. G. Fu and Y. M. Gao: *Materials Characterization*, 2008, vol. 59, pp. 1221-1226.

[10] A. Bedolla-Jacuinde, R. Correa, J. G. Quezada and C. Maldonado: *Materials Science and Engineering A*, 2005, vol. 398, pp. 297-308.

[11] X. J. Wu, J. D. Xing, H. G. Fu and X. H. Zhi*: Materials Science and Engineering A*, 2007, vol. 457, pp. 180-185.

[12] M. E. Maja, M. G. Maruma, L. A. Mampuru and S. J. Moema: *Journal of the Southern African Institute of Mining and Metallurgy*, 2016, vol. 116, pp. 981-986.

[13] *Annual Book of ASTM Standards*, ASTM Designation A247-17, ASTM, 2017.

[14] C. V. White: *Metals Handbook*, 10th ed., ASM International, 1990, vol. 1, pp. 12-32.

[15] W. L. Guesser, I. Masiero, E. Melleras and C. S. Cabezas: *Revista Materia*, 2005, vol. 10, pp. 265-272.

[16] D. Holmgren: *International Journal of Cast Metals Research*, 2013, vol. 18, pp. 331-345.

[17] I. G. Chen and D. M. Stefanescu: *AFS Transaction*, 1984, vol. 92, pp. 947-964.

[18] J. M. Frost and D. M. Stefanescu: *AFS Transaction*, 1992, vol. 100, pp. 189-200.

[19] D. Emadi, L. V. Whiting, S. Nafisi and R. Ghomashchi: *Journal of Thermal Analysis and Calorimetry*, 2005, vol. 81, pp. 235-242.

[20] A. Gaard, N. Hallback, P. Krakhmalev and J. Bergstrom: *Wear*, 2010, vol. 268, pp. 968-975.

[21] P. C. Okonkwo, G. Kelly, B. F. Rolfe and M. P. Pereira: *Wear*, 2012, vol. 282-283, pp. 22-30.

[22] J. Krawczyk and J. Pacyna: *Metallurgy and Foundry Engineering*, 2009, vol. 35, pp. 101-110.

[23] J. Krawczyk and J. Pacyna: *18th International Conference on Metallurgy and Materials*, 2009, pp. 19-21.

[24] J. Krawczyk and J. Pacyna: *Archives of Foundry Engineering,* 2010, vol. 10, pp. 45-50.

[25] J. J. Coronado, A. Gomez and A. Sinatora: *Wear*, 2009, vol. 267, pp. 2070-2076.

[26] J. J. Coronado and A. Sinatora: *Wear*, 2009, vol. 267, pp. 2077-2082.

[27] J. J. Coronado, S. A. Rodriguez, C. E. K. Mady and A. Sinatora: *Abrasion Wear Resistant Allowed White Cast Iron for Rolling and Pulverizing Mills,* 2008, pp. 212-221.

[28] D. C. Van Aken and W. F. Hosford*: Reporting Results: a practical guide for engineers and scientists*, 1st ed., Cambridge University, 2008, pp. 87-91.

[29] M. D. Hecht, B. A. Webler and Y. N. Picard: *Metall. Trans. A*, 2018, vol. 49, pp. 2161-2172.

[30] M. Bruneau, C.M. Uang and A. S. Whittaker: *Ductile design of steel structures*, 1st ed., McGraw-Hill Education, 1998.

[31] A. A. Zhukov: *Theoretical foundations of graphitization of cast iron and formation of structure in preforms,* 1978.

[32] S. Q. Ma, J. D. Xing, Y. L. He, Y. F. Li, Z. F. Huang, G. Z. Liu and Q. J. Geng*: Materials Chemistry and Physics,* 2015, vol. 161, pp. 65-73.

[33] L. Sha, Y.F. Zhou, X. L. Xing, J. B. Wang, X. J. Ren and Q. X. Yang: *Scientific Reports* 2016, vol. 6.

[34] D. A. Skobir, F. Vodopivec, M. Jenko, S. Spaic and B. Markoli: *Zeitschrift fur Metallkunde,* 2004, vol. 95, pp. 1020-1024.

[35] A. Inoue and T. Masumoto: *Metallurgical Transaction A*, 1980, vol. 11, pp. 739-747.

[36] *Annual Book of ASTM Standards*, ASTM Designation E92-17, ASTM, 2017.

[37] S. R. Wang, L. H. Song, Y. Qiao and M. Wang: *Tribology Letters,* 2013, vol. 50, pp. 439-448.

[38] J. J. Coronado: *Wear*, 2011, vol. 270, pp. 287-293.

III. DEVELOPING A GRAPHITIC WHITE IRON FOR ABRASIVE WEAR APPLICATION: THERMAL AND WEAR PROPERTIES

Jie Wan[1], David C. Van Aken[1], Jingjing Qing[2], Thomas J. Yaniak[3], Thomas E. Clements[3], Mingzhi Xu[2]

[1]Missouri University of Science and Technology, Rolla, MO 65401, USA

[2]Georgia Southern University, Statesboro, GA 30460, USA

[3]Caterpillar Inc., Peoria, IL 61552, USA

Tel: 573-578-3874

Email: jwvt7@mst.edu

Keywords: Graphitic White Iron, Alloy Design, Three-Body Abrasion, Thermal Diffusivity

ABSTRACT

Frictional heat generated in high speed sliding and rolling wear generates a significant amount of heat. Metal loses a large portion of hardness at high temperature, making it more susceptible to failures. Temperature rise due to abrasive wear on contact surface is a serious issue that limits the lifetime of many metal-to-metal contact wear systems. Five flake graphite containing white irons with different chromium and carbon contents (graphitic white irons) were designed, cast and investigated by the authors to solve this problem. This study examined the introduction of flake graphite into a white iron to increase the net thermal diffusivity, and to improve the abrasive wear resistance. Thermal diffusivity was measured using the laser flash method following ASTM E1461 and thermal diffusivity increased with increasing graphite volume percentage. Abrasive

wear resistance was evaluated utilizing a dry sand/rubber wheel apparatus following ASTM G65 Procedure A, and it was found that 1 vol% graphite was equivalent to an increase in wear resistance resulting from a hardness increment of 2.3 HRC, which benefited from the evaluated thermal diffusivity. Several numerical models were established to correlate hardness, microstructure, thermal and wear properties with the developed carbon equivalent. Comparisons with other commonly used alloys showed that the graphitic white irons had comparable wear performance to a premium high molybdenum, high chromium, white iron, but the alloy cost was 90% lower.

1. INTRODUCTION

Wear is defined by ASTM G40 as “alteration of a solid surface by progressive loss or progressive displacement of material due to relative motion between that surface and a contacting substance or substances” [1]. Kato [2] categorized wear into four basic types: abrasive wear, adhesive wear, fatigue wear, and corrosive wear. As a major problem in various industries, the cost induced by abrasive wear is high and has been estimated as ranging from 1 to 4% of the gross national product of an industrialized nation [3]. According to the type of contact and contact environment, abrasive wear is typically categorized into two-body or three-body abrasive wear. Two-body abrasive wear commonly occurs when the abrasive particles are constrained, and remove material from the opposite surface, whereas the abrasive particles are not constrained, and free to roll and slide down surfaces in three-body abrasive wear. A dry sand/rubber wheel apparatus is often used to quantitatively assess three-body abrasive wear performance due

to the ease of utilization and its high reproducibility [4-6]. There are many factors affecting three-body abrasive wear, such as specimen hardness, spinning speed, force, temperature, and particle size. While most of these influencing factors have been thoroughly investigated, only a few investigations have reported the effect of specimen temperature increase on the wear behavior. Frictional heating of the test specimen is one of the attributes of the dry sand/ rubber wheel test and that the wear rate increases with increasing temperature [7,8], which could be due to the fact that hardness decreases with increasing temperature [9]. The authors are unaware of any studies where graphite flake addition to white iron have been used to thermally manage specimen heating during abrasive wear.

High Cr white irons are widely used in both abrasive and adhesive wear applications because it contains M_7C_3 carbide of high hardness (1100-1600 HV) [10]. M_7C_3 carbides appear as hexagonal shaped rods in high Cr white iron and serve as "stoppers" in terminating a penetrating wear gouge or scar [4]. However, Cr content also decreases thermal diffusivity of white iron and make it more susceptible to abrasive wear [11]. Natarajan found that graphite addition enhanced the abrasive wear resistance of plasma sprayed NiCrBSi coatings [12]. Addition of graphite to white iron mill rolls has also been shown to improve wear resistance. These mottled cast iron microstructures usually contain spheroidal graphite, which may not be optimum with respect to improving thermal diffusion [13-18]. It was found the thermal diffusivity of a cast iron increases with decreasing nodularity [19], and flake graphite has the best thermal diffusivity compared with the vermicular graphite and spheroidal graphite. To take the advantage of both high wear resistance of M_7C_3 carbides and high thermal diffusivity of

flake graphite, the authors designed and produced the first generation of graphitic white iron [20-22].

In the present investigation, the authors studied the microstructure, hardness, thermal diffusivity and abrasive wear performance. The designed alloys were treated as a composite material to quantify the graphite effect on the thermal diffusivity. Numerical models correlating the chemistry and phase constituents to thermal diffusivity and wear resistance were also developed.

2. MATERIALS AND METHODS

2.1. MATERIAL DEVELOPMENT

In the present investigation, the primary phases formed during the solidification for ferrous alloys containing 2wt.%Si, 0.5wt.%Mn, and a range of carbon (0-8 wt.% C) and chromium (0-30 wt.% Cr) contents were calculated using FactSage Equilibrium module (version 7.1, using database FSstel). As shown in Figure 1, carbon promotes the formation of graphite, while chromium promotes the formation of M_7C_3 and ferrite. It should be noted that Figure 1 is a liquidus projection, and primary phases are formed at different temperature across the studied carbon and chromium range. To take advantages of both thermal diffusivity from graphite and hardness from carbides, three hypereutectic and two hypoeutectic chemical compositions were selected for this study, with the goal to produce graphite flakes of high thermal diffusivity, and M_7C_3 carbide with high wear resistance. The alloys were named as 3Cr, 5Cr, 7Cr, 9Cr and 11Cr, based on the Cr

content in the alloy and are shown in Figure 1. Numbers in the parentheses in the legend show the weight percentage of Cr and C for each alloy.

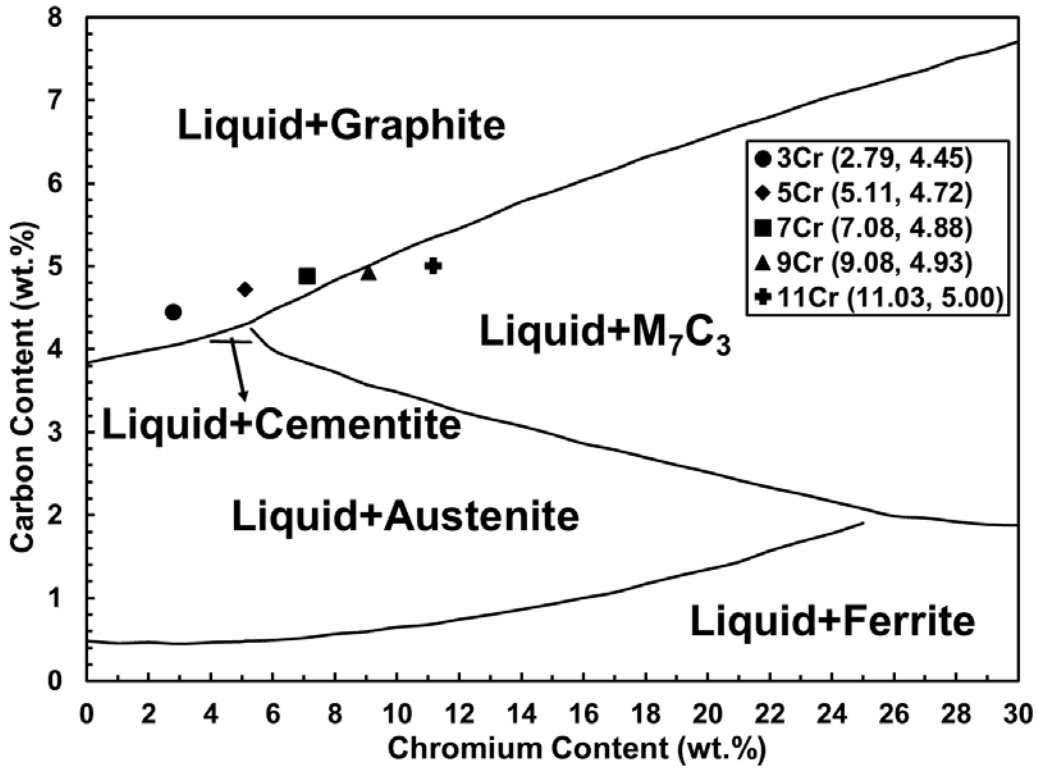

Figure 1. Primary phase formed during solidification for ferrous alloy containing 2wt.%Si-0.5wt.%Mn, and different levels of C and Cr.

To accurately control the chemistry, high purity charge materials including induction iron, graphite, low carbon ferrochrome, ferrosilicon and ferromanganese were melted in a coreless induction furnace to produce the five alloys. Additionally, 0.15wt.% graphite inoculant (Fe-Si-Sr-Zr) was added into the sprue well prior to each pour to promote formation of graphite. Metal was cast into no-bake keel block sand molds and a superheat of 200 ºC was used for each alloy. Figure 2 shows an example of the actual casting. The chemical compositions of the five alloys produced are given in Table 1.

Calculated values for the liquidus, solidus and eutectoid temperature are reported in Table 2 along with the measured pouring temperature.

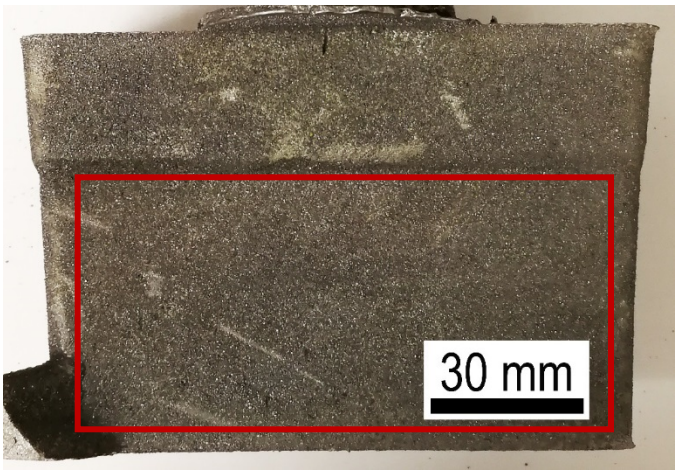

Figure 2. An example of a keel block casting produced.

Table 1. Composition of the five alloys analyzed using an optical emission spectrometer and Leco combustion C/S analyzers.

Alloys	Chemical composition (wt.%)					Inoculant (wt.%)
	Leco C	Leco S (ppm)	Si	Mn	Cr	
3Cr	4.45	154	2.06	0.44	2.79	0.15
5Cr	4.72	157	2.00	0.47	5.11	0.15
7Cr	4.88	184	2.07	0.49	7.08	0.15
9Cr	4.93	198	2.05	0.50	9.08	0.15
11Cr	5.00	170	2.03	0.50	11.03	0.15

Table 2. Pertinent temperature information for the five alloys studied.

Alloys	Temperature (K)			
	A_1	Solidus	Liquidus	Pouring Temperature
3Cr	1071 (798 ºC)	1415 (1142 ºC)	1578 (1305 ºC)	1778 (1505 ºC)
5Cr	1091 (818 ºC)	1412 (1139 ºC)	1577 (1304 ºC)	1777 (1504 ºC)
7Cr	1107 (834 ºC)	1407 (1134 ºC)	1565 (1292 ºC)	1765 (1492 ºC)
9Cr	1107 (834 ºC)	1411 (1138 ºC)	1529 (1256 ºC)	1729 (1456 ºC)
11Cr	1107 (834 ºC)	1411 (1138 ºC)	1555 (1282 ºC)	1755 (1482 ºC)

2.2. SAMPLE PREPARATION AND CHARACTERIZATION

Specimens used for microstructural characterization, thermal diffusivity and wear resistance were prepared from the bottom part of the Y-block casting (box in Figure 2) where the amount of shrinkage porosity was a minimum. Samples for each test were sectioned from the same location with the same orientation for each alloy to minimize the effects of cooling rate as well as the orientation of carbide.

2.2.1. Metallographic Sample Preparation and Characterization.

Metallographic specimens were ground with silicon carbide papers from 180 to 1200 grit and polished using 3 µm and 0.1 µm diamond paste. As-polished samples were used to study the graphite morphology and volume percent, and the second set of samples were etched with 2% nital to reveal different carbides as well as the matrix microstructure. Graphite volume percent was estimated by measuring area percent using the ImageJ contrast threshold method on images obtained by optical microscopy. [20,21]. Phase mapping via electron backscattered diffraction (EBSD) pattern analysis was performed on a Helios Nanolab 600 FIB system using a Nordlys detector and the AZtec 3.3 software package. An accelerating voltage of 20.0 kV, an emission current of 5.5 nA, and a step size of 57 nm were used for EBSD analysis. Vickers indentation hardness of M7C3 carbide in alloy 7Cr, 9Cr and 11Cr was measured on the 2% nital etched metallographic samples following ASTM E92 [23]. The parameters of 490.6 mN press load and 10 second press time were used.

2.2.2. Thermal Diffusivity Sample Preparation and Characterization.

Thermal diffusivity of each alloy was measured using a laser flash method following ASTM E1461 [24]. Five laser flash samples were prepared and measured for each alloy.

The dimension of the laser flash samples was 12.7 mm x 12.7 mm and the thickness of each sample was 3.0±0.2 mm. Both surfaces of the laser flash sample along with a thermographite standard were surface ground and spray coated with graphite to promote the heat absorption [24] and to achieve a consistent surface emissivity [25,26]. The thermal diffusivity of each sample was tested at temperatures of 200 ºC, 300 ºC, 400 ºC, 500 ºC, 600 ºC and 800ºC, respectively. Tests were repeated for three times at each testing temperature.

2.2.3. Wear Test Sample Preparation and Characterization. The abrasive wear resistance of the alloy produced was evaluated using a dry sand/rubber wheel apparatus following ASTM G65 Procedure A [27]. Three specimens of 12.7mm x 25.4mm x 76.2mm were prepared for each alloy for dry sand/rubber wheel wear testing. In addition to the five graphitic white irons, Hardox 400 and alloy Fe15Mo19Cr were also tested for comparison. Hardox 400 is a commercialized wear-resistant steel, which is commonly used as a reference in industries due to its consistent wear performance. Alloy Fe15Mo19Cr is a premium wear-resistant white iron that is currently used in metal-to-metal wear application. Each specimen was weighed before and after the wear test. The density of each alloy was measured utilizing Archimedes Principle, and the weight loss was then converted to volume loss. Lower volume loss reflects a higher wear resistance. To correlate the effect of graphite addition to the wear performance of graphitic white iron, the Rockwell hardness of each alloy was measured in C scale. The wear scars of each studied alloys were evaluated using the scanning electron microscope (SEM) to investigate the wear mechanism. The electron beam was operated at an

accelerating voltage of 20.0 kV and an emission current of 5.5 nA during image acquisition.

3. RESULTS

3.1. METALLOGRAPHIC MICROSTRUCTURE

Optical images of as-polished specimens showing graphite morphology and distribution are reported in Figure 3 and Figure 4 for the five alloys. Generally, flake graphite is divided into five types, where Type A graphite flakes have a random orientation, type B graphite has a rosette pattern, Type C graphite is kish graphite which is formed in hypereutectic cast irons, Type D graphite is randomly orientated very fine interdendritic flakes, and Type E graphite is very fine interdendritic flakes with a preferred orientation. Based on the above mentioned classification, Type A (arrows with round end) and Type C (arrows with rhomb end) flake graphite was observed in alloys 3Cr, 5Cr and 7Cr, as shown in Figure 3, in addition to Type D flake graphite (arrows with straight end) which was observed in all five alloys as shown in Figure 3 and Figure 4.

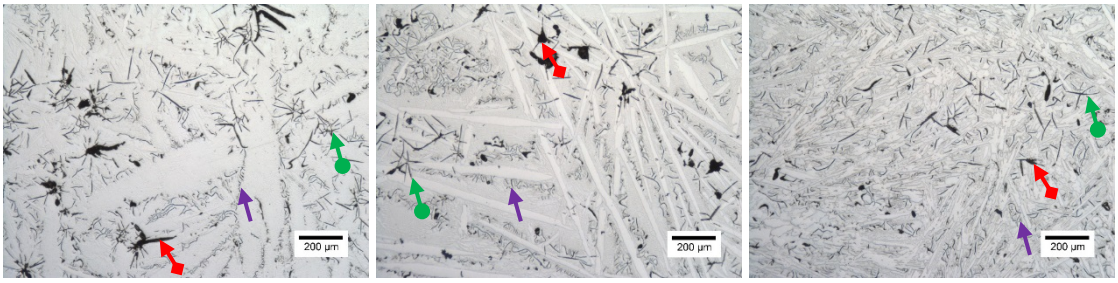

3Cr 5Cr 7Cr

Figure 3. As polished microstructures for alloys studied. Arrows with rhomb end indicate the Type C graphite, arrows with round end indicate the Type A graphite, and arrows with straight end indicate the Type D graphite.

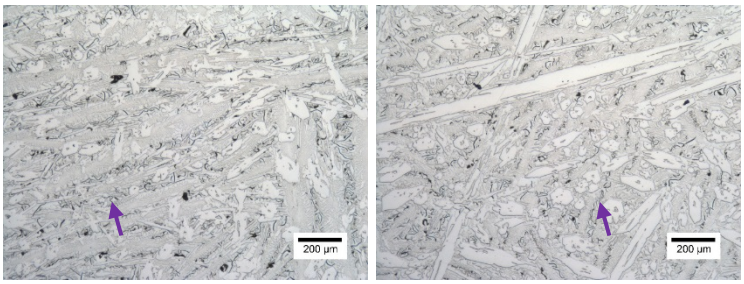

9Cr 11Cr

Figure 3. As polished microstructures for alloys studied. Arrows with rhomb end indicate the Type C graphite, arrows with round end indicate the Type A graphite, and arrows with straight end indicate the Type D graphite (cont.).

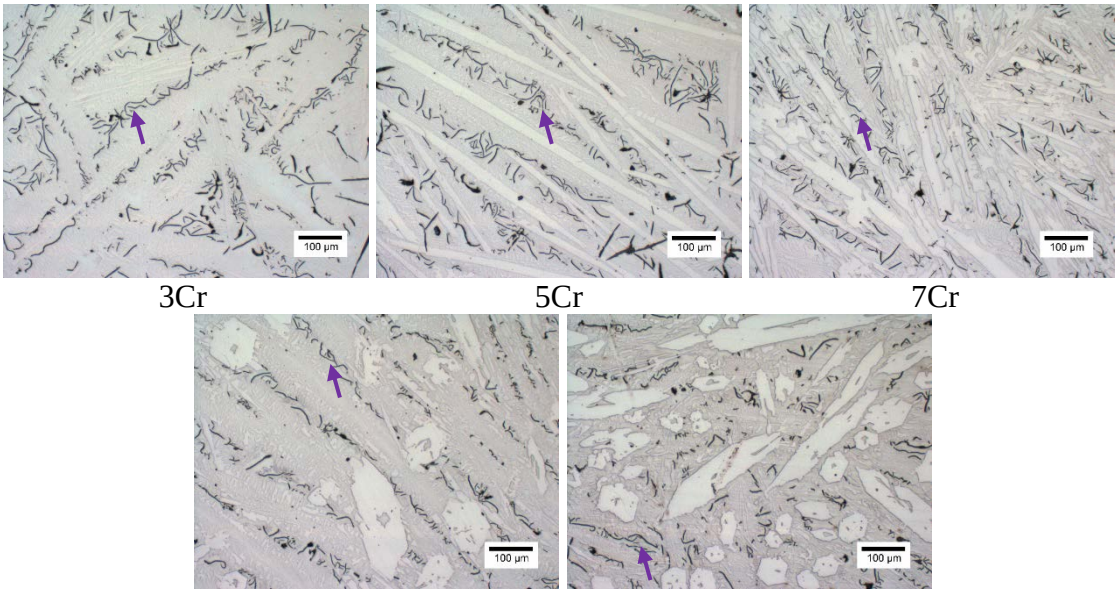

3Cr 5Cr 7Cr

9Cr 11Cr

Figure 4. As polished microstructures for alloys studied at a higher magnification. Arrows with straight end indicate the Type D flake graphite.

Different carbides and matrix phases were differentiated on the microstructures for the specimen etched with 2% nital, as shown in Figures 5 and 6. A detailed phase characterization procedure was described in authors' previously published work [20]. Both M_7C_3 carbide and M_3C carbide are shown as white phases in the optical microstructure. The arrows with straight end in Figure 5 highlight the plate cementite

(M_3C) carbides, and the arrows with round end label the M_7C_3 carbides. The matrix (other than graphite and carbide) is pearlitic in each of the graphitic white irons (see Figure 6).

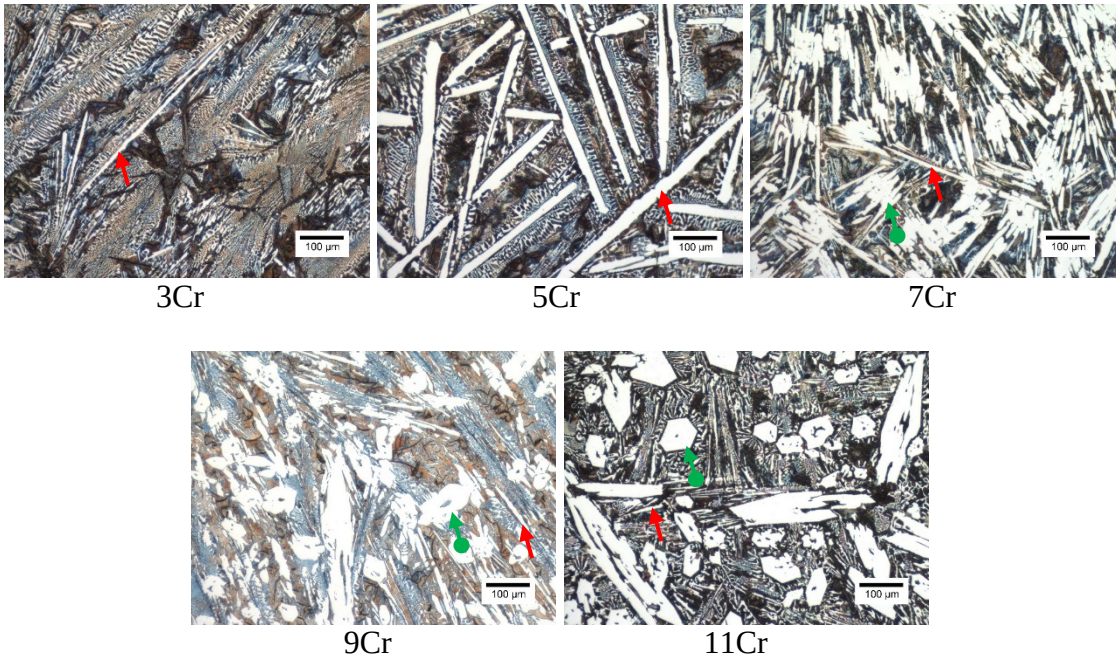

Figure 5. Carbides of different shapes observed on the etched micrographs of alloys studied. Arrows with straight end indicate plate cementite, arrows with round end indicate M_7C_3 carbide.

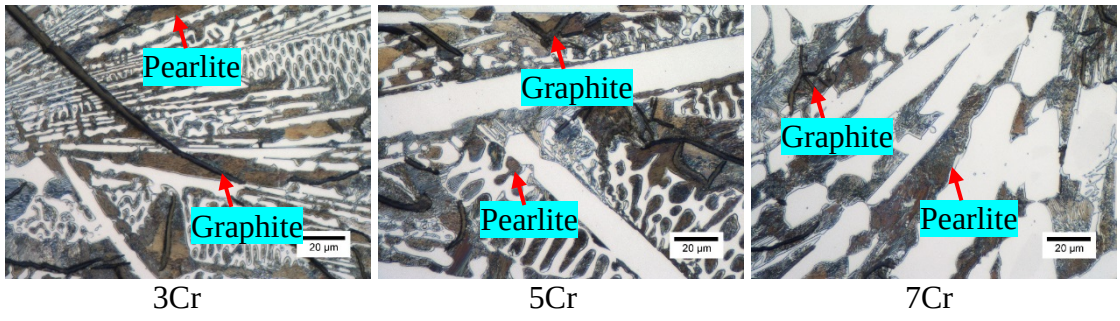

Figure 6. Pearlite in the matrix revealed using 2% nital etching in alloys studied. The highlighted black flakes are graphite particles.

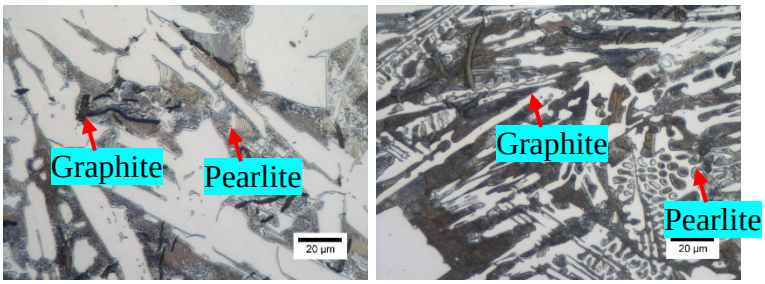

9Cr 11Cr

Figure 6. Pearlite in the matrix revealed using 2% nital etching in alloys studied. The highlighted black flakes are graphite particles (cont.).

Graphite volume percent determined by image analysis [20] varied between 3 and 10% and decreased as Cr content increased as shown in Figure 7. The graphite volume percent was averaged over ten different fields of view for each alloy, and the error bars in Figure 7 represent a 95% confidence level (CL) [28]. Carbide content was more difficult to quantify in optical images, but appeared to increase in volume with increasing Cr content [20].

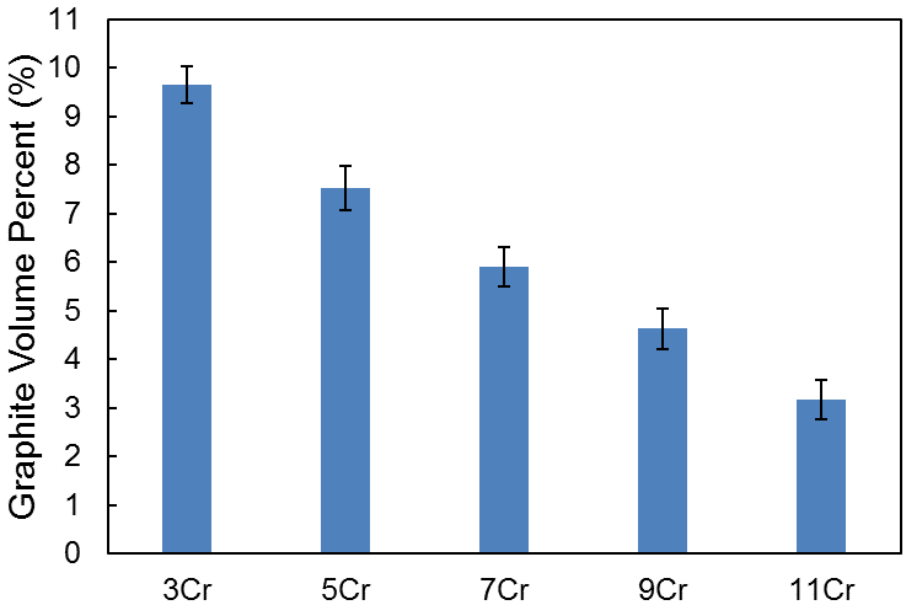

Figure 7. Measured graphite volume percent for the five alloys studied. Error bars represent a 95% CL.

3.2. THERMAL DIFFUSIVITY ANALYSIS

Figure 8 shows the averaged results at various temperatures with the error bars representing a 95% CL [28]. In general and within the testing temperature range measured, up to 800°C, thermal diffusivity decreased with increasing temperature for each of the graphitic white irons. Thermal diffusivity is also plotted against the graphite volume percent at different temperatures in Figure 9 and as expected an increasing thermal diffusivity was observed with increasing graphite volume percent.

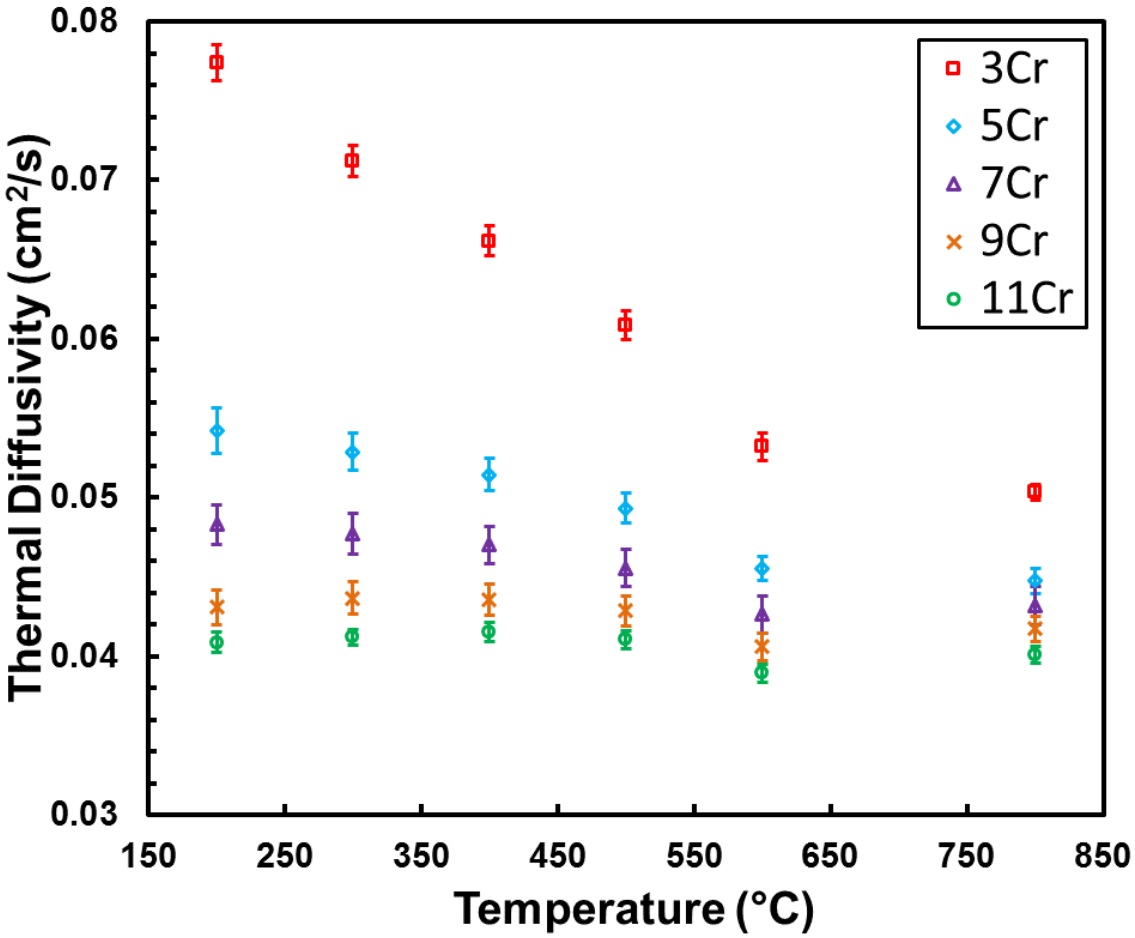

Figure 8. Thermal diffusivity results for five graphitic white irons. The alloy thermal diffusivity increases as the volume percent of graphite increases. Alloys in the legend are listed in order of graphite content with 11 Cr having the least graphite. Error bars represent a 95% CL.

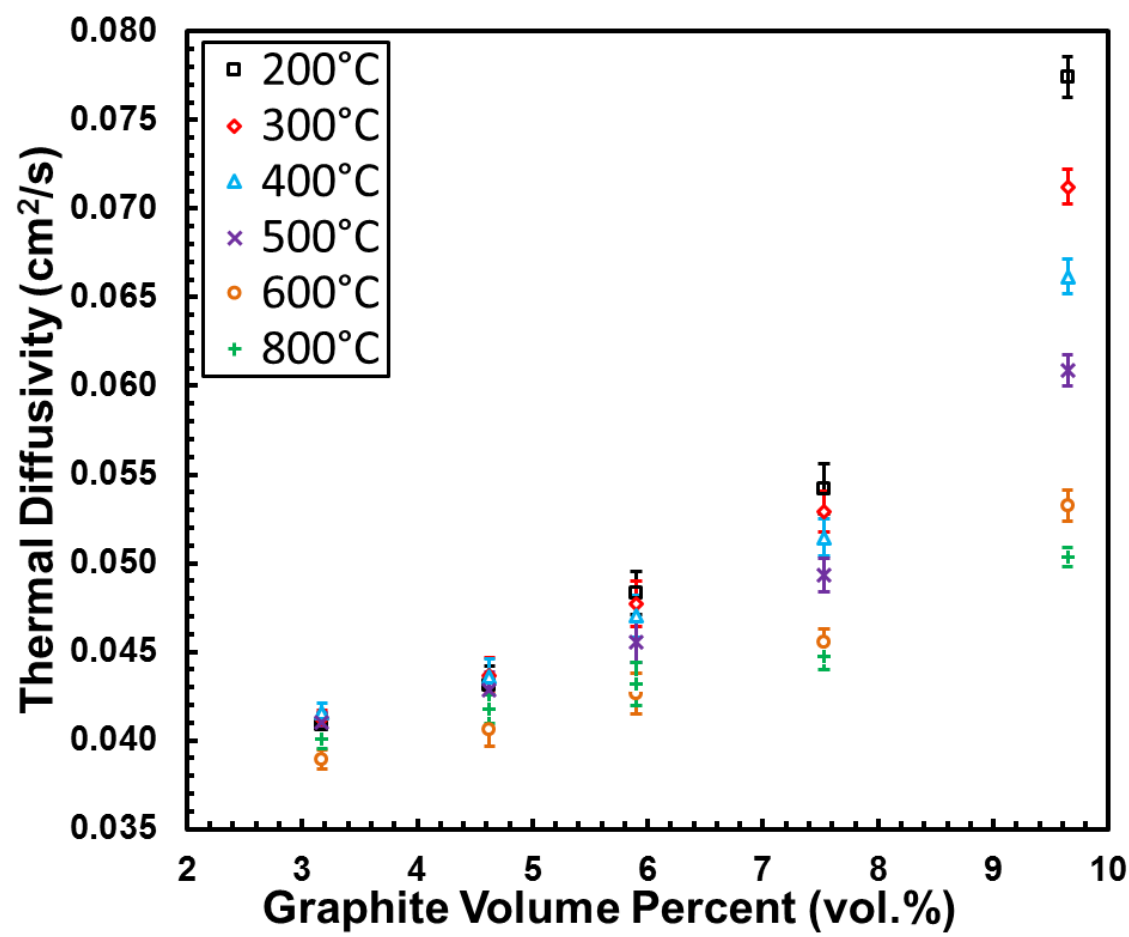

Figure 9. Measurements showing that a higher graphite volume percent improves the thermal diffusivity of the alloy at every testing temperature. Error bars represent a 95% CL.

3.3. WEAR PROPERTY ANALYSIS

Volume loss measurements are reported in Figure 10 for the dry sand/rubber wheel tests. Hardox 400 and Fe15Mo19Cr were also tested as a standard for comparison. Within the five graphitic white irons studied, alloy 9Cr had the best wear performance, which indicates that Cr content, carbide type or carbide hardness were not the only controlling factors for the wear resistance.

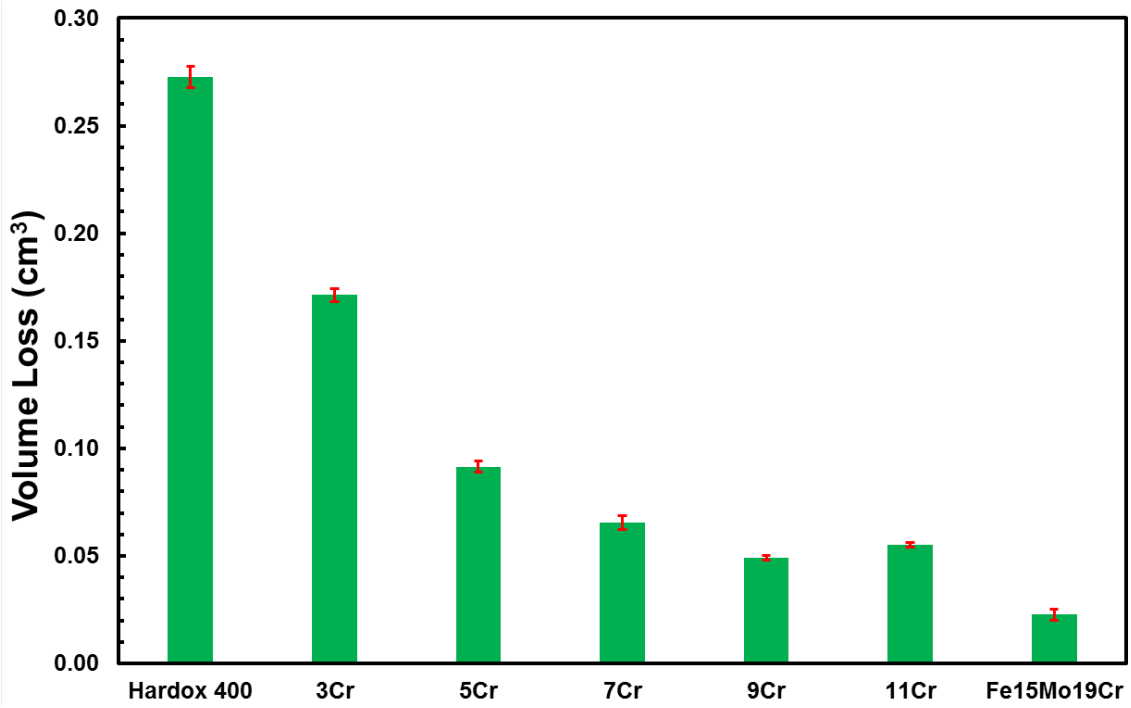

Figure 10. Volume loss of the five graphitic white irons studied compared to Hardox 400 and alloy Fe15Mo19Cr. Error bars represent a 95% CL.

3.4. WEAR SCARS EVALUATION

Wear scars were analyzed using SEM to determine the wear mechanism. Figure 11 shows the back scatted electron images of the wear scars for the five graphitic white irons as well as the alloys Fe15Mo19Cr. The matrix in alloy 3Cr was worn down almost evenly, due to a low fraction of hard phase in the alloy, as shown in Figure 11(a). Higher volume fraction of hard plate cementite was found in alloy 5Cr than alloy 3Cr [20] and these plate carbides worked as "stoppers" during particle ploughing or cutting during wear scar formation, see Figure 11(b). As for the alloy 7Cr shown in Figure 11(c), a combination of plate cementite and hexagonal shaped M_7C_3 carbide worked as "stoppers" to decrease the wear rate. Increasing the Cr content further as in 9Cr produced more M_7C_3 carbides, which show greater relief resulting from a higher intrinsic hardness than

the cementite [10], see Figures 11(c) and 11(d). The highest volume percent of M_7C_3 carbides was found in 11Cr as shown in Figure 11(e) although the volume loss was greater than that reported for 9 Cr. Alloy Fe15Mo19Cr also contains hexagonal-shaped M_7C_3 carbide as shown in Figure 11(f), but at a lower volume percent than observed for 9Cr. It should be noted that the premium Fe15Mo19Cr had the least volume loss and had a M_7C_3 carbide content comparable to 9Cr. A less worn-away volume was observed in in alloy Fe15Mo19Cr based on Figure 10, so the topographic height difference between the matrix and M_7C_3 carbides in the Fe15Mo19Cr iron appears smaller in Figure 11(f) when comparing to that in alloy 11Cr in Figure 11(e).

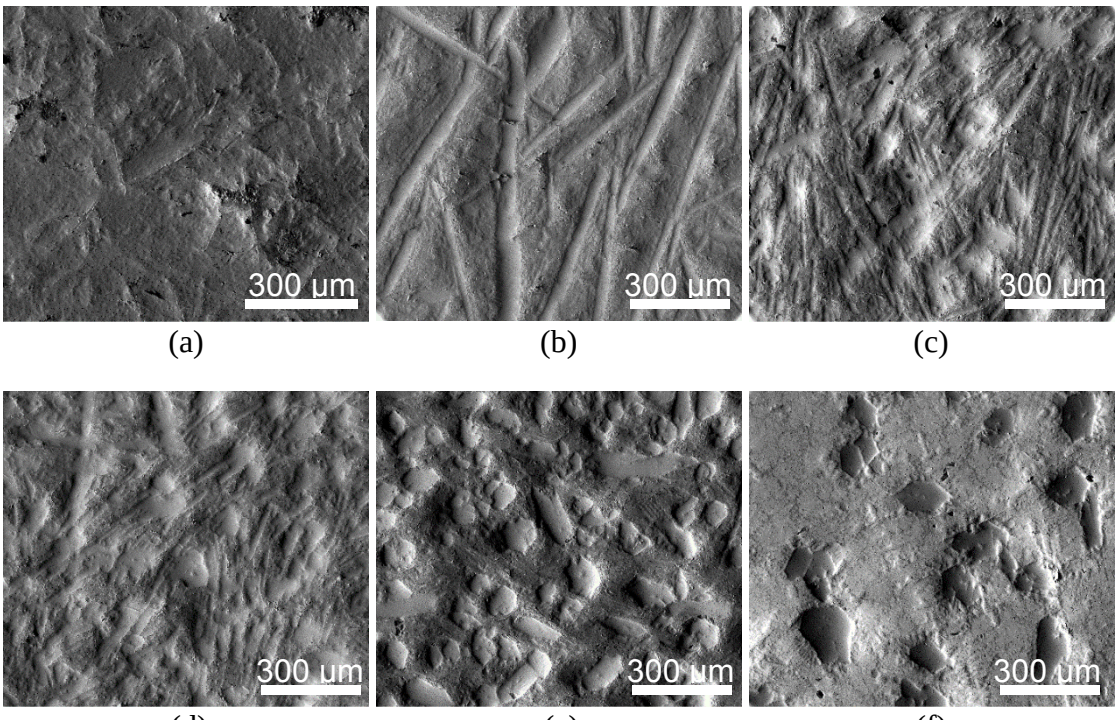

(a) (b) (c)

(d) (e) (f)

Figure 11. SEM back scattered electron images showing the topography information of wear scars for alloys (a) 3Cr; (b) 5Cr; (c) 7Cr; (d) 9Cr; (e) 11Cr; (f) Fe15Mo19Cr.

4. DISCUSSION

4.1. THERMAL DIFFUSIVITY INVESTIGATION

Thermal diffusivity of the graphite containing white irons was treated as a multiphase composite. Many numerical models have been established to calculate the effective thermal diffusivity and conductivity for composite materials [29-35]. One of the most popular models for an isotropic composite is the Hashin-Shtrikman model [30]. The alloys studied here can be treated as an isotropic composite material containing graphite since the graphite flakes are mostly discrete and randomly oriented. Furthermore, a lower bound analysis was found to better agree with the results. The lower bound of Hashin-Shtrikman model is shown in Eq. 1.

$$d = d_m + \frac{v_{Gr}}{1/(d_{Gr} - d_m) + v_m/3d_m} \quad (1)$$

where, d is the effective thermal diffusivity for the composite, d_m is the thermal diffusivity for the alloy excluding graphite, d_{Gr} is the thermal diffusivity for graphite, v_m is the volume fraction of the alloy excluding graphite and v_{Gr} is the volume fraction of graphite.

As described in Section 2.3, the measured thermal diffusivity of the thermographite was used as the thermal diffusivity of graphite and the measured thermal diffusivity of the alloys can be treated as the overall effective thermal diffusivity for the graphitic white iron composite. The thermal diffusivity of the alloys excluding graphite at each temperature was inversely calculated using Eq. 1. The calculated thermal

diffusivity of the alloy excluding graphite is different among the five alloys, as shown in Figure 12. Overall, thermal diffusivity of the alloy excluding graphite decreases with increasing Cr content in the bulk material.

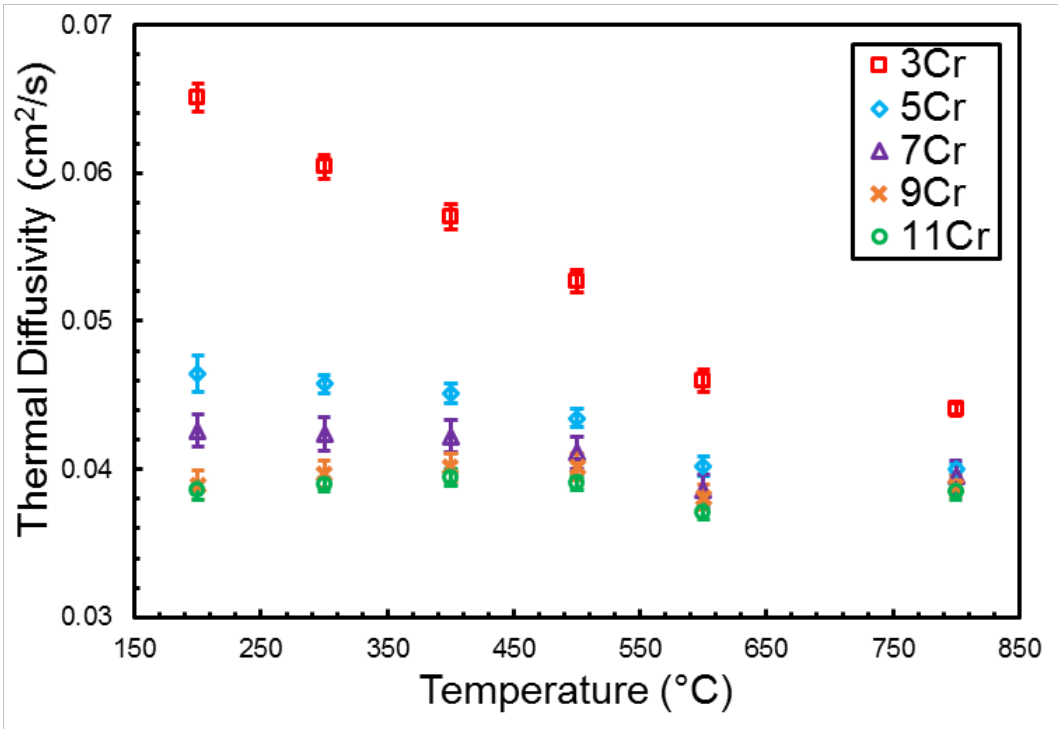

Figure 12. Thermal diffusivity of the alloy excluding graphite calculated using the lower bound of the Hashin-Shtrikman model [30]. Error bars represent a 95% CL.

To fully understand how the chemistry affects the thermal diffusivity of the alloy excluding graphite, the chemical composition of the alloy excluding graphite was calculated by deducting the carbon in the flake graphite particles (assumed 100% carbon) from the overall alloy composition listed in Table 1. The carbon equivalent of the alloy excluding graphite for each alloy was then calculated using the carbon equivalent equation [20] developed for the graphitic white iron shown as Eq. 2. The detailed

chemical composition for the alloy excluding graphite and its carbon equivalent is listed in Table 3.

$$C_{Eq} = C_C + 0.4C_S + 0.33C_{Si} - 0.027C_{Mn} - 0.25C_{Cr} \quad (2)$$

Table 3. Composition of the alloy excluding graphite for the five graphitic white irons.

Alloys	Chemical Composition (wt.%)					Carbon Equivalent
	C	S (ppm)	Si	Mn	Cr	
3Cr	1.55	159	2.12	0.45	2.87	1.52
5Cr	2.50	161	2.05	0.48	5.23	1.86
7Cr	3.10	187	2.11	0.50	7.21	1.98
9Cr	3.60	198	2.05	0.50	9.08	2.00
11Cr	4.13	172	2.05	0.50	11.13	2.02

The thermal diffusivities of the alloy excluding graphite at various temperatures were then plotted against carbon equivalent (CE) of alloy excluding graphite, using the data in Table 3. As shown in Figure 13, the thermal diffusivity of the alloy excluding graphite follows a linear relation with the carbon equivalent of the alloy at each individual testing temperature. The linear equations fitted to the diffusivity-CE relationships are shown in Figure 13. Moreover, the slope of the linear equation increases and the constant of the linear equation decreases with increasing temperature (see data points in Figure 14). Second order polynomial equations were fitted to represent the relationships between linear equation slope and testing temperature, and between linear equation constant and testing temperature, respectively. Taking both CE of the alloy excluding graphite and the temperature into consideration, a comprehensive equation shown in Eq. 3 was developed and was used to calculate the thermal diffusivity

of each alloy matrix (excluding graphite) at any given temperature. As a result, the effective thermal diffusivity of any graphitic white iron can be determined by combining Eq. 2, Eq. 3 and the Hashin-Shtrikman model. This method can be potentially applied to other similar alloyed cast iron systems.

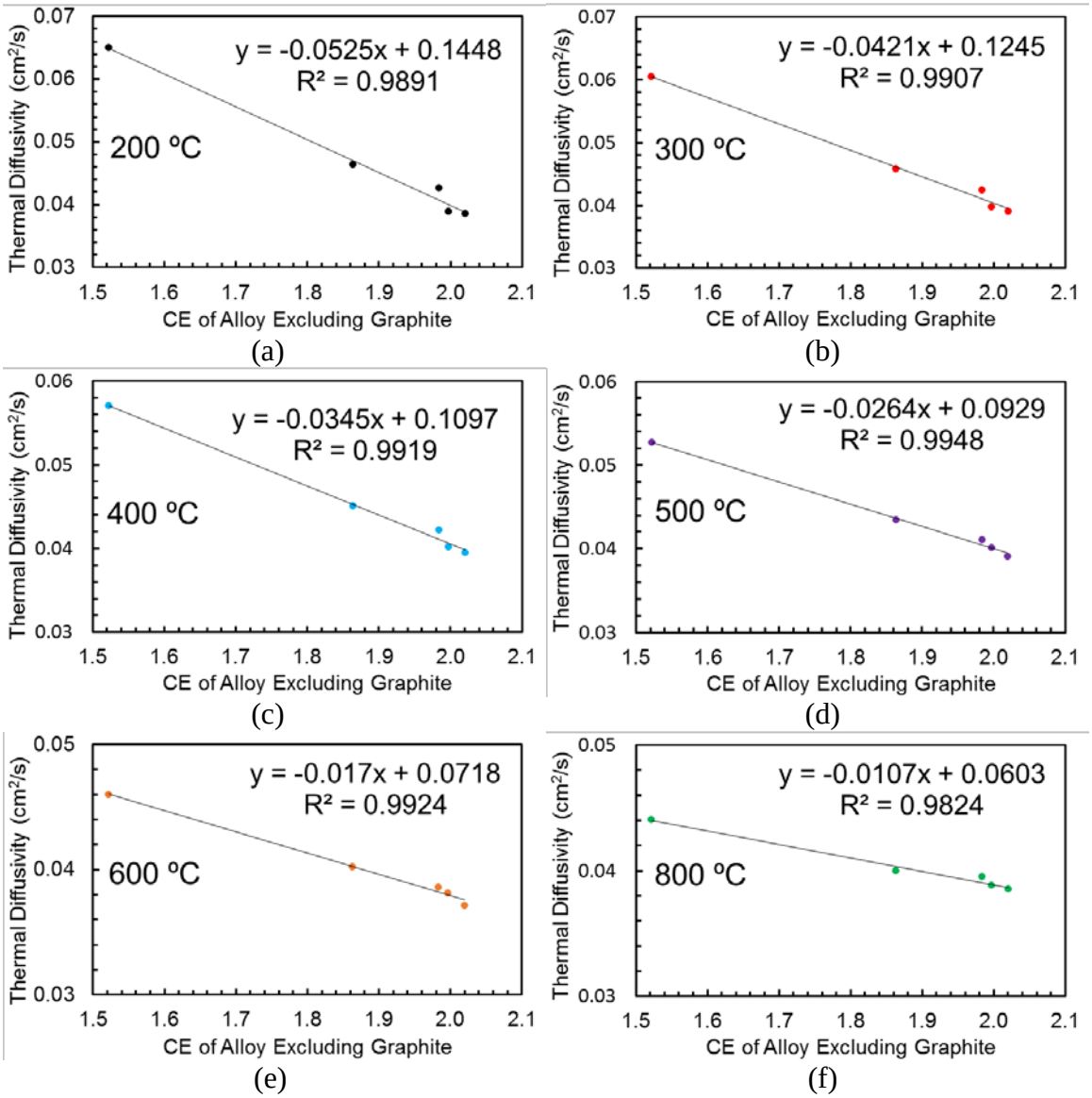

Figure 13. Plots of thermal diffusivity of the alloy excluding graphite against carbon equivalent of the alloy excluding graphite at temperatures of: (a) 200 °C; (b) 300 °C; (c) 400 °C; (d) 500 °C; (e) 600 °C; (f) 800 °C.

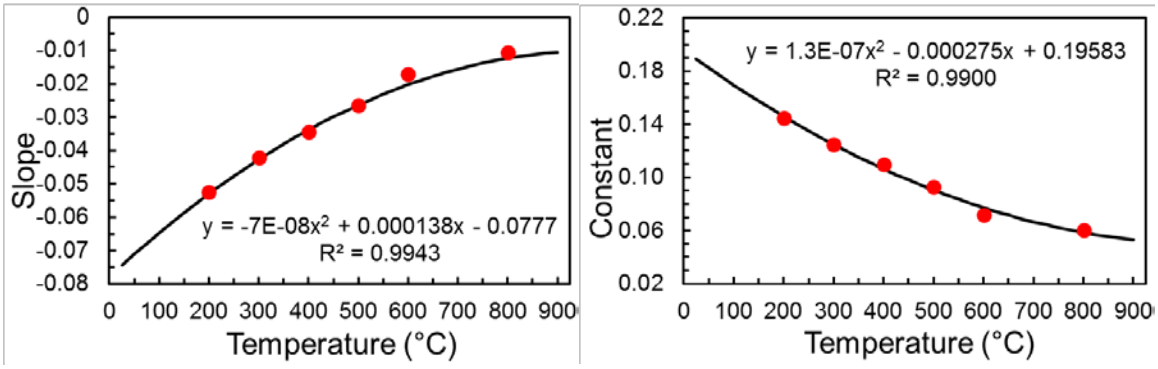

Figure 14. Plots showing the relationship between temperature and (a) slope of linear equations; (b) constant of linear equations shown in Figure 12. The dots represent the calculated slopes versus constants at the various testing temperatures.

$$dm = (-7 \times 10^{-8}T^2 + 1.38 \times 10^{-4}T - 0.0777)CE + (1.3 \times 10^{-7}T^2 - 2.75 \times 10^{-4}T + 0.19583) \quad (3)$$

where, d_m is the thermal diffusivity for the alloy excluding graphite, T is temperature in Celsius, CE is the carbon equivalent of the alloy excluding graphite.

4.2. WEAR RESISTANCE INVESTIGATION

Comparing the wear scars for various alloys in Figure 11, the wear mechanism is controlled by both removal of the hard phases and removal of the matrix. Tolfree [36] found that when the hardness of a material reaches a certain point, the wear resistance does not increase significantly any more. Instead, the controlling factor of a material's wear resistance becomes the removal of the hard phase and the toughness of the matrix. As a consequence, the harder M_7C_3 carbides provided a better wear resistance comparing to cementite. In addition, as shown in Figure 15, the hardness of M_7C_3 increases with the addition of Cr. This explains the improved wear resistant from alloy 3Cr to alloy 9Cr.

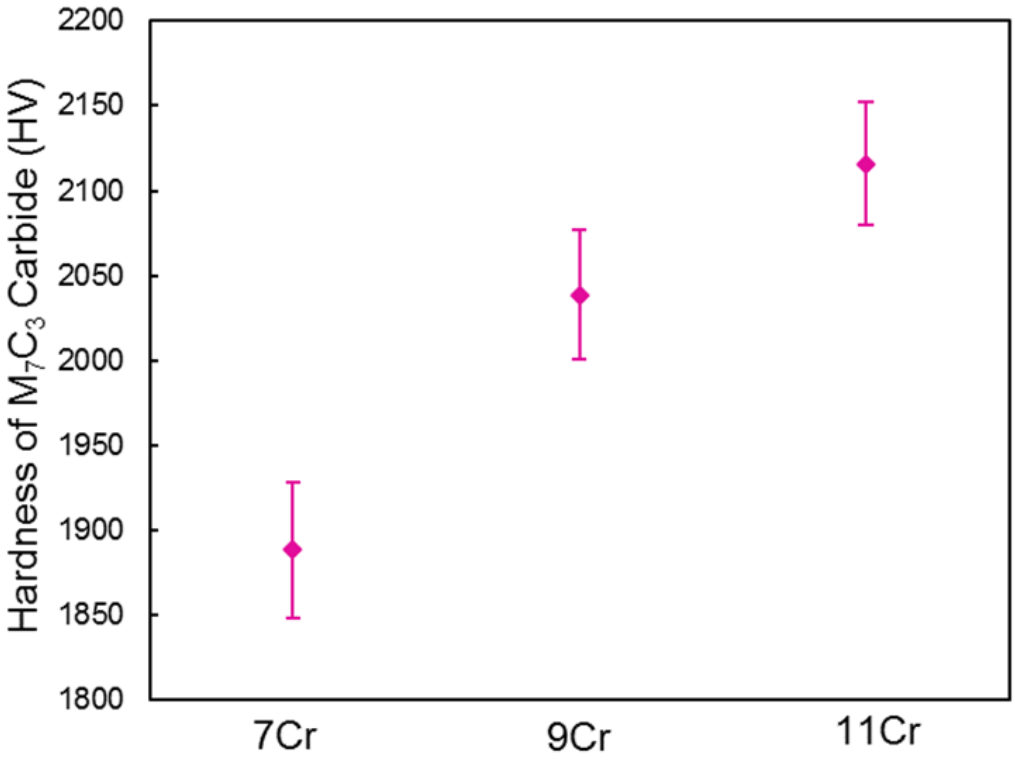

Figure 15. Vickers indentation hardness for M_7C_3 carbide in alloys 7Cr, 9Cr and 11Cr. Error bars represent a 95% CL for 10 measurements.

Another dominating wear mechanism in abrasive wear is the removal of softer metal matrix [37]. The additional plate cementite existing in the alloy 9Cr (compared to alloy 11Cr) served as a "buffer" for the matrix, which also slowed down the wear rate of matrix as M_7C_3 carbides is worn away. A phase map obtained using EBSD shown in Figure 16(a) indicates that alloy Fe15Mo19Cr contains a high fraction of M_6C. In contrast, the matrix of alloy 11Cr (Figure 16(b)) is primarily pearlite, including those around the graphite flakes and transformed from austenite, as well as those in the ledeburite structure. The EBSD does not have the resolution to differentiate the fine lamellar structure of cementite in the pearlite, and only the ferrite was captured and

indexed. The extra hardness provided by M_6C in alloy Fe15Mo19Cr made it more wear resistant.

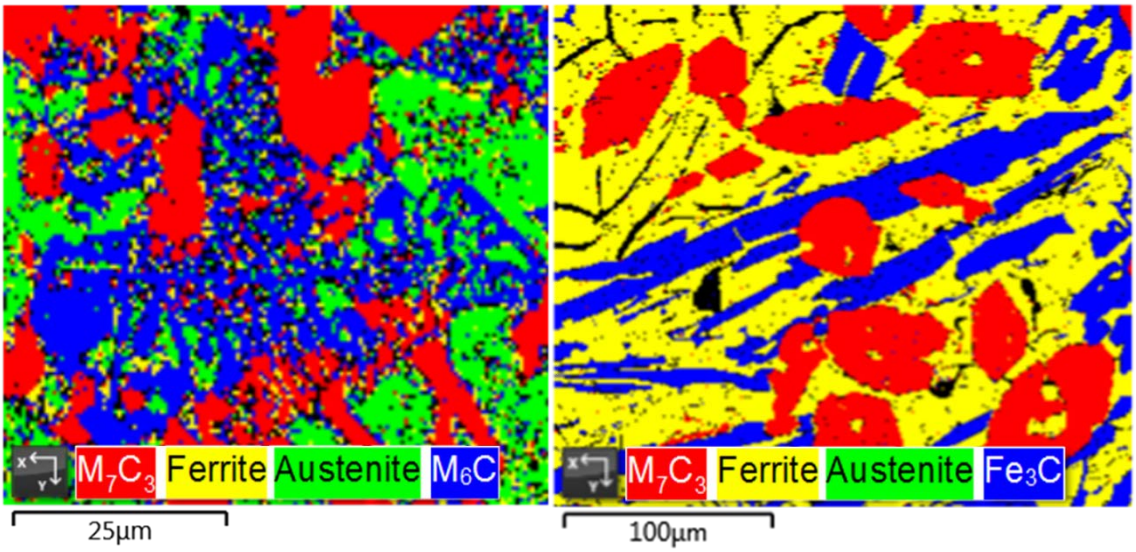

(a) (b)

Figure 16. EBSD phase mapping for alloys (a) Fe15Mo9Cr; (b) 9Cr.

Cr EDS (Energy Dispersive Spectroscopy) mappings were acquired on the wear surfaces of alloy 7Cr, 9Cr and 11Cr. As shown in Figure 17(a-c), M_7C_3 carbide has a higher Cr content, plate cementite has an intermediate Cr content, and all the additional matrix structures have the lowest Cr content. Carbide volume percent was then measured on the Cr EDS mappings by adjusting the contrast threshold to include only the M_7C_3 carbide and the plate cementite. The measured results are shown in Table 4. Although alloy 11Cr has the highest Cr content and the M_7C_3 has the highest hardness (>2100 HV), alloy 9Cr has a better wear resistance than alloy 11Cr since the carbide volume percent in alloy 11Cr is lower than that in alloy 7Cr and alloy 9Cr.

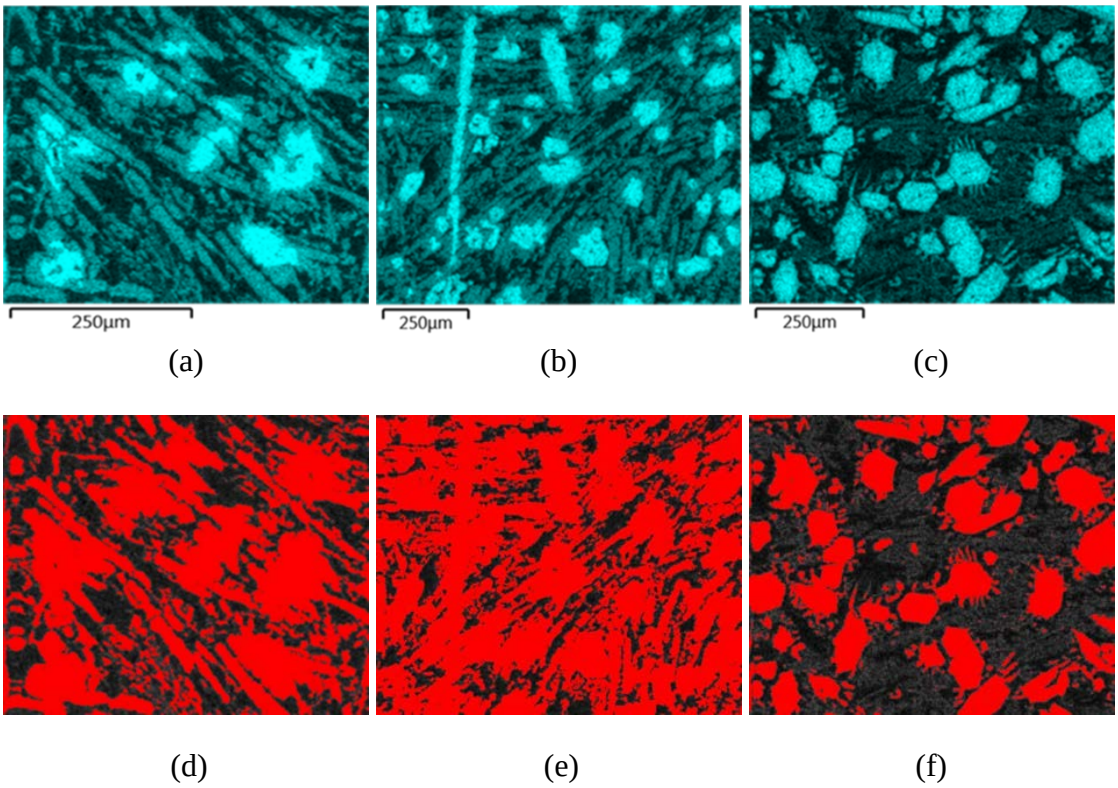

Figure 17. Cr EDS mapping for alloys 7Cr (a), 9Cr (b) and 11Cr (c); Contrast threshold adjusted to include carbidic phases in alloys 7Cr (d), 9Cr (e) and 11Cr (f).

Table 4. Exposed volume percent for carbides measured on the Cr EDS mapping acquired from the wear scars.

Alloy	7Cr	9Cr	11Cr
Carbide Volume Percent (vol.%)	58.73	70.92	35.49

4.3. WEAR PROPERTY MODEL

It is reported that there is a linear correlation between the volume loss and the hardness for the similar type of material [38-40]. As shown in Figure 18 (a), the developed graphitic white irons fall into the lower left side of the volume loss vs. hardness graph compared with the other two non-graphite-containing alloys. This indicates that graphitic white irons have a better wear resistance compared with non-

graphitic irons at equivalent hardness. To quantitatively study the graphite effect on the wear resistance, a graphite contribution factor was added as an independent variable. As shown in Figure 18 (b), volume loss determined from the wear test was plotted against the alloy hardness using the Rockwell C-scale and graphite volume percent. Data for seven studied alloys were fitted with a linear equation. This implies that introducing graphite flakes into white irons can reduce the wear rate. Namely, graphitic white irons have a better wear resistance compared with the non-graphite-containing irons of equivalent hardness. Quantitatively, 1 vol.% addition of graphite has the same effect as a 2.33 HRC increase in hardness with respect to the wear resistance. The empirical equation shown in Figure 18(b) can be used to calculate the volume loss of similar alloy with any given hardness and graphite volume percent in future study.

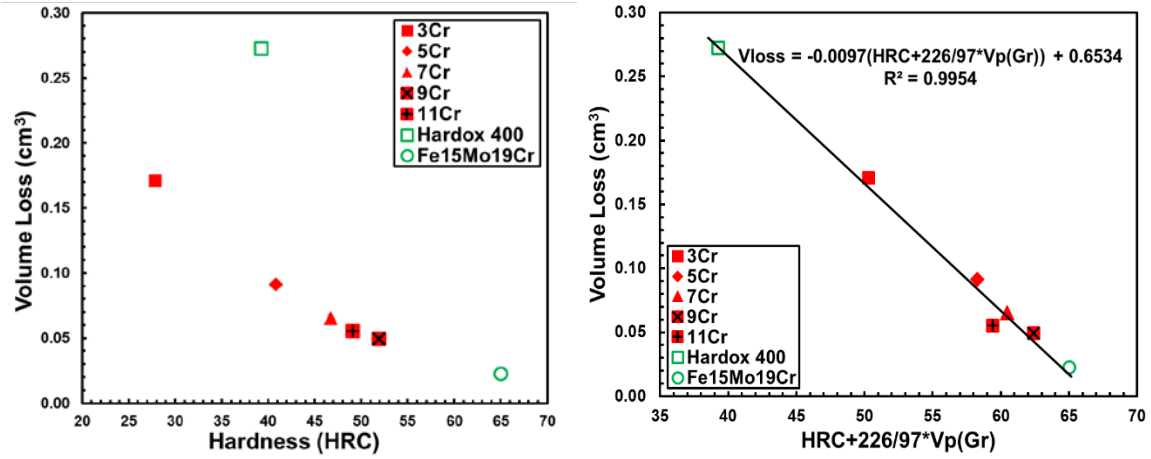

(a) (b)

Figure 18. Plots showing: (a) volume loss versus hardness of alloys studied; (b) volume loss as a function of alloy hardness and graphite volume percent.

4.4. RATIONAL FOR GRAPHITE CONTRIBUTION

Two possible mechanisms may play a role in the observed increase of wear resistance for white iron via the addition of graphite flakes. First, graphite addition increases the thermal diffusivity of the white irons as shown in Figure 9. Formation of the wear scar requires substantial plastic deformation and the flow stress decreases with increasing temperature. Thus, a reduced surface temperature during particle penetration may reduce the depth of penetration and increase the work of particle ploughing or cutting. Graphite may also become dispersed on the surface during abrasive wear which may contribute to particle sliding versus penetration and ploughing. Similar to graphite impregnated metal composites [41-44], the abraded and dispersed graphite particles on the wear scars work as a lubricant, which further slows down the wear rate. The optimal combination of graphite volume percent and graphite flake size may be studied in future work.

4.5. ALLOY COST

Cost is a key factor during material selection. To compare the alloy cost among the alloys studied, the scrap price for different ferrous alloy was acquired from InfoMine [45]. The unit price for each alloy was calculated based on chemistry. The alloy cost was plotted against its volume loss in Figure 19(b). Even though alloy Fe15Mo19Cr has the best wear performance, it is almost ten times more expensive as a result of the high Mo (15wt.%) and high Cr (19wt.%) concentrations as compared with the developed graphitic white irons. The 9Cr graphitic white iron gives the best combination of wear resistance and cost with wear resistance almost as good as the Fe15Mo19Cr iron while

having a cost comparable to Hardox 400. There still exists large potential to improve the wear performance for graphitic white iron. Future work will focus on improving the matrix hardness by adding alloy addition, in order to improve the wear performance of developed alloy.

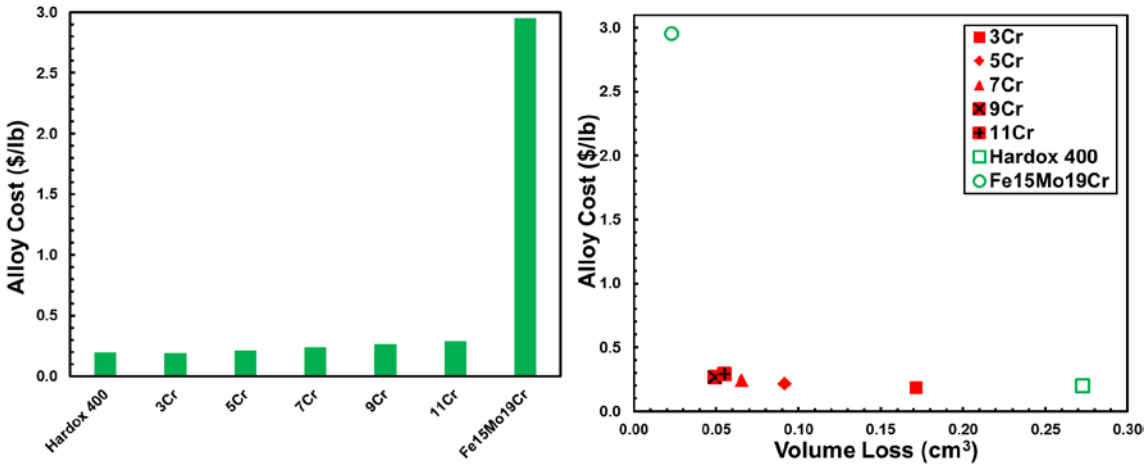

(a) (b)

Figure 19. Plots showing: (a) alloy cost comparison in dollar per pound for alloys studied; (b) alloy cost versus volume loss.

5. CONCLUSION

Five alloys have been designed, cast and investigated to develop the first generation of graphitic white iron, which shows premium thermal diffusivity and can potentially extend the lifetime of dissimilar metals contact wear systems. Abrasive wear tests showed that graphite had a positive effect on the wear performance within the 3-10 vol.% of graphite studied. The improved wear resistance of the graphite flake containing composites was related to improved thermal diffusivity. A numerical model taking both hardness and graphite volume percent into volume loss calculation was established.

Alloy cost comparison indicated that the alloy 9Cr graphitic white iron had a comparable wear resistance to a Fe15Mo19Cr white iron, but at a cost comparable to Hardox 400. Future work will focus on producing carbide networks through alloy additions, in order to improve the wear resistance.

ACKNOWLEDGEMENTS

This work was financially supported by Caterpillar Inc. The authors would like to thank James O. Barlow for providing the scrap price. Perrin W. Habecker is acknowledged for his assistance with the experiments and sample preparations. The FEI Helios NanoLab SEM was obtained with a Major Research Instrumentation grant from the National Science Foundation under contract DMR-0723128.

REFERENCES

[1] Annual Book of ASTM Standards, "ASTM Designation G40-17," *ASTM*, 2017.

[2] K. Kato, "Classification of Wear Mechanisms/Models," *Journal of Engineering Tribology,* vol. 216, no. J6, pp. 349-355, 2002.

[3] J. H. Tylczak and A. Oregon, "Abrasive Wear," in *ASM Handbook Volume 18*, ASM International, 1992, p. 184.

[4] M. F. Buchely, J. C. Gutierrez, L. M. Leon and A. Toro, "The Effect of Microstructure on Abrasive Wear of Hardfacing Alloys," *Wear,* vol. 259, pp. 52-61, 2005.

[5] M. Shah and S. D. Bakshi, "Three-body Abrasive Wear of Carbide-free Banite, Martensite and Banite-martensite Structure of Similar Hardness," *Wear,* vol. 402, pp. 207-215, 2018.

[6] S. A. Buckholz, D. C. Van Aken and L. N. Bartlett, "On the Influence of Aluminum and Carbon on Abrasion Resistance of High Manganese Steels," *AFS Transaction,* pp. 495-509, 2013.

[7] W. Molnar, A. Nevosad, H. Rojacz, K. Adam, H. J. Henze, M. R. Ripoll, and E. Badisch, "Two and three-body abrasion resistance of rubbers at elevated temperatures," *Wear,* Vols. 414-415, pp. 174-181, 2018.

[8] H. Rojacz, H. Pahr, S. Baumgartner, and M. Varga, "High temperature abrasion resistance of differently welded structural steels," *Tribology International,* vol. 113, pp. 487-499, 2017.

[9] H. Torres, M. Varga, M. R. Ripoll, "High temperature hardness of steels and iron-based alloys," *Materials Science and Engineering: A,* vol. 671, pp. 170-181, 2016.

[10] H. Berns and W. Theisen, "Tribological Properties," in *Ferrous Materials,* Bochum, Springer, 2008, p. 103.

[11] P. E. Belyakova, M. E. Garber, and E. V. Rozhkova, "Physical properties of white chromium cast irons," *Metal Science and Heat Treatment,* vol. 17, no. 12, pp. 1041-1044, 1975.

[12] S. Natarajan, E. Anand, K. S. Akhilesh, A. Rajagopal, and P. P. Nambiar, "Effect of graphite addition on the microstructure, hardness and abrasive wear behavior of plasma sprayed NiCrBSi coatings," *Materials Chemistry and Physics,* vol. 175, pp. 100-106, 2016.

[13] J. Krawczyk and J. Pacyna, "Effect of the Cooling Rate on the Mottled Cast Iron Microstructure Designed for the Mill Rolls," *Metallurgy and Foundry Engineering,* vol. 35, no. 2, pp. 101-110, 2009.

[14] J. Krawczyk and J. Pacyna, "The Influence of Microstructure of Mottled Cast Iron for Mill Rolls on its Properties," *18th International Conference on Metallurgy and Materials,* pp. 266-272, 2009.

[15] J. Krawczyk and J. Pacyna, "Influence of a Matrix on Properties of Mottled Cast Iron Applied for Mill Rolls," *Archives of Foundry Engineering,* vol. 10, no. 3, pp. 45-50, 2010.

[16] J. J. Coronado, A. Gomez and A. Sinatora, "Tempering Temperature Effects on Abrasive Wear of Mottled Cast Iron," *Wear,* vol. 267, pp. 2070-2076, 2009.

[17] J. J. Coronado and A. Sinatora, "Particle Size Effect on Abrasion Resistance of Mottled Cast Iron with Different Retained Austenite Contents," *Wear,* vol. 267, pp. 2077-2082, 2009.

[18] J. J. Coronado, S. A. Rodriguez, C. E. K. Mady and A. Sinatora, "Mechinical Properties of Cementite in Mottled Cast Iron," in *ABRASION2008,* Trento, 2008.

[19] T. Matsushita, A. G. Saro, L. Elmquist and A. W. Jarfors, "On the Specific Heat and Thermal Diffusivity of CGI and SGI Cast Irons," *International Journal of Cast Metals Research,* vol. 30, pp. 276-282, 2017.

[20] J. Wan, J. Qing and M. Xu, "Designing a Novel Graphitic White Iron for Metal-to-metal Wear Systems," *Metallurgical and Materials Transactions A,* vol. 50, no. 3, pp. 1162-1174, 2019.

[21] J. Wan, J. Qing and M. Xu, "Developing a Graphitic White Cast Iron," in *Materials Science and Technology 2018,* Columbus, 2018.

[22] J. Wan, P. W. Habecker, J. Qing and M. Xu, "Evolution of Phases in a Graphitic White Iron," *AFS Trasaction,* 2019.

[23] Annual Book of ASTM Standards, "ASTM Designation E92-17," *ASTM,* 2017.

[24] Annual Book of ASTM Standards, "ASTM Designation E1461-13," *ASTM,* 2013.

[25] K. Shinzato and T. Babe, "A Laser Flash Apparatus for Thermal Diffusivity and Specific Heat Capacity Measurements," *Journal of Thermal Analysis and Calorimetry,* vol. 64, no. 1, pp. 413-422, 2001.

[26] M. Kover, M. Behulova, M. Drienovsky and P. Motycka, "Determination of the Specific Heat Using Laser Flash Apparatus," *Journal of Thermal Analysis and Calorimetry,* vol. 122, no. 1, pp. 151-156, 2015.

[27] Annual Book of ASTM Standards, "ASTM Designation G65-16," *ASTM,* 2016.

[28] D. C. Van Aken and W. F. Hosford, "Reporting Results: A Practical Guide for Engineers and Scientists," Cambridge University, 2008, pp. 87-91.

[29] A. Salazar, "On Thermal Diffusivity," *European Hournal of Physics,* vol. 24, no. 4, pp. 351-358, 2003.

[30] Z. Hashin, "Analysis of Composite Materials- A Survey," *Journal of Applied Mechanics,* vol. 50, no. 3, pp. 481-505, 1983.

[31] A. Salazar, A. Sanchez-Lavega and J. M. Terron, "Effective Thermal Diffusivity of Layered Materials Measured by Modulated Photothermal Techniques," *Journal of Applied Physics,* vol. 84, no. 6, pp. 3031-3041, 1998.

[32] A. Salazar, J. M. Terron, A. Sanchez-Lavega and R. Celorrio, "On the Effective Thermal Diffusivity of Fiber-reinforced Composites," *Applied Physics Letters,* vol. 80, no. 11, pp. 1903-1905, 2002.

[33] J. R. Thomas, JR. and D. P. H. Hasselman, "Effective Thermal Conductivity of Continuous Matrix-spherical Dispersed Phase Composite with Single-point Interfacial Thermal Contact: Free Molecular Gas Conduction in the Gas," *Journal of Composite Materials,* vol. 41, no. 3, pp. 267-279, 2007.

[34] K. Das, S. M. Kamaruzzaman, T. R. Middya and S. Datta, "Thermal diffusivity of Advanced Composite Materials of e-glass Fiber Reinforced Plastic in the Temperature Range 5-12K," *Indian Journal of Pure & Applied Physics,* vol. 47, pp. 273-276, 2009.

[35] K. Pietrak and T. S. Wisniewski, "A Review of Models for Effective Thermal Conductivity of Composite Materials," *Journal of Powder Technologies,* vol. 95, no. 1, pp. 14-24, 2015.

[36] D. Tolfree, "Investigation of the Gouging Abrasion Resistance of Materials in the Mining Industry," McGill University, 2000.

[37] P. Kulu, R. Tarbe, A. Zikin, H. Sarjas and A. Surzenkov, "Abrasive Wear Resistance of Recycled Hardmetal Reinforced Thick Coating," *Key Engineering Materials,* vol. 527, pp. 185-190, 2013.

[38] K. Hokkirigawa, K. Kato and Z. Z. Li, "The Effect of Hardness on the Transition of the Abrasive Wear Mechanism of Steels," *Wear,* vol. 123, pp. 241-251, 1988.

[39] J. A. Hawk, R. D. Wilson, J. H. Tylczak and O. N. Dogan, "Laboratory Abrasive Wear Tests: Investigation of Test Methods and Alloy Correlation," *Wear,* vol. 225, pp. 1031-1042, 1999.

[40] J. H. Tylczak, J. A. Hawk and R. D. Wilson, "A Comparison of Laboratory Abrasion and Field Wear Results," *Wear,* vol. 225, pp. 1029-1069, 1999.

[41] R. Kumar and T. S. Sudarshan, "Self-Lubricating Composites: Graphite-Copper," *Materials Technology,* vol. 11, no. 5, pp. 191-194, 1996.

[42] H. Goto and K. Uchijo, "Wear Mechanism of Al-Si Alloy Impregnated Graphite Composite under Dry Sliding," *Wear,* vol. 259, no. 1-6, pp. 613-619, 2005.

[43] H. Goto and S. Omori, "Friction and Wear Characterisitics of Aluminum Alloy Impregnated Carbon Composite," *Journal of Tribology,* vol. 121, no. 2, pp. 294-300, 1999.

[44] H. Goto, S. Omori and K. Uchijo , "Wear Behaviro of Al-Si Alloy Impregnated Graphite Composite," *Tribology Transactions,* vol. 44, no. 4, p. 551, 2001.

[45] J. O. Barlow, *Personal communication,* Peoria, 2018.

IV. ADHESIVE WEAR PROPERTY OF A GRAPHITIC WHITE IRON DESIGNED FOR METAL-TO-METAL WEAR SYSTEMS

Jie Wan[1], David C. Van Aken[1], Jingjing Qing[2], Mingzhi Xu[2]

[1]Missouri University of Science and Technology, Rolla, MO 65401, USA

[2]Georgia Southern University, Statesboro, GA 30460, USA

Tel: 573-578-3874

Email: jwvt7@mst.edu

Keywords: Graphitic White Iron, Graphite Effect, Block On Ring Test, Adhesive Wear, Empirical Model

ABSTRACT

Five chromium white iron composites were cast containing graphite between 3 and 10 volume percent. Chromium content was varied between 3 and 11 wt.% to change the primary solidification from graphite to M7C3 and graphite content decreased to 3 volume percent. Adhesive wear resistance was assessed with a block on ring apparatus in accordance with ASTM G77. Hardness and adhesive wear resistance increased with chromium content and the most wear resistant alloy (9wt.%Cr) had a microstructure containing both M7C3 carbides and graphite (4.6 vol.%). An empirical model was formulated to quantitatively evaluate graphite additions on the adhesive wear resistance, which indicated that 1 vol.% graphite addition had the same effect as a hardness increase of 2.66 HRC. The improved wear resistance was related to an increased thermal diffusivity of the composite microstructure and the surface lubricating effect of graphite.

1. INTRODUCTION

Metal-to-metal wear systems are common in rotating machinery [1], [2], [3]. The cost of repair and replacement of these parts and the associated downtime related to these activities is a significant cost to the industry [4]. It has been estimated that the economic cost of wear ranges from 1% to 4% of the gross national product for an industrialized nation. Various hard facing materials have been designed for such applications, such as silicon carbide, tungsten carbide, Ni-Resist cast iron, Stellite, and aluminum oxide in order to slow down the wear rate and extend the service life [3], [5], [6], [7]. However, all of these hard facing materials are either too expensive or too brittle to be widely used in metal-to-metal wear systems [8].

A cast version of a hard facing material has been investigated by the authors, which was termed as Fe15Mo18Cr based on its nominal composition [9]. Failure analysis showed that a brittle white layer was formed on the wearing surface. Similar observations of white layer formation have been associated with adhesive wear failures [10], [11], [12], [13]. Typically, a white layer is a result of excessive heat generated during adhesive wear for metal-to-metal surface contact under high contact pressure.

A potential solution to deal with frictional heating is to increase thermal diffusivity by composite engineering. In a previous study by the authors, flake graphite was introduced by inoculation when casting a chromium alloyed white iron [14]. These new composite alloys combined the advantages of both high wear resistant M7C3 carbides [15], [16], [17] and high thermal diffusivity of flake graphite [18], [19], [20], [21], [8]. Thermal diffusivity and abrasive wear performance for these graphitic white

irons have been reported elsewhere, but are briefly reviewed below for the readers' convenience [22].

1.1. THERMAL DIFFUSIVITY

Thermal diffusivity was measured using a laser flash method following ASTM E1461 [23]. As shown in Figure 1, thermal diffusivity of the graphitic white iron increased with increasing graphite volume percent and decreased with increasing test temperature.

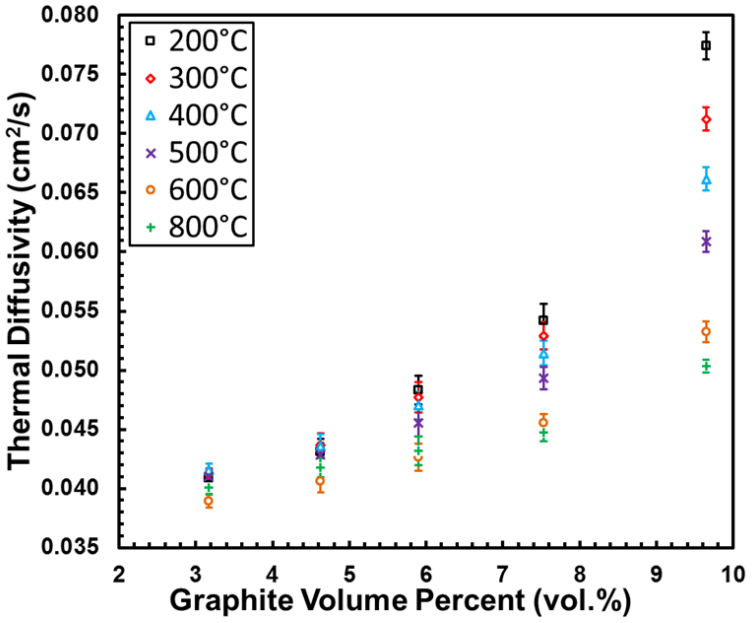

Figure 1. Measurements showing that a higher graphite volume percent improves the thermal diffusivity of the alloy at every testing temperature. Error bars represent a 95% CL [22].

1.2. ABRASIVE WEAR

Abrasive wear resistance was evaluated utilizing a dry sand/rubber wheel apparatus following ASTM G65 [24]. Hardox 400 and a cast hard facing alloy

(designated Fe15Mo19Cr) were also tested to provide a standard for comparison. In general, the abrasive wear resistance of the chromium white irons increased as the hardness increased, as shown in Figure 2(a). An empirical model was established, where the volume percent of graphite was fit to the volume loss data, and graphite addition was found to be beneficial with respect to abrasive wear, as shown in Figure 2(b). Quantitatively, 1 vol.% addition of graphite has the same effect as a 2.33 HRC increase in hardness with respect to the wear resistance. In conclusion, the graphitic white irons developed have a better abrasive wear resistance compared with regular non-graphite-containing irons of equivalent hardness.

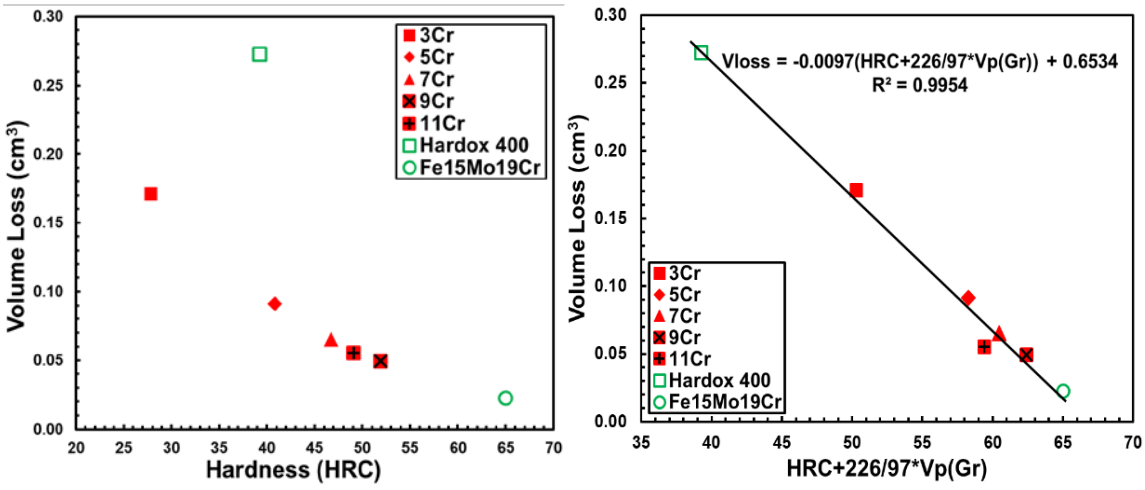

(a) (b)

Figure 2. Plots showing: (a) volume loss versus hardness of alloys studied; (b) volume loss as a function of alloy hardness and graphite volume percent [22].

Thermal diffusivity is expected to play a more important role in adhesive wear resistance, since local heating or flash temperatures can be as high as 1000°C [25]. In the present investigation, the adhesive wear performance of these first generation of graphitic white irons have been studied using an ASTM G77 block on ring test. The adhesive wear

mechanism was studied by means of optical microscopy and scanning electron microscopy.

2. MATERIALS AND METHODS

2.1. MATERIALS

Thermodynamic and microstructural analyses of the five chromium white irons has been presented elsewhere [22], [14]. The five chromium compositions ranging from 3 to 11 wt.% chromium produce primary graphite at low chromium concentrations and primary M7C3 carbide at higher chromium concentrations. In general, the hardness increases and the volume fraction of graphite decreases with increasing chromium content. Alloys were induction melted using high purity charge materials and cast in no-bake sand molds. An inoculant (0.15wt.%) was added into each alloy to promote the formation of graphite. The chemical compositions were analyzed using an optical emission spectrometer and Leco combustion C/S analyzer, as listed in Table 1. The five alloys produced are designated as 3Cr, 5Cr, 7Cr, 9Cr and 11Cr, based on their approximate Cr content.

Table 1. Chemical compositions of the five alloys analyzed using an optical emission spectrometer and a Leco combustion C/S analyzer.

Alloys	Chemical composition (wt.%)				
	Leco C	Leco S (ppm)	Si	Mn	Cr
3Cr	4.45	154	2.06	0.44	2.79
5Cr	4.72	157	2.00	0.47	5.11
7Cr	4.88	184	2.07	0.49	7.08
9Cr	4.93	198	2.05	0.50	9.08
11Cr	5.00	170	2.03	0.50	11.03

2.2. SAMPLE PREPARATION AND CHARACTERIZATION

2.2.1. Metallographic Samples. Metallographic specimens were prepared with silicon carbide papers from 180 to 1200 grit, followed by polishing using diamond pastes from 3 μm to 0.1 μm. The specimens were ultrasonically cleaned between each step. The first set of specimens were observed in an as-polished state to measure graphite volume percent and study the graphite morphology to determine when the graphite formed during solidification. The second set of specimens were etched with 2% nital to observe different carbides as well as the matrix microstructure. Images were recorded using a Nikon FX-35DX camera.

2.2.2. Block On Ring Samples. A block on ring (BOR) apparatus was utilized to study the adhesive wear performance of each alloy in accordance with ASTM G77 [26]. In addition to the five graphitic white irons, a cast Fe15Mo19Cr alloy was also tested for comparison. The Fe15Mo19Cr was originally used as a hardfacing alloy, but can also be cast directly to form a premium wear-resistant white iron, which can be used in metal-to-metal wear applications. Three block specimens were prepared for each alloy with dimensions of 6.35mm x 10.16mm x 15.75mm. A fresh standard carburized 4620 steel Falex ring was used for each test to minimize the ring effect during the test. Hardness of the rings was measured to be 60±2 HRC. The test was run with a portion of the rotating ring submerged into lubricant to mimic a lubricated metal-to-metal wear system. Each test was conducted for one hour at a constant load of 300 lbf (1334 N) and a constant speed of 400 rpm (42 m/s). After testing, the average scar width was calculated based upon the measured area of the block wear scar. Volume loss was determined according to ASTM G77 Table I using the measured average width of the block wear scar [26].

Wear scars for each alloy were then evaluated by means of optical microscope and SEM to investigate the adhesive wear mechanisms. Operating parameters for the scanning electron microscope (SEM) consisted of an accelerating voltage of 20.0 kV and an emission current of 1.4 nA during image acquisition.

3. RESULTS

3.1. MICROSTRUCTURE

Figure 3 shows the as-polished microstructure, and Figure 4 shows the Nital etched microstructure. Low Cr alloys produced primary graphite (type A and type C), whereas higher Cr alloys exhibited primary M7C3 with eutectic graphite (type D). As is indicated in Figure 3 and Figure 4, three types of graphite (A, C, and D) and two types of carbide (M3C and M7C3) can be observed. The graphite addition is 9.64, 7.53, 5.90, 4.63, and 3.17 vol.% for alloy 3Cr, 5Cr, 7Cr, 9Cr and 11Cr, respectively. Detailed graphite volume percent measurement and phase characterization procedures can be accessed from authors' previously published work [14].

3.2. ADHESIVE WEAR PERFORMANCE

Volume loss measurements are reported in Figure 5 for the BOR tests, with error bars representing a 95% CL [27]. The hardness for each alloy is also labeled in Figure 5. A lower volume loss reflects better wear resistance. Alloy Fe15Mo19Cr showed the best wear resistance due to its high hardness, as it is even harder than the standard Falex ring (65 HRC vs. 60 HRC).

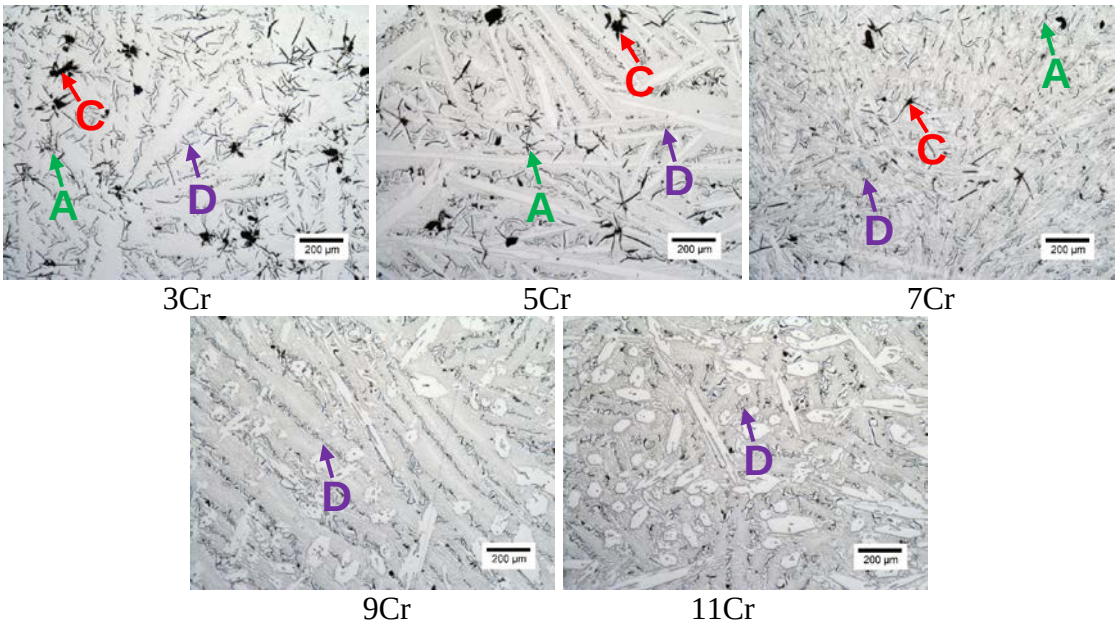

Figure 3. As-polished microstructures for five alloys studied. Three types of graphite can be observed, and are indicated by arrows with a letter in the end.

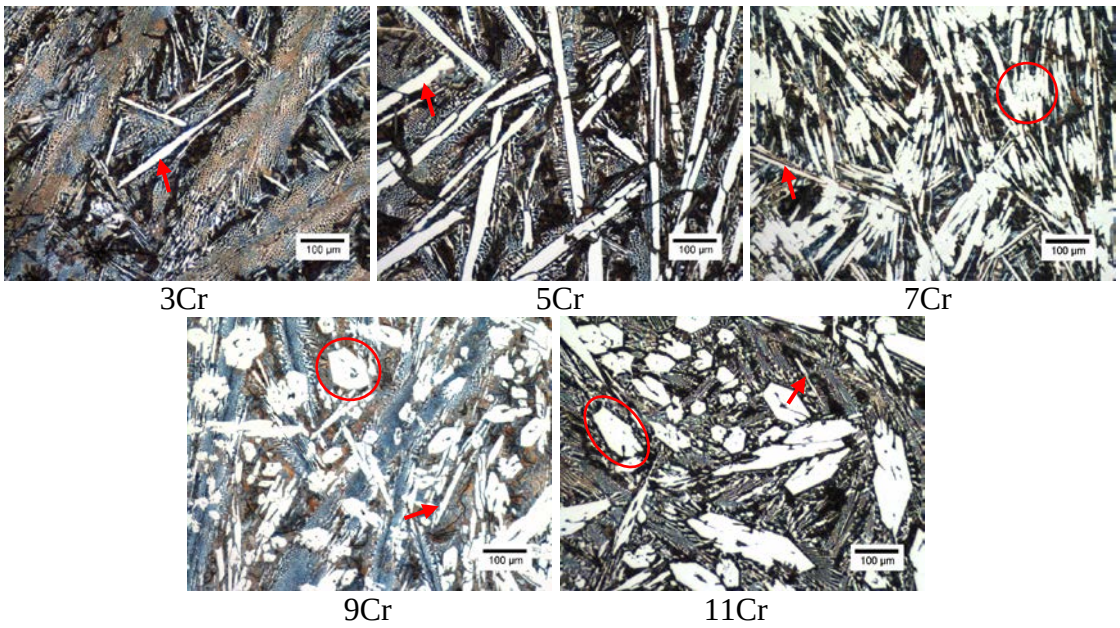

Figure 4. Nital etched microstructures for five alloys studied. Arrows indicate plate cementite (M3C), and circles indicate M7C3 carbide.

However, alloy 7Cr showed a better wear resistance than alloy 11Cr, even though it is softer than alloy 11Cr, which indicates that hardness was not the only controlling factors for the adhesive wear resistance. Within the five graphitic white irons developed, alloy 9Cr showed the best wear resistance.

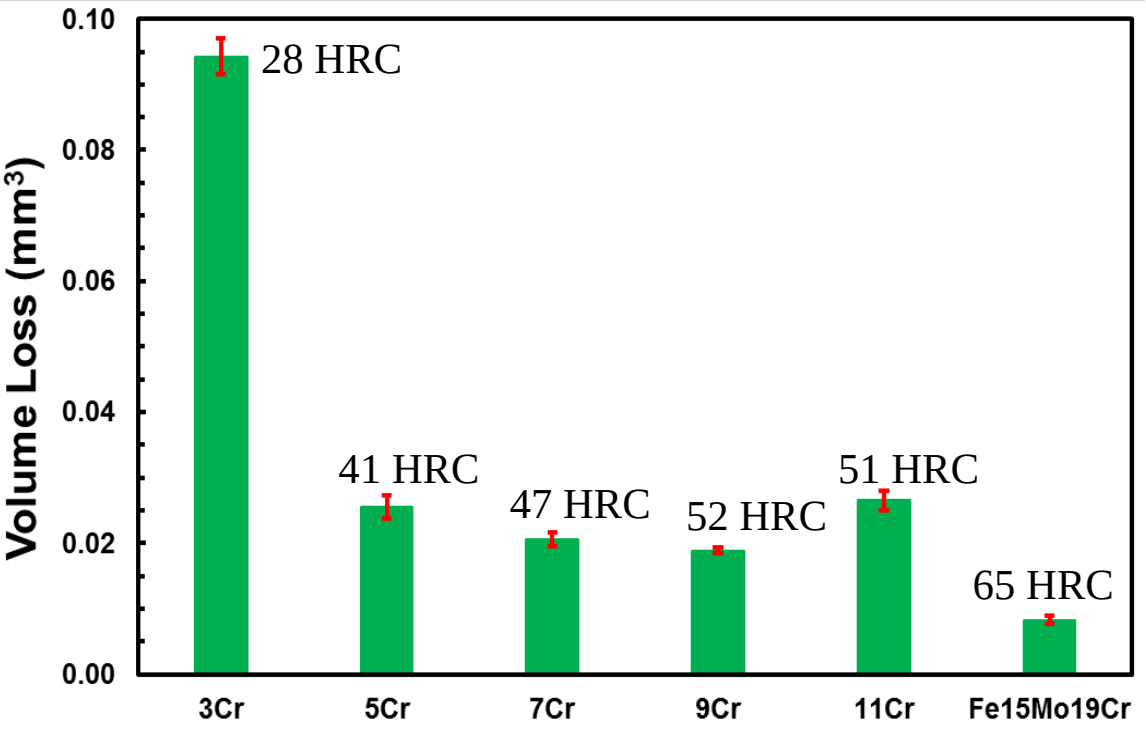

Figure 5. BOR volume loss of the graphitic white irons studied compared to alloy Fe15Mo19Cr. Error bars represent a 95% CL. Hardness for each alloy is labeled in Rockwell C scale.

3.3. ADHESIVE WEAR SCAR EVALUATION

The BOR wear scars were evaluated by means of SEM. As shown in Figure 6, three characteristics for adhesive wear can be observed including: material pulled out (indicated by arrows with straight end), material attachment (indicated by arrows with rhomb end), and material deformation (indicated by arrows with round end). In addition,

there was no direct evidence of abrasive wear like cutting or ploughing can be observed. It should be noted that the vertical lines on the wear scars are more likely a result of combination effect from ring surface roughness and plastic deformation. Therefore, abrasive wear was minimized in the BOR test, and this test result can represent adhesive wear resistance.

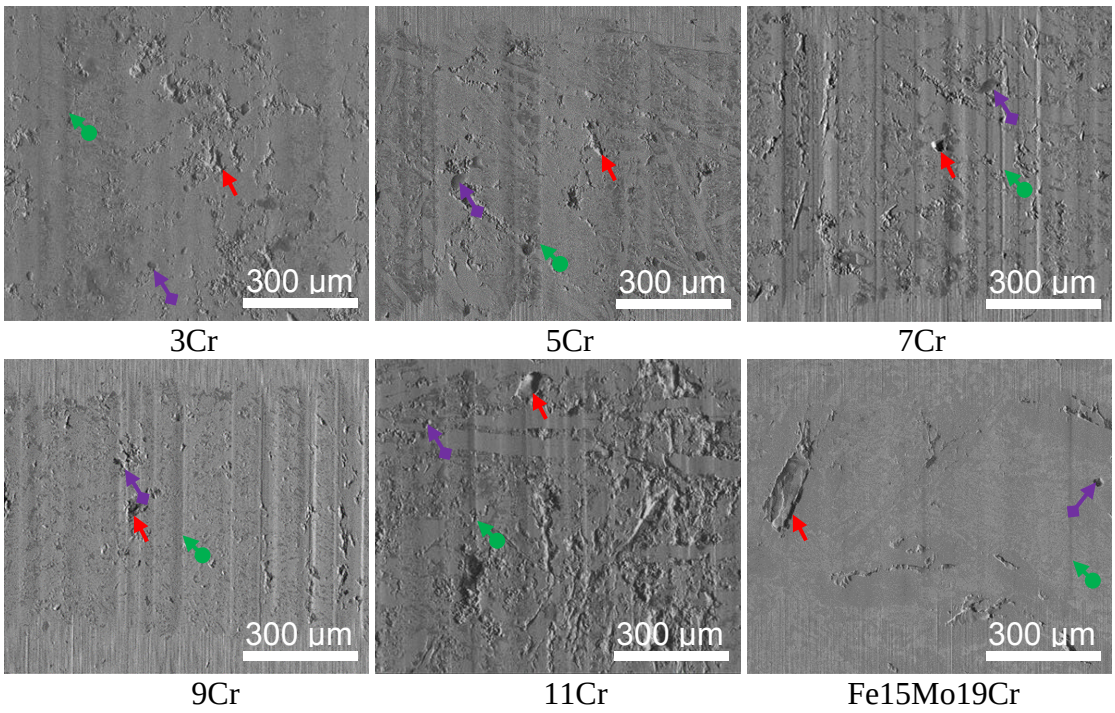

Figure 6. SEM secondary electron images showing the BOR wear scars for all five graphitic white irons studied as well as alloy Fe15Mo19Cr. Arrows with straight end indicate material pulled out, arrows with rhomb end indicate material attachment, and arrows with round end indicate material deformation.

Furthermore, high magnification SEM images on the material pulled out areas clearly revealed an adhesive wear mechanism, as shown in Figure 7. Solid arrows indicate crack initiation sites, and dashed arrows indicate the stepped crack propagation along the slip planes. As block surface and ring surface were pressed against each other

during the test, the adhesive bonding strength on the contact interface resisted relative sliding between the block and the ring. A large enough resistance relative to sliding created plastic deformation followed by shearing along slip planes. The slip initiated crack underneath the contact interface (solid arrows), which then propagated along the slip planes (dashed arrows). Taking the above mentioned into consideration, the performed BOR test was predominately an adhesive wear test and the results shown in Figure 5 can be used exclusively to assess the adhesive wear resistance.

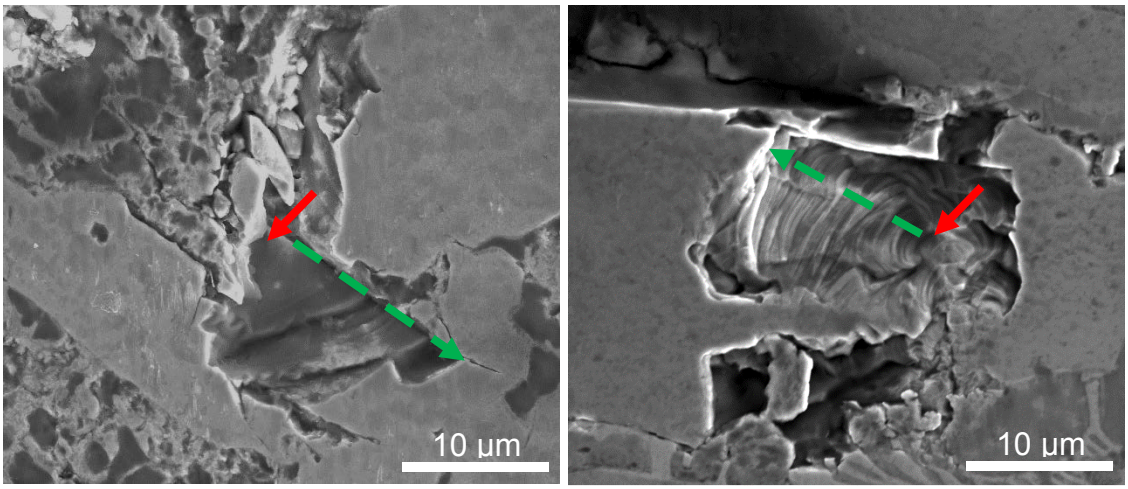

(a) (b)

Figure 7. SEM secondary electron image showing the BOR wear scar for: (a) alloy 9Cr; (b) alloy Fe15Mo19Cr. Adhesive wear mechanism is revealed by the material pulled out area. Solid arrows indicate crack initiation sites, and dashed arrows indicate the stepped crack propagation along the slip planes.

Figure 8(a) shows another high magnification SEM picture taken from the wear scar of alloy Fe15Mo19Cr, and Figure 8(b) is an optical micrograph showing its corresponding original microstructure taken from an as-polished metallographic sample via differential interference contrast (DIC) technique. A lot of fishbone carbides can be observed in both images. According to authors' pervious EBSD analysis, those fishbone

carbides are M6C carbides with Mo as the predominant metallic element. This eutectic M6C carbide worked as wear scare “stopper” or “buffer” in alloy Fe15Mo19Cr and decreased the wear rate during dry sand/rubber wheel abrasive wear test [22].

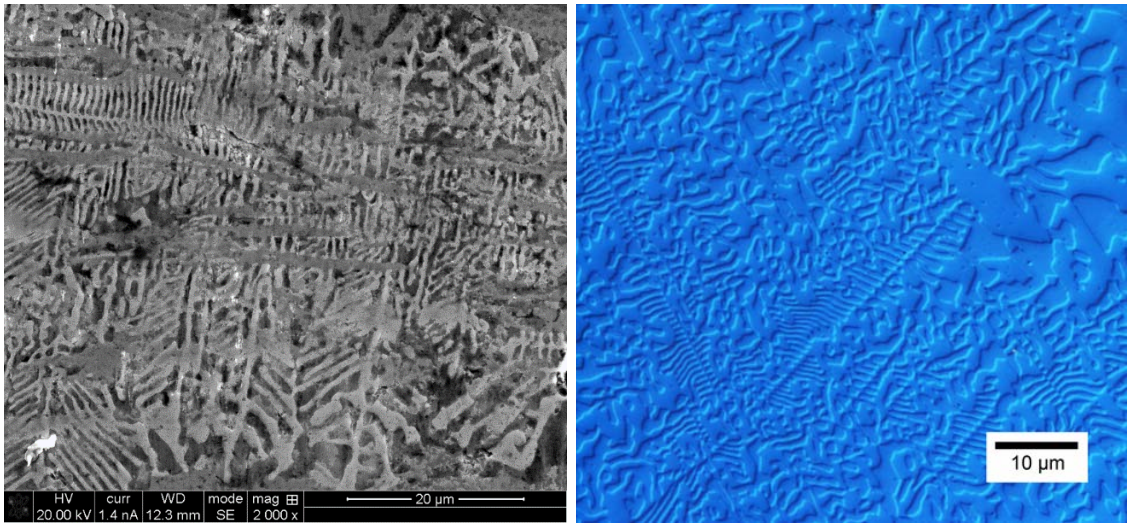

(a) (b)

Figure 8. Pictures for alloy Fe15Mo19Cr showing: (a) SEM image taken from BOR wear scar; (b) DIC image of the as-polished microstructure.

4. DISCUSSION

4.1. ADHESIVE WEAR RESISTANCE

Generally, adhesive wear resistance increases with increasing hardness [28], [29]. Therefore, alloy Fe15Mo19Cr showed the best adhesive wear resistance, as it is harder than other alloys including the standard Falex ring used as a counterbody. In work by Buchely et al. on the wear resistance of hard facing alloys [30], it was described that the M6C fishbone carbide is a tough phase that could withstand extensive plastic deformation without cracking and in turn enhance the material’s wear resistance.

Within the five graphitic white irons studied, the overall wear resistance increased with increasing hardness, as shown in Figure 5. However, alloy 5Cr showed a similar wear resistance with alloy 11Cr, and 7Cr showed a better wear resistance than alloy 11Cr, even though they are softer than alloy 11Cr by 10 HRC and 4HRC, respectively. Thus, hardness was not the only controlling factor for the adhesive wear resistance. Also, as shown in Figure 6, the amount of material pulled out from the contact interface seemed to increase with decreasing the graphite addition in the bulk material, which is especially severe in alloy 11Cr. This again indicated graphite phases were helpful in terms of reducing the severity of adhesive wear. However, as a phase of pure carbon, too much graphite depleted carbon from other portion of the material. This led to fewer carbides (Figure 4) and lower hardness (Figure 5). Therefore, the severity of plastic deformation appeared to increase with decreasing the graphite volume percent in the material, as shown in Figure 6. It should be noted that the appearance of the wear scar only reflects the last several paths of the test, and may not be directly related to the wear resistance. Width and depth of wear scar, and volume loss should be used as the primary justifications for the overall wear resistance.

High Cr content promotes the formation of hard M7C3 carbide [15], [14]. As shown in Figure 7(a), the pullout of M7C3 is not a benefit to the wear resistance. It's worth noting that the density of slip planes in Figure 7(b) is much higher than in Figure 7(a), which is due to the crystal structure difference. The pullout phases in Figure 7(a) and Figure 7(b) appear to be M7C3, and austenite, respectively. M7C3 has a hexagonal crystal structure, while austenite shows a FCC crystal structure. There are more slip systems in FCC than in hexagonal structure. It is also worth noting that the plastic

behavior of M7C3 has always been ignored due to its high hardness and lack of slip systems [15], [14], [16], [17]. However, many researchers found the plastic deformation behavior of M7C3 [31], [32], [33], [34]. The fracture behavior above the pullout area in Figure 7(a) could be resulted from the post cracking deformation.

4.2. ADHESIVE WEAR MODEL

A lot of numerical models have been developed to quantitatively study the adhesive wear resistance for different materials [35], [36], [37], [38]. However, most of those models are associated with complicated local asperity contacts area calculation, which makes them impractical. One of the most popular and practical models for adhesive wear is Archard equation [39], as shown in Eq. 1.

$$V = \frac{K}{3} \times \frac{WL}{H} \tag{1}$$

where, V is the adhesive wear volume loss, K is the non-dimensional parameter, W is the normal load, L is the sliding distance, and H is the material's hardness.

As a constant normal load and a constant test duration (sliding distance) were used for each test, the parameters "W" and "L" should be constant. Therefore, to quantitatively study the adhesive wear resistance, volume loss was plotted against 1/hardness, as shown in Figure 9(a). The data seemed to scatter around in the graph instead of falling into a linear line. A linear fit showed that there is a strong correlation between volume loss and hardness. However, the dispersion is unneglectable, which can be reduced and optimized by adding a graphite contribution factor into the independent

variable. Volume loss determined from the wear test against 1/(HRC+226/85*Vp(Gr)) was fitted into a linear equation, with a coefficient of determination very close to one, as shown in Figure 9(b). This implies that introducing graphite flakes into white irons does reduce the adhesive wear rate. Specifically, graphitic white irons have a better adhesive wear resistance compared with the non-graphite-containing irons of equivalent hardness. Quantitatively, 1 vol.% addition of graphite has the same effect as a 2.66 HRC increase in hardness with respect to the adhesive wear resistance. Eq. 2 can be used to quantitatively study the BOR adhesive wear resistance of similar alloys with any given hardness and graphite volume percent.

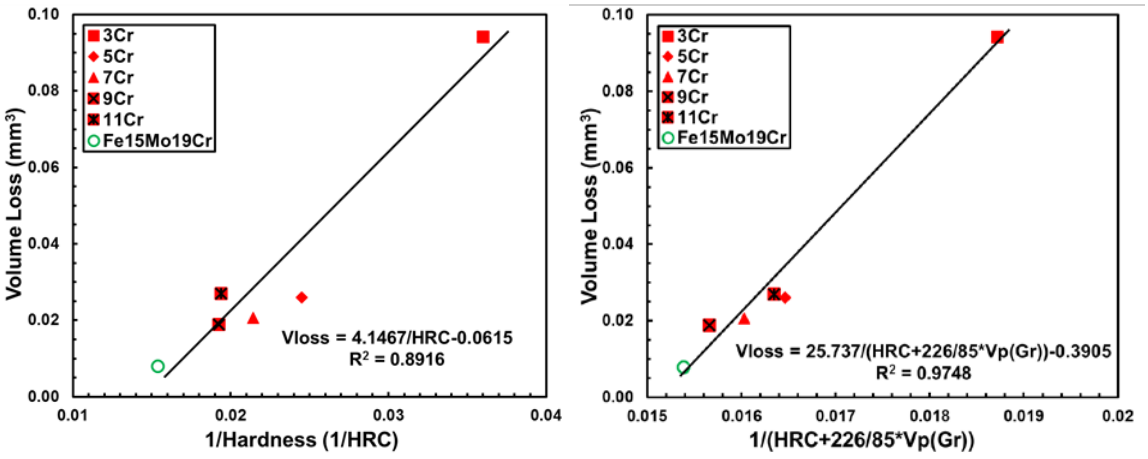

(a) (b)

Figure 9. Plots showing: (a) volume loss versus hardness of alloys studied; (b) volume loss as a function of alloy hardness and graphite volume percent.

$$Vloss = 25.737/\left(HRC + \frac{226}{85}Vp(Gr)\right) - 0.3905 \quad (2)$$

where, Vloss is the adhesive wear volume loss, HRC is the material's hardness, and Vp(Gr) is the graphite volume percent.

4.3. ADHESIVE WEAR VS. ABRASIVE WEAR

Figure 10 compared the abrasive wear test results with the adhesive wear test results. Similar to dry sand/rubber wheel (DSRW) abrasive wear, both hardness and graphite volume percent played positive roles in the wear resistance of graphitic white irons. Within the five graphitic white irons developed, alloy 9Cr showed the best wear resistance for both abrasive wear and adhesive wear. Moreover, the graphite contribution factor in the independent variable is 2.66 in adhesive wear model (Figure 9(b)) and 2.33 in abrasive wear model (Figure 1), which means that graphite addition has a stronger effect in terms of reducing the adhesive wear rate than abrasive wear rate. This is consistent with the expectation and thermal diffusivity plays a more important role in adhesive wear resistance.

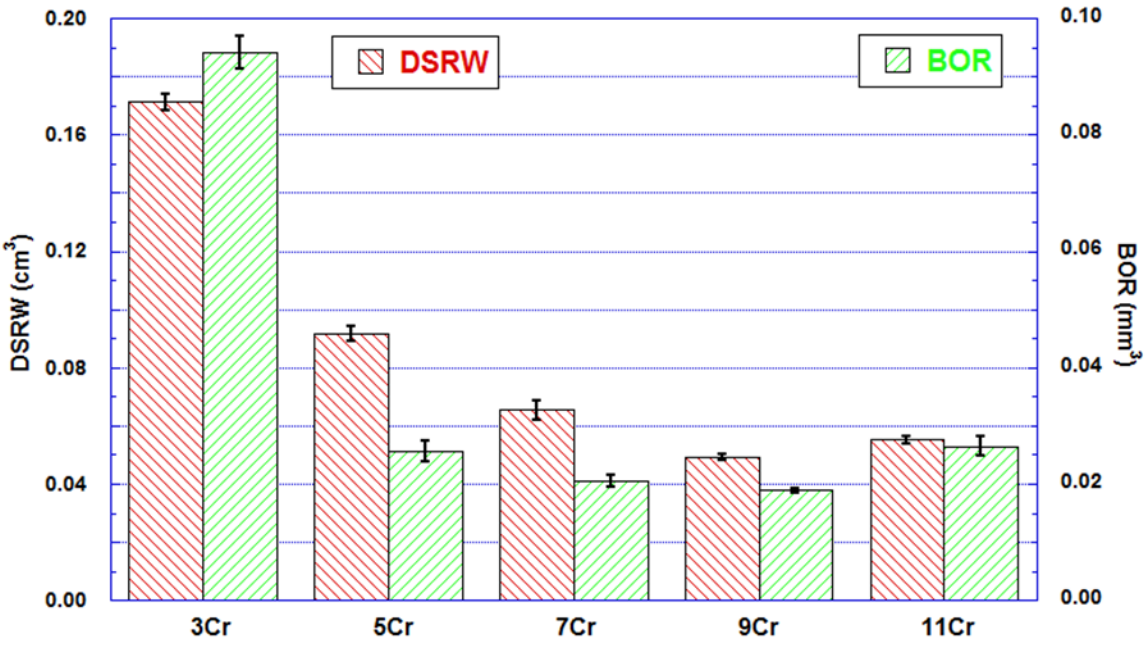

Figure 10. Wear resistance comparison between abrasive wear test (DSRW) and adhesive wear test (BOR) for five graphitic white irons developed. Error bars represent a 95% CL.

4.4. RATIONAL FOR GRAPHITE CONTRIBUTION

Authors propose two mechanisms by which the addition of graphite to chromium white iron increases the wear resistance. First, graphite addition increases the thermal diffusivity of the alloy, as shown in Figure 1, which in turn mitigates the frictional heating during the wear test and reduces the wearing surface temperature of the test specimen. Close proximity of graphite flakes to asperity contact is expected to lower the flash temperature and reduce the probability of asperity fusion, fracture of the fused asperity and material transfer. Therefore, a reduced hardness loss can be expected from the elevated thermal diffusivity, which can enhance the wear resistance and lower the wear rate during the test [40]. Graphite may also be abraded into small particles and dispersed across the whole wearing surface. Similar to the concept used for graphite impregnated metal composites [41], [42], [43], [44], the abraded and distributed graphite particles on the wear scars work as a lubricant, which further slows down the wear rate. This latter mechanism is very much similar to the self-lubricating theory adopted for bearings, gears, etc. [45], [46], [47].

5. CONCLUSION

The adhesive wear property for the first generation of graphitic white iron has been investigated. Results showed that graphite addition has a positive contribution to the adhesive wear resistance, which was benefited from the enhanced thermal diffusivity from graphite addition. The empirical model suggested that, quantitatively, 1 vol.% graphite addition has the same effect with a 2.66 HRC increase in hardness with respect

to the adhesive wear resistance. A comparison between adhesive wear model and previously developed abrasive wear model implied that graphite addition has a stronger effect in terms of reducing the adhesive wear rate than abrasive wear rate.

ACKNOWLEDGEMENTS

This work was financially supported by Caterpillar Inc. The authors would like to thank Thomas J. Yaniak for his technical discussion, and Hyung K. Yoon and Isaiah Strong for their guidance on the block on ring wear test. Perrin W. Habecker is acknowledged for his assistance with the experiments and sample preparations. The FEI Helios NanoLab SEM was obtained with a Major Research Instrumentation grant from the National Science Foundation under contract DMR-0723128.

REFERENCES

[1] X. Ai, and C. A. Moyer, "Rolling Element Bearings," in *Modern Tribology Handbook*, CRC, 2001, pp. 1041-1093.

[2] H. S. Cheng, "Gears," in *Modern Tribology Handbook*, CRC, 2001, pp. 1095-1129.

[3] R. F. Salant, "Rotary Dynamic Seals," in *Modern Tribology Handbook*, CRC, 2001, pp. 1131-1157.

[4] J. A. Hawk, R. D. Wilson, J. H. Tylczak and O. N. Dogan, "Laboratory Abrasive Wear Tests: Investigation of Test Methods and Alloy Correlation," *Wear*, vol. 225, pp. 1031-1042, 1999.

[5] M. Riddihough, "Stellite as a wear-resistant material," *Tribology*, vol. 3, no. 4, pp. 211-215, 1970.

[6] K. C. Antony, "Wear-Resistant Cobalt-Based Alloys," *Journal of Metals,* vol. 35, no. 2, pp. 52-60, 1983.

[7] J. Shin, J. Doh, J. Yoon, D. Lee, and J. Kim, "Effect of molybdenum on the microstructure and wear resistance of cobalt-base Stellite hardfacing alloys," *Surface and Coatings Technology,* vol. 166, no. 2-3, pp. 117-126, 2003.

[8] J. Wan, J. Qing, and M. Xu, "Designing a Graphitic White Iron: Microstructures and Properties," in *Association for Iron & Steel Technology 2019*, Pittsburgh, PA, 2019.

[9] J. Wan, D. C. Van Aken, J. Qing, and M. Xu, "Microstructural Characterization and Failure Analysis of a New Novel Wear-Resistant Material: Fe15Mo18Cr," 2019.

[10] K. Sipos, M. Lopez, and M. Trucco, "Surface Martensite White Layer Produced by Adhesive Sliding Wear-Friction in AISI 1065 Steel," *Revista Latinoamericana de Metalurgia Materiales,* vol. 28, no. 1, pp. 46-50, 2008.

[11] F. Klocke, E. Brinksmeier, and K. Weinert, "Capability profile of hard cutting and grinding processes," *Annals of CIRP,* vol. 54, no. 2, pp. 22-45, 2005.

[12] S. Smith, S.N. Melkote, L. Curzio, E.T. Watkins, R. Allard, and L. Riester, "Effect of surface integrity of hard turned AISI 52100 steel on fatigue performance," *Materials Science & Engineering A,* vol. 459, pp. 337-346, 2007.

[13] Y.B. Guo, and G.M. Janowski, "Microstructural characterization of white layers by hard turning and grinding," *Transactions of NAMRI/SME,* vol. 32, pp. 367-374, 2004.

[14] J. Wan, J. Qing and M. Xu, "Designing a Novel Graphitic White Iron for Metal-to-metal Wear Systems," *Metallurgical and Materials Transactions A,* vol. 50, no. 3, pp. 1162-1174, 2019.

[15] H. Berns and W. Theisen, "Tribological Properties," in *Ferrous Materials*, Bochum, Springer, 2008, p. 103.

[16] A. Kagawa, T. Okamoto, K. Saito, and M. Ohta, "Hot hardness of (Fe,Cr)3C and (Fe,Cr)7C3 carbides," *JOURNAL OF MATERIALS SCIENCE,* vol. 19, pp. 2546-2554, 1984.

[17] J. Wang, W. Guo, H. Sun, H. Li, H. Gou, and J. Zhang, "Plastic deformation behaviors and hardening mechanism of M7C3 carbide," *Materials Science and Engineering: A*, vol. 662, pp. 88-94, 2016.

[18] J. Wan, J. Qing and M. Xu, "Developing a Graphitic White Cast Iron," in *Materials Science and Technology 2018*, Columbus, 2018.

[19] J. Wan, P. W. Habecker, J. Qing and M. Xu, "Evolution of Phases in a Graphitic White Iron," in *AFS*, Atlanta, 2019.

[20] J. Wan, J. Qing, and M. Xu, "Investigation of Wear Performance for The First Generation Graphitic White Iron," in *Materials Science & Technology 2019*, Portland, OR, 2019.

[21] J. Wan, J. Qing, and M. Xu, "Investigation of Thermal Diffusivity for The First Generation Graphitic White Iron," in *Materials Science & Technology 2019*, Portland, OR, 2019.

[22] J. Wan, D. C. Van Aken, J. Qing, T. J. Yaniak, T. C. Clements, and M. Xu, "Developing a graphitic white iron for abrasive wear application: Thermal and wear properties," *Wear*, Vols. 436-437, 2019.

[23] Annual Book of ASTM Standards, "ASTM Designation E1461-13," *ASTM*, 2013.

[24] Annual Book of ASTM Standards, "ASTM Designation G65-16," *ASTM*, 2016.

[25] G. Sutter, and N. Ranc, "Flash temperature measurement during dry friction process at high sliding speed," *Wear*, vol. 268, no. 11-12, pp. 1237-1242, 2010.

[26] Annual Book of ASTM Standards, "ASTM Designation G77-17," *ASTM*, 2017.

[27] D. C. Van Aken and W. F. Hosford, "Reporting Results: A Practical Guide for Engineers and Scientists," Cambridge University, 2008, pp. 87-91.

[28] G. P. Alejandro, A. A. Florentino, and A. L. Juan, "Improvement of Adhesive Wear Behavior by Variable Heat Treatment of a Tool Steel for Sheet Metal Forming," *Materials*, vol. 12, pp. 1-10, 2019.

[29] M. S. Narassima, S. Hangovan, S. P. Anbuudayasankar, and P. Pavithran, "Effect of reinforcement and aging time on wear behavior and mechanical properties of Aluminium LM4," *International Journal of Engineering and Advanced Technology,* vol. 8, no. 5, pp. 2426-2433, 2019.

[30] M. F. Buchely, J. C. Gutierrez, L. M. Leon and A. Toro, "The Effect of Microstructure on Abrasive Wear of Hardfacing Alloys," *Wear,* vol. 259, pp. 52-61, 2005.

[31] S. B. Hosseini, U. Klement, Y. Yao, and K. Ryttberg, "Formation mechanisms of white layers induced by hard turning of AISI 52100 steel," *Acta Materialia,* vol. 89, pp. 258-267, 2015.

[32] S.Goto, C.Liu, S.Aso, and Y.Komatsu, "Proceedings of the 9th International Conference on Creep and Fracture of Engineering Materials and Structures," in *The Institute of Materials*, London, 2001.

[33] S.Goto, S.Aso, and Y.Komatsu, "Proceedings of abrasion wear resistant alloyed white cast iron for rolling and pulverizing mills," in *Japan Foundry Eng. Soc.*, Fukuoka, 2002 .

[34] L. Xu, S. Wei, J. XIng, *Chinese Journal of Mechanical Engineering,* vol. 44, pp. 50-55, 2008.

[35] K. Kato, and K. Adachi, "Wear Mechanisms," in *Modern Tribology Handbook,* CRC Press, 2010, pp. 273-300.

[36] E. Rabinowicz, "AN ADHESIVE WEAR MODEL BASED ON VARIATIONS IN STRENGTH VALUES," *Wear,* vol. 63, pp. 175-181, 1980.

[37] S. Wu, and H. S. Cheng, "A Sliding Wear Model for Partial-EHL Contacts," *Transactions of the ASME,* vol. 113, pp. 134-141, 1991.

[38] H. Wang, C. Zhou, Y. Lei, and Z. Liu, "An adhesive wear model for helical gears in line-contact mixed elastohydrodynamic lubrication," *Wear,* Vols. 426-427, pp. 896-909, 2019.

[39] J. F. Archard, "Contact and rubbing on flat surfaces," *J. appl. Phys,* vol. 24, pp. 981-988, 1953.

[40] H. Torres, M. Varga, M. R. Ripoll, "High temperature hardness of steels and iron-based alloys," *Materials Science and Engineering: A*, vol. 671, pp. 170-181, 2016.

[41] R. Kumar and T. S. Sudarshan, "Self-Lubricating Composites: Graphite-Copper," *Materials Technology*, vol. 11, no. 5, pp. 191-194, 1996.

[42] H. Goto and K. Uchijo, "Wear Mechanism of Al-Si Alloy Impregnated Graphite Composite under Dry Sliding," *Wear*, vol. 259, no. 1-6, pp. 613-619, 2005.

[43] H. Goto and S. Omori, "Friction and Wear Characterisitics of Aluminum Alloy Impregnated Carbon Composite," *Journal of Tribology*, vol. 121, no. 2, pp. 294-300, 1999.

[44] H. Goto, S. Omori and K. Uchijo , "Wear Behaviro of Al-Si Alloy Impregnated Graphite Composite," *Tribology Transactions*, vol. 44, no. 4, p. 551, 2001.

[45] D. J. Boes, and P. H. Bowen, "Friction-wear characteristics of self-lubricating composites developed for vacuum service," *ASLE Transactions*, vol. 6, pp. 192-200, 1963.

[46] S. Boubendir, S. Larbi, M. Malki, and R. Bennacer, "Hydrodynamic self-lubricating journal bearings analysis using Rabinowitsch fluid lubricant," *Tribology International*, vol. 140, 2019.

[47] J. D. Mello, C. Binder, G. Hammes, R. Binder, and A. N. Klein, "Tribological behaviour of sintered iron based self-lubricating composites," *Friction*, vol. 5, no. 3, pp. 285-307, 2017.

SECTION

3. CONCLUSIONS AND RECOMMENDATIONS

3.1. CONCLUSIONS

3.1.1. Alloy Fe15Mo18Cr. A comprehensive microstructural characterization was conducted for alloy Fe15Mo18Cr, by means of SEM and TKD techniques. Results showed that this new wear-resistant material has a complex phase constituent of ferrite, retained austenite, M_7C_3 carbide, and M_2C carbide. The utilization of thermodynamic software to predict the solidification sequence was successful and matched the size of the phase constituents very well.

Material flow, white layer, and micro-galling defects were analyzed on the contact interface of a field return wear component, which indicates that excessive frictional heat was associated with this wear component. It is believed that frictional heating is detrimental to the service life of wear components [112], [113], [114]. It was concluded that the mechanical load and frictional heating were responsible for the material flow and formation of the white layer. It was reported that white layer is an extremely brittle structure [38], [39]. Therefore, it can be fractured off during the service and leads to micro-galling defects, which were the potential root cause for failure.

An in-depth microstructural investigation on the white layer was performed using TEM and the white layer has the same phase constituents as the cast material, but appears as a mixture of randomly oriented nanocrystalline grains. TEM-BF images shows that its grain size is in the order of approximately 15 nm.

3.1.2. Graphitic White Iron. To mitigate the frictional heating effect and extend the service life of the wear component, graphite flakes were introduced into the white cast iron and these new alloy systems were designated as graphitic white irons. With the assistance of a thermodynamic software, five iron based alloys have been designed, cast, and investigated as the first generation of graphitic white iron for metal-to-metal wear systems. Graphite addition increased the thermal diffusivity and enhanced the wear performance of metal-to-metal wear systems as measured by block on ring wear test. The following conclusions can be drawn for the different aspects of the alloys studied.

3.1.2.1. Metallographic analyses of microstructures. Solidification sequences have been determined by correlating the microstructures with the FactSage equilibrium step diagrams. As chromium content in the five cast alloys increases, the chromium content in plate cementite and primary M_7C_3 carbide increases. The increased chromium content of each carbide increased their micro-hardness. Meanwhile, primary M_7C_3 carbide was measured to be much harder than plate cementite, and the cross face ((0001) plane) of M_7C_3 carbide is harder than its side face ((1010) plane). In addition, the primary M_7C_3 carbides become more regular and appears as hexagonal prisms in shape with increasing Cr content in the bulk materials. It was also observed that the primary M_7C_3 carbide has a transformed austenite core structure along its [0001] direction.

It was found, for the first time, M_7C_3 carbides formed together with austenite into a lamellar structure (similar to ledeburite) during the metastable eutectic reaction in alloy 11Cr. At lower temperature M_7C_3 in the lamellar-shaped structure was transformed into cementite. The presence of M_7C_3 in lamellar-shaped structure at high temperatures

during the early-stage metastable eutectic reaction was verified by EBSD analysis on a heat-treated specimen.

ImageJ measurements of phase fractions were consistent with the thermodynamic equilibrium calculations results for both graphite and non-eutectoid carbides. A new carbon equivalent was established for graphitic white iron using the separate multiplying factors reported in published articles, and this carbon equivalent equation was utilized to develop an empirical model to predict the graphite volume percent in this new alloy system.

3.1.2.2. Thermal diffusivity. A laser flash method to measure the thermal diffusivity of graphitic white irons was used to study heat conduction in the graphitic white irons. Results show that the thermal diffusivity increased with increasing graphite volume percent. The rate of increase of the thermal diffusivity with increasing graphite also increased with increasing graphite volume percent. However, the macroscopic hardness decreased as the volume of graphite increased. Thus, the optimal graphite volume percent still needs to be determined and should be investigated in the future.

The utilization of the lower bound of Hashin-Shtrikman model for thermal diffusivity [115] was successful in treating the graphitic white iron as a multiphase composite material. The graphite was treated as the second phase, and the alloy excluding graphite was treated as the matrix. A comprehensive numerical model was developed to predict the thermal diffusivity for any given chemical composition and temperature, which can be potentially used to predict the thermal diffusivity for other similar alloyed cast iron systems.

3.1.2.3. Wear performance. Abrasive wear and adhesive wear testing were conducted via DSRW apparatus and BOR apparatus, respectively. Results proved that graphite addition increased both abrasive wear resistance and adhesive wear resistance. Two tribological mechanisms were proposed to explain the improvement in wear resistance measured for the graphitic white irons. First, graphite addition increased the thermal diffusivity of the alloy, which in turn mitigates the frictional heating during the test and reduces the temperature of the contact interface. Graphite may also be abraded into small particles and dispersed across the whole wearing surface. Similar to the concept used for graphite impregnated metal composites, the abraded and distributed graphite particles on the wear scars work as a lubricant, which further slows down the wear rate [116], [117], [118], [119].

As for the abrasive wear performance, the hardest phase (M_7C_3) worked as "stopper" and decreased the wear rate. Meanwhile, the second hard phase (M_3C) was found effective in further increasing the wear resistance via a "buffer" effect. An empirical model was developed to predict the volume loss during the wear test based upon graphite volume percent and macro-hardness. Quantitatively, with regards to abrasive wear resistance, 1 vol.% graphite was equivalent to an increased hardness increment of 2.33 HRC.

With respect to adhesive wear testing, the volume loss for adhesive wear test decreased with increasing hardness. Evidence of metal pulled out, attachment, and plastic deformation were observed on the block specimen wear scar for each alloy, which are the characteristics of adhesive wear. An empirical model was also developed to predict the volume loss during the wear test based upon graphite volume percent and

macro-hardness. Quantitatively, with regards to abrasive wear resistance, 1 vol.% graphite was equivalent to an increased hardness increment of 2.66 HRC.

By comparing the graphite contribution factor in adhesive wear model (2.66) and abrasive wear model (2.33), one can conclude that graphite addition has a bigger effect in terms of reducing the adhesive wear rate than abrasive wear rate. This is consistent with the expectation and thermal diffusivity played a more important role in adhesive wear resistance, as the local heating or flash temperatures can be as high as 1000 °C. Both hardness and graphite volume percent played important roles in wear resistance. Within the five graphitic white irons studied, alloy 9Cr showed the best wear performance for both abrasive wear and adhesive wear. The optimal combination of hardness, and graphite volume percent need to be further studied.

3.2. RECOMMENDATIONS

Among the five graphitic white irons studied in this dissertation, alloy 9Cr had the best wear performance for both abrasive wear and adhesive wear. Upon the abrasive wear performance study, a second hard phase, usually carbide, was found effective in increasing the wear resistance via a “buffer” effect. It was found that the premium white iron Fe15Mo19Cr had a better wear performance than alloy 9Cr. The premium white iron benefited from a molybdenum containing M_6C carbide that formed in a fishbone morphology. Therefore, introducing M_6C fishbone carbide into alloy 9Cr may offer a way to formulate the next generation of graphitic white iron, which can potentially advance the wear performance of this new alloy system.

According to the stoichiometric calculation for Mo_6C, approximately 0.02 wt.% carbon addition needs to be added for every weight percent of molybdenum addition to form M_6C carbide. Thereafter, four chemical compositions have been proposed for future graphitic white iron alloy design, as shown in Table 3.1. Each of the alloy was named according to their individual molybdenum content.

Table 3.1. Chemical compositions proposed for future graphitic white iron alloy design.

Alloys	Chemical composition (wt.%)				
	C	Mo	Si	Mn	Cr
3Mo	4.99	3	2.05	0.50	9.08
4Mo	5.01	4	2.05	0.50	9.08
5Mo	5.03	5	2.05	0.50	9.08
6Mo	5.05	6	2.05	0.50	9.08

The equilibrium step diagrams for each of the alloy proposed was thermodynamically calculated using JMatPro software, as shown in Figure 3.1. It should be noted that with increasing molybdenum content in the material, the amount of M_6C carbide formed increases. However, the amount of graphite formed does not change with the molybdenum addition, and approximately 3.1 wt.% of graphite is predicted for each alloy proposed. These calculations are consistent with the equilibrium calculations for alloy 9Cr [20]. Therefore, the four alloys proposed can potentially exhibit similar thermal diffusivity with alloy 9Cr, but at a higher overall hardness. An exceptional wear performance for metal-to-metal wear systems can be expected for these proposed new alloys.

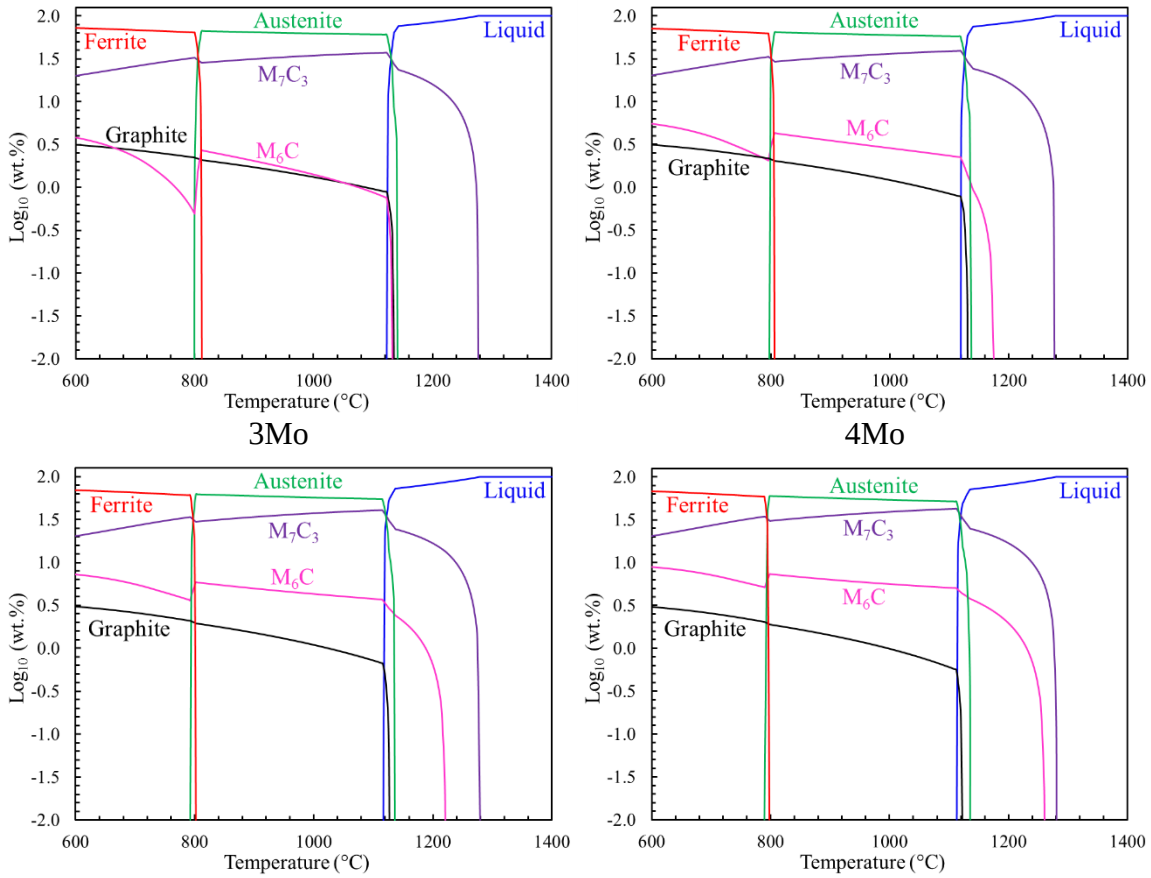

Figure 3.1. Schematics of equilibrium step diagram calculated using JMatPro for future graphitic white iron alloy design.

BIBLIOGRAPHY

[1] X. Ai, and C. A. Moyer, "Rolling Element Bearings," in *Modern Tribology Handbook*, CRC, 2001, pp. 1041-1093.

[2] H. S. Cheng, "Gears," in *Modern Tribology Handbook*, CRC, 2001, pp. 1095-1129.

[3] R. F. Salant, "Rotary Dynamic Seals," in *Modern Tribology Handbook*, CRC, 2001, pp. 1131-1157.

[4] T. A. Harris, "Friction and Wear of Rolling-Element Bearings," in *ASM Handbook Volume 18: Friction, Lubrication, and Wear Technology*, Ohio, ASM International, 2002, pp. 499-514.

[5] R. Pike, and J. M. Conway-Jones, "Friction and Wear of Sliding Bearings," in *ASM Handbook Volume 18: Friction, Lubrication, and Wear Technology*, Ohio, ASM International, 2002, pp. 515-521.

[6] D. D. Fuller, "Friction and Wear of Gas-Lubricated Bearings," in *ASM Handbook Volume 18: Friction, Lubrication, and Wear Technology*, Ohio, ASM INternational, 2002, pp. 522-534.

[7] R. Errichello, "Friction, Lubrication, and Wear of Gears," in *ASM Handbook Volume 18: Friction, Lubrication, and Wear Technology*, Ohio, ASM INternational, 2002, pp. 535-545.

[8] J. F. Dray, "Friction and Wear of Seals," in *ASM Handbook Volume 18: Friction, Lubrication, and Wear Technology*, Ohio, ASM International, 2002, pp. 546-552.

[9] J. A. Hawk, R. D. Wilson, J. H. Tylczak and O. N. Dogan, "Laboratory Abrasive Wear Tests: Investigation of Test Methods and Alloy Correlation," *Wear*, vol. 225, pp. 1031-1042, 1999.

[10] J. H. Tylczak, "Abrasive Wear," in *ASM Handbook, Volume 18: Friction, Lubrication, and Wear Technology*, Ohio, ASM International, 2002, pp. 184-190.

[11] M. Riddihough, "Stellite as a wear-resistant material," *Tribology*, vol. 3, no. 4, pp. 211-215, 1970.

[12] K. C. Antony, "Wear-Resistant Cobalt-Based Alloys," *Journal of Metals,* vol. 35, no. 2, pp. 52-60, 1983.

[13] J. Shin, J. Doh, J. Yoon, D. Lee, and J. Kim, "Effect of molybdenum on the microstructure and wear resistance of cobalt-base Stellite hardfacing alloys," *Surface and Coatings Technology,* vol. 166, no. 2-3, pp. 117-126, 2003.

[14] J. Wan, J. Qing, and M. Xu, "Designing a Graphitic White Iron: Microstructures and Properties," in *AISTech*, Pittsburgh, Pa., USA, 2019.

[15] J. O. Barlow, *Personal communication,* Peoria, 2018.

[16] H. S. Cheng, "Introduction to Lubrication," in *ASM Handbook Volume 18: Friction, Lubrication, and Wear Technology*, Ohio, ASM International, 2002, pp. 79-80.

[17] Z. Tang, "A review of corrosion inhibitors for rust preventative fluids," *Current Opinion in Solid State and Materials Science,* 2019.

[18] a. S. C. J. Mezger, "Corrosion inhibitors for fuels and lubricants". United States Patent US 20190218471A1, 18 July 2019.

[19] K. Kato, "Classification of Wear Mechanisms/Models," *Journal of Engineering Tribology,* vol. 216, no. J6, pp. 349-355, 2002.

[20] J. Wan, J. Qing and M. Xu, "Designing a Novel Graphitic White Iron for Metal-to-metal Wear Systems," *Metallurgical and Materials Transactions A,* vol. 50, no. 3, pp. 1162-1174, 2019.

[21] J. Wan, J. Qing and M. Xu, "Developing a Graphitic White Cast Iron," in *Materials Science and Technology 2018*, Columbus, 2018.

[22] J. Wan, P. W. Habecker, J. Qing and M. Xu, "Evolution of Phases in a Graphitic White Iron," in *AFS*, Atlanta, 2019.

[23] J. Wan, J. Qing, J. O. Barlow, and M. Xu, "Microstructural Characterization and Failure Analysis of a New Type of Wear-Resistant Material: Fe15Mo18Cr," 2019.

[24] J. Wan, D. C. Van Aken, J. Qing, T. J. Yaniak, T. C. Clements, and M. Xu, "Developing a graphitic white iron for abrasive wear application: Thermal and wear properties," *Wear,* Vols. 436-437, p. 202967, 2019.

[25] J. Wan, J. Qing, T. J. Yaniak, H. K. Yoon, and M. Xu, "Abrasive and Adhesive Wear of a Graphitic White Iron Designed for Metal-to-Metal Wear Systems," 2019.

[26] A. Gaard, N. Hallback, P. Krakhmalev and J. Bergstrom, "Temperature Effects on Adhesive Wear in Dry Sliding Contacts," *Wear,* vol. 268, no. 7, pp. 968-975, 2010.

[27] P. C. Okonkwo, G. Kelly, B. F. Rolfe and M. P. Pereira, "The Effect of Temperature on Sliding Wear of Steel-tool Steel Paris," *Wear,* vol. 282, no. 5, pp. 22-30, 2012.

[28] W. Molnar, A. Nevosad, H. Rojacz, K. Adam, H. J. Henze, M. R. Ripoll, and E. Badisch, "Two and three-body abrasion resistance of rubbers at elevated temperatures," *Wear,* Vols. 414-415, pp. 174-181, 2018.

[29] H. Rojacz, H. Pahr, S. Baumgartner, and M. Varga, "High temperature abrasion resistance of differently welded structural steels," *Tribology International,* vol. 113, pp. 487-499, 2017.

[30] F. E. Kennedy, "Frictional Heating and Contact Temperatures," in *Modern Tribology Book*, CRC, 2001, pp. 235-272.

[31] L. J. Gschwender, D. C. Kramer, B. K. Lok, S. K. Sharma, C. E. Snyder, and M. L. Sztenderowicz, "Liquid Lubricants and Lubrication," in *Modern Tribology handbook*, CRC, 2001, pp. 361-373.

[32] C. Barnes, *Failure Analysis*, Peoria, IL, 2015.

[33] G. Guerrini, F. Lerra, and A. Fortunato, "The effect of radial infeed on surface integrity in dry generating gear grinding for industrial production of automotive transmission gears," *Journal of Manufacturing Processes,* vol. 45, pp. 234-241, 2019.

[34] A. Alok, and M. Das, "White layer analysis of hard turned AISI 52100 steel with the fresh tip of newly developed HSN2 coated insert," *Journal of Manufacturing Processes,* vol. 46, pp. 16-25, 2019.

[35] R. D. Gruiter, "WHITE LAYER IN HARD TURNING," 2015.

[36] S. S. Bosheh, and P. T. Mativenga, "White layer formation in hard turning of H13 tool steel at high cutting speeds using CBN tooling," *International Journal of Machine Tools & Manufacture*, vol. 46, pp. 225-233, 2006.

[37] F. Klocke, E. Brinksmeier, and K. Weinert, "Capability profile of hard cutting and grinding processes," *Annals of CIRP*, vol. 54, no. 2, pp. 22-45, 2005.

[38] S. Smith, S.N. Melkote, L. Curzio, E.T. Watkins, R. Allard, and L. Riester, "Effect of surface integrity of hard turned AISI 52100 steel on fatigue performance," *Materials Science & Engineering A*, vol. 459, pp. 337-346, 2007.

[39] Y.B. Guo, and G.M. Janowski, "Microstructural characterization of white layers by hard turning and grinding," *Transactions of NAMRI/SME*, vol. 32, pp. 367-374, 2004.

[40] S. Natarajan, E. Anand, K. S. Akhilesh, A. Rajagopal, and P. P. Nambiar, "Effect of graphite addition on the microstructure, hardness and abrasive wear behavior of plasma sprayed NiCrBSi coatings," *Materials Chemistry and Physics*, vol. 175, pp. 100-106, 2016.

[41] J. Krawczyk and J. Pacyna, "Effect of the Cooling Rate on the Mottled Cast Iron Microstructure Designed for the Mill Rolls," *Metallurgy and Foundry Engineering*, vol. 35, no. 2, pp. 101-110, 2009.

[42] J. Krawczyk and J. Pacyna, "The Influence of Microstructure of Mottled Cast Iron for Mill Rolls on its Properties," *18th International Conference on Metallurgy and Materials*, pp. 266-272, 2009.

[43] J. Krawczyk and J. Pacyna, "Influence of a Matrix on Properties of Mottled Cast Iron Applied for Mill Rolls," *Archives of Foundry Engineering*, vol. 10, no. 3, pp. 45-50, 2010.

[44] J. J. Coronado, A. Gomez and A. Sinatora, "Tempering Temperature Effects on Abrasive Wear of Mottled Cast Iron," *Wear*, vol. 267, pp. 2070-2076, 2009.

[45] J. J. Coronado and A. Sinatora, "Particle Size Effect on Abrasion Resistance of Mottled Cast Iron with Different Retained Austenite Contents," *Wear*, vol. 267, pp. 2077-2082, 2009.

[46] J. J. Coronado, S. A. Rodriguez, C. E. K. Mady and A. Sinatora, "Mechinical Properties of Cementite in Mottled Cast Iron," in *ABRASION2008*, Trento, 2008.

[47] T. Matsushita, A. G. Saro, L. Elmquist and A. W. Jarfors, "On the Specific Heat and Thermal Diffusivity of CGI and SGI Cast Irons," *International Journal of Cast Metals Research,* vol. 30, pp. 276-282, 2017.

[48] D. M. Stefanescu, "Classification and Basic Metallurgy of Cast Iron," in *ASM Handbook Volume 1,* Ohio, ASM Internatinal, 2002, pp. 3-11.

[49] H. Berns, and W. Theisen, Ferrous Materials, Springer- Verlag Berlin Heidelberg, 2008.

[50] R. B. Gundlach, and D. V. Doane, "Alloy Cast iron," in *ASM Handbook Volume 1,* Ohio, ASM International, 2002, p. 326.

[51] R. B. Gundlach, "White Iron and High-Alloyed Iron Castings," in *ASM Handbook Volume 15,* Ohio, ASM International, 2002, pp. 896-903.

[52] "ASTM Designation A532," in *Annual Book of ASTM Standards,* ASTM International, 2014.

[53] M. Mohammadnezhad, V. Javaheri, M. Shamanian, M. Naseri and M. Bahrami, "Effects of vanadium addition on microstructure, mechanical properties and wear resistance of Ni-Hard4 white cast iron," *Materials & Design,* vol. 49, pp. 888-893, 2013.

[54] M. Filipovic, Z. Kamberovic and M. Korac, "Solidification of high chromium white cast iron alloyed with vanadium," *Materials Transactions,* vol. 52, pp. 386-390, 2011.

[55] A. Bedolla-Jacuinde, M. W. Rainforth and I. Mejia, "The role of silicon in the solidification of high-Cr cast irons," *Metall. Trans. A,* vol. 44, pp. 856-872, 2013.

[56] Z. F. Huang, J. D. Xing, X. H. Zhi and Y. M. Gao, "Effect of Ti addition on morphology and size of primary M7C3 type carbide in hypereutectic high chromium cast iron," *Materials Science and Technology,* vol. 27, pp. 426-430, 2014.

[57] W.T. Yu, J. Li, C.B. Shi, and Q.T. Zhu, "Effect of Titanium on the Microstructure and Mechanical Properties of High-Carbon Martensitic Stainless Steel 8Cr13MoV," *Metals,* vol. 6, p. 193, 2016.

[58] X. Zhi, J. Xing, H. Fu, and M. Gao, "Effect of titanium on the as-cast microstructure of hypereutectic high chromium cast iron," *Materials Characterization,* vol. 59, pp. 1221-1226, 2008.

[59] A. Bedolla-Jacuinde, R. Correa, J. G. Quezada and C. Maldonado, "Effect of titanium on the as-cast microstructure of a 16% chromium white iron," *Materials Science and Engineering A,* vol. 398, pp. 297-308, 2005.

[60] X. Wu, J. Xing, H. Fu and X. Zhi, "Effect of titanium on the morphology of primary M7C3 carbides in hypereutectic high chromium white iron," *Materials Science and Engineering A,* vol. 457, pp. 180-185, 2007.

[61] M. E. Maja, M. G. Maruma, L. A. Mampuru and S. J. Moema, "Effect of niobium on the solidification structure and properties of hypoeutectic high-chromium white cast irons," *Journal of the Southern African Institute of Mining and Metallurgy,* vol. 116, pp. 981-986, 2016.

[62] P. E. Belyakova, M. E. Garber, and E. V. Rozhkova, "Physical properties of white chromium cast irons," *Metal Science and Heat Treatment,* vol. 17, no. 12, pp. 1041-1044, 1975.

[63] M. Riddihough, "Stellite as a wear-resistant material," *Tribology,* vol. 3, no. 4, pp. 211-215, 1970.

[64] K. C. Antony, "Wear-Resistant Cobalt-based Alloys," *JOM,* vol. 35, no. 2, pp. 52-60, 1983.

[65] "Stellite," Wikipedia, 2019.

[66] "Sliding wea rcharacteristics of molybdenum containing Stellite 12 coating at elevated temperatures," *TribologyInternational,* vol. 91, pp. 40-47, 2015.

[67] L. Jiang, W. Zhang, Z. Xu, H. Huang, X. Ye, B. Leng, L. Yan, Z. Li, and X. Zhou, "M2C andM6C carbide precipitation in Ni-Mo-Cr based superalloys containing silicon," *Materials and Design,* vol. 112, pp. 300-308, 2016.

[68] "Stellite Alloy," Kennametal Inc., [Online]. Available: http://www.stellite.com/en/products/stellite-family/stellite-family-stellite.html. [Accessed 10 September 2019].

[69] Y. Birol, "High temperature sliding wear behaviour of Inconel 617 and Stellite 6 alloys," *Wear,* vol. 269, pp. 664-671, 2010.

[70] "Stellite 12 Alloy," Deloro Stellite.

[71] J. Shin, J. Doh, J. Yoon, D. Lee, and J. Kim, "Effect of molybdenum on the microstructure and wear resistance of cobalt-base Stellite hardfacing alloys," *Surface and Coatings Technology,* vol. 166, pp. 117-126, 2003.

[72] I. A. Inman, S. Datta, H. L. Du, J. S. Burnell-Gary, and Q. Luo, "Microscopy of glazed layers formed during high temperature sliding wear at 750 ◦C," *Wear,* vol. 254, pp. 461-467, 2003.

[73] S. Apay, B. Gulenc, "Wear properties of AISI 1015 steel coated with Stellite 6 by microlaser welding," *Mayterials and Design,* vol. 55, pp. 1-8, 2014.

[74] M. S. Sawant, and N. K. Jain, "Investigations on wear characteristics of Stellite coating by micro-plasma transferred arc powder deposition process," *Wear,* Vols. 378-379, pp. 155-164, 2017.

[75] S. Houdkova, Z. Pala, E. Smazalova, M. Vostrak, abd Z. Cesanek, "Microstructure and sliding wear properties of HVOF sprayed, laser remelted and laser clad Stellite 6 coatings," *Surface & Coatings Technology,* vol. 318, pp. 129-141, 2017.

[76] P. Sassatelli, G. Bolelli, M. L. Gualtieri, E. Heinonen, M. Honkanen, L. Lusvarghi, T. Manfredini, R. Rigon, and M. Vippola, "Properties of HVOF-sprayed Stellite-6 coatings," *Surface & Coatings Technology,* vol. 338, pp. 45-62, 2018.

[77] P. Crook, and H. N. Framer, "Friction and Wear of Hardfacing Alloys," in *ASM Handbook Volume 18,* Ohio, ASM International, 2002, pp. 758-767.

[78] W. L. Mankins, and S. Lamb, "Nickel and Nickel Alloys," in *ASM Handbook Volume 2,* Ohio, ASM International, 2002, pp. 428-445.

[79] M. Vasilescu, and M. Dobrescu, "Hardfacing Corrosion and Wear Resistant Alloys," *Advanced Materials Research,* vol. 1114, pp. 196-205, 2015.

[80] Annual Book of ASTM Standards, "ASTM Designation G65-16," *ASTM,* 2016.

[81] Q. Ming, L. C. Lim, and Z. D. Chen, "Laser cladding of nickel-based hardfacing alloys," *Surface and Coatings Technology*, vol. 106, pp. 174-182, 1998.

[82] Q. Ming, L. C. Lim, and Z. D. Chen, "Laser cladding of nickel-based hardfacing alloys," *Surface and Coatings Technology*, vol. 106, no. 2-3, pp. 174-182, 1998.

[83] G. Chakraborty, N. Kumar, C.R. Das, S. K. Alber, A. K. Bhaduri, S. Dash, and A. K. Tyagi, "Study on microstructure and wear properties of different nickel base hardfacing alloys deposited on austenitic stainless steel," *Surface and Coatings Technology*, vol. 288, pp. 180-188, 2014.

[84] Annual Book of ASTM Standards, "ASTM Designation G40-17," *ASTM*, 2017.

[85] R. G. Bayer, Mechanical Wear Prediction and Prevention, New York: Marcel Dekker, 1994.

[86] J. T. Burwell, "Survey of possible wear mechanisms," *Wear*, vol. 1, pp. 119-141, 1957.

[87] K. Kato, and K. Adachi, "Wear Mechanisms," in *Modern Tribology Handbook*, CRC, 2001, pp. 273-300.

[88] E. Rabinowicz, Friction and Wear of Materials, New York: Wiley, 1995.

[89] J. D. majumdar, and I. Manna, "Laser surface engineering of titanium and its alloys for improved wear, corrosion and high-temperature oxidation resistance," in *Laser Surface Engineering*, Woodhead, 2015, pp. 483-521.

[90] I. D. marinescu, W. B. Rowe, B. Dimitrov, and I. Inasaki, "Forces, Friction, and Energy," in *Tribology of Abrasive Machining Processes*, Noyes, 2004, pp. 121-176.

[91] J. A. Schey, Tribology in Metalworking, Ohio: American Society for Metals, 1983.

[92] K. Hokkirigawa, K. Kato and Z. Z. Li, "The Effect of Hardness on the Transition of the Abrasive Wear Mechanism of Steels," *Wear*, vol. 123, pp. 241-251, 1988.

[93] J. H. Tylczak, J. A. Hawk and R. D. Wilson, "A Comparison of Laboratory Abrasion and Field Wear Results," *Wear*, vol. 225, pp. 1029-1069, 1999.

[94] D. Tolfree, "Investigation of the Gouging Abrasion Resistance of Materials in the Mining Industry," McGill University, 2000.

[95] K. Hokkirigawa, and K. kato, "An experimental and theoretical investigation of ploughing, cutting and wedge formation during abrasive wear," *Tribology International,* vol. 21, no. 1, pp. 51-57, 1988.

[96] J. M. Challen, P. L. B. Oxley, and B. S. Hockenhull, "Prediction of Archard's wear coefficient for metallic sliding friction assuming a low cycle fatigue wear mechanism," *Wear,* vol. 111, no. 3, pp. 275-288, 1986.

[97] R. H. Dauskardt, "A FRICTIONAL-WEAR MECHANISM FOR FATIGUE-CRACK GROWTH IN GRAIN BRIDGING CERAMICS," *Acta metall, mater.,* vol. 41, no. 9, pp. 2765-2781, 1993.

[98] J. T. Burwell, "SURVEY OF POSSIBLE WEAR MECHANISMS," *Wear,* vol. 1, pp. 119-141, 1957.

[99] A. W. Lui, and G. R. Hoey, "Corrosive and erosive wear of metals in mineral slurries," *The Canadian Journal of Metallurgy and Materials Science,* vol. 12, pp. 185-190, 2013.

[100] H. Abd-Ei-kader, and S. M. Ei-Raghy, "Wear-corrosion mechanism of stainless steel in chloride media," *Corrosion Science,* vol. 26, no. 8, pp. 647-653, 1986.

[101] V. S. Saji, "A Review on Recent Patents in Corrosion Inhibitors," *Recent Patents on Corrosion Science,* vol. 2, pp. 6-12, 2010.

[102] N. C. Welsh, "Frictional Heating and Its Influence on the Wear of Steel," *JOURNAL OF APPLIED PHYSICS,* vol. 28, pp. 960-968, 1957.

[103] J. Bos , and H. Moes, "Frictional Heating of Tribological Contacts," *Journal of Tribology,* vol. 177, no. 1, pp. 171-177, 1995.

[104] M. Amiri, and Michael M. Khonsari, "On the Thermodynamics of Friction and Wear—A Review," *entropy ,* vol. 12, pp. 1021-1049, 2010.

[105] S. R. Pearson, P. H. Shipway, J. O. Abere, and R. A. A. Hewitt, "The effect of temperature on wear and friction of a high strength steel in fretting," *Wear,* vol. 303, pp. 622-631, 2013.

[106] L. M. Du, L. W. Lan, S. Zhu, H. J. Yang, X. H. Shi, P. K. Liaw, and J. W. Qiao, "Effects of temperature on the tribological behavior of Al0.25CoCrFeNi high-entropy alloy," *Journal of Materials Science & Technology,* vol. 35, no. 5, pp. 917-925, 2019.

[107] T. S. Mahmoud, "Artificial neural network prediction of the wear rate of powder metallurgy Al/Al2O3 metal matrix composites," *Proc. IMechE Vol. 226 Part L: J. Materials: Design and Applications,* vol. 226, no. 1, pp. 3-15, 2011.

[108] B. Basu, and M. Kalin, Tribology of Ceramics and Composites: A Materials Science Perspective, John Wiley & Sons, 2011.

[109] J. F. Archard, "THE TEMPERATURE OF RUBBING SURFACES," *Wear,* vol. 2, pp. 438-455, 1958.

[110] A. H. Abdel-Aal, "Flash Temperature Theory," in *Encyclopedia of Tribology*, Boston, Springer, 2013.

[111] G. Sutter, and N. Ranc, "Flash temperature measurement during dry friction process at high sliding speed," *Wear,* vol. 268, no. 11-12, pp. 1237-1242, 2010.

[112] D. Cheng, J. Park, J. Suh, S. Kim, and C. Park, "Effect of frictional heat generation on the temperature distribution in roller linear motion rail surface," *Journal of Mechanical Science and Technology,* vol. 31, no. 3, pp. 1477-1487, 2017.

[113] J. Takabi, and M. M. Khonsari, "Experimental testing and thermal analysis of ball bearings," *Tribology International,* vol. 60, pp. 93-103, 2013.

[114] G. Fortunato, V. Ciaravola, A. Furno, B. Lorenz, and B. N. J. Persson, "General theory of frictional heating with application to rubber friction," *Journal of Physics: Condensed Matter,* vol. 27, p. 17, 2015.

[115] Z. hashin, "Analysis of composite materials- a survey," *J. Appl. Mech.,* vol. 50, no. 3, pp. 481-505, 1983.

[116] R. Kumar and T. S. Sudarshan, "Self-Lubricating Composites: Graphite-Copper," *Materials Technology,* vol. 11, no. 5, pp. 191-194, 1996.

[117] H. Goto and K. Uchijo, "Wear Mechanism of Al-Si Alloy Impregnated Graphite Composite under Dry Sliding," *Wear,* vol. 259, no. 1-6, pp. 613-619, 2005.

[118] H. Goto and S. Omori, "Friction and Wear Characterisitics of Aluminum Alloy Impregnated Carbon Composite," *Journal of Tribology*, vol. 121, no. 2, pp. 294-300, 1999.

[119] H. Goto, S. Omori and K. Uchijo , "Wear Behaviro of Al-Si Alloy Impregnated Graphite Composite," *Tribology Transactions*, vol. 44, no. 4, p. 551, 2001.

VITA

Jie Wan was born in 1992 in Shaanxi, China. He graduated from Middle School Attached to Northwestern Polytechnical University in June of 2008. Upon graduation, he entered Xi'an Jiaotong University in China, and received his bachelor of engineering degree in Material Science and Engineering and bachelor of management degree in Accounting in June of 2015. He was awarded the APEC-Caterpillar Fellowship in September of 2015 and started to pursue his Ph.D. of Materials Science and Engineering in Missouri University of Science and Technology in January of 2016.

He received his Ph.D. in Materials Science & Engineering, from Missouri University of Science and Technology in December of 2019. He earned this degree under the advising of Dr. Mingzhi Xu and Dr. David C. Van Aken.